Inflow Turbulent Effects on Tidal Turbines

experimental and numerical study

Luca Camosi

Supervisor: Dr. J.A. Teixeira

School of Water, Energy and Environment

Cranfield University

This dissertation is submitted for the degree of

Doctor of Philosophy

Power Engineering Group April 2018

Abstract

Hydrokinetic tidal turbines are devices for which the relative importance of the incoming flow on fatigue life is higher when compared to wind generators. This is due to the difference in density between the two fluids and because of the more turbulent nature of marine channel flows [50] compared to winds.

This work is part of an effort to produce a more accurate description of the impact of turbulence on open-rotor turbines in general. In order to reach the described scope the author conducted an experimental campaign and developed numerical tools within the OpenFOAM [5] CFD libraries.

The experimental campaign conducted in IFREMER (Boulogne-sur-Mer France) provides data used for the numerical model validation.

The developed models consists in two main parts:

1. an actuator line turbine model similar to that presented by Churchfield in [18] but more integrated with the OpenFOAM libraries

2. two novel generators of turbulence for Large Eddy Simulations (LES) inlet boundary conditions

    - one that combines the state of the art generator philosophy for CFD [60] with a more general statistical representation approach by Shinozuka and al. [57]. This method is designed to accurately match the first order statistics of a flow given the turbulence spectra in a position of interest.
    - a second approach has been developed in order to reproduce the typical flow structures particular of a specific site. It makes use of Proper Orthogonal Decomposition (POD) in order to describe the intrinsically non homogeneous nature of environmental turbulence. Such is the case in tidal channel flows.

The combination of the developed libraries constitutes an enabling simulation toolbox for the study of tidal turbines dynamic response to turbulence.

The author could test the qualitative behavior of the second approach compared to the current state of the art showing promising results. Results from the first approach intended for the dynamic validation of the IFREMER turbine model are not shown in this thesis report being analysis not completed yet.

The comparison of the torque and thrust signatures on the turbine from different inflow generators shows equivocally the importance of accurate modeling of turbulence when assessing the effects of dynamic load on hydrokinetic tidal turbines.

Furthermore the POD methodology is used to analyse flow data from the Ramsey Sound site where the company sponsor of this work installed a full-size device. These show the high meaningfulness of the POD methodology in the description of turbulent flows.

Table of contents

List of figures

List of tables

Nomenclature

Roman Symbols

α airfoil angle of attack

μ dynamic viscosity

$\tau_w = \mu \left(\frac{\partial u}{\partial y}\right)_{y=0}$ wall shear stress

θ pitch angle of the blade

c airfoil chord length

$C_d = \frac{D}{\frac{1}{2}\rho v^2 A}$ airfoil drag (D drag force) coefficient

$C_l = \frac{L}{\frac{1}{2}\rho v^2 A}$ airfoil lift (L lift force) coefficient

Re Reynolds Number $\frac{uL}{\nu}$ with u velocity, L length and ν kinematic viscosity

U velocity magnitude

$u_* \equiv \sqrt{\frac{\tau_w}{\rho}}$ friction velocity

$y_w^+ \equiv \frac{u_* y}{\nu}$ non-dimensional wall distance

ADCP Acoustic Doppler Current Profilers

ADV Acoustic Doppler Velocimeter

ALM Actuator Line Model

BEM Blade-Element Momentum

CFD Computational Fluid Dynamics

DNS Direct Numerical Simulation

FEA Finite Element Analysis

GDW Generalized Dynamic Wake

LES Large Eddy Simulation

N-S Navier-Stokes Equations

NREL National Renewable Energy Laboratory

ODE Ordinary Differential Equations

PCA Principal components analysis

PIV Particle Image Velocimetry

POD Proper Orthogonal Decomposition

PSD Power Spectral Density

RANS Reynolds Averaged Navier-Stokes

TSR Tip Speed Ratio

Part I

Introduction

Chapter 1

Introduction

1.1 Introduction to Tidal Energy

1.1.1 Tidal power

The use of this resource was historically applied to produce mechanical power generally applied to a grinding wheat process.
That was achieved by the transformation of the potential energy accumulated by the water due to the high tide into mechanical energy during the period of low tide when the water free-surface lowers. The flow so generated was used to power a water mill.
Nowadays direct mechanical transformation is no longer practical for the society necessities and that energy is converted in electricity via electrical generators and distributed locally to the users. New types of generation plants are also in study and constant development.
Currently two main types have successfully been employed in producing power

- tidal barrages
- tidal stream generators

The former is in a mature state consisting in a dam-like structure that separates the ocean from a bay or river. Every time a convenient static head is present between the two sides of the barrage, hydro turbines are used to extract power from the occurring potential gradient.

The latter which is topic of this work, consists in placing array-like or fence-like a number of devices whose aim is converting the dynamic energy due to the water movement caused by the tide change. These kinds of devices resemble the wind turbines in terms of operational principles and configurations.

The two techniques above represent opposite ways of extracting power from tides. The first extracting the static potential accumulated by the water during the high tide. The second converting some of the dynamic part of this movement during the change of the tide in terms of velocity of the water.

It is worth citing a third way, still unapplied, that results in a combination of the two mentioned techniques in terms of operational principle. Rather than isolating part of the shore line from the rest of the sea, a long (several tens of kilometers) dam is built along a line perpendicular to the cost whose end draws a T, when viewed from the top. This will allow, in shallow water, to exploit the dynamic motion parallel to the coast as a static head between the two sides of the dam separating two phases of the phenomenon. Reversible machines can be installed in order to use either of the directions of the water motion.

A review of the state of the art tidal hydrokinetic turbines installed and under development can be found in [10].

1.1.2 Tidal Energy Limited project

Tidal Energy Ltd is an innovative renewable energy company, which was set up in Wales by a team of marine engineering and renewable energy experts. Their concept test rig was financed by European Structural Funds, administered by the Welsh European Funding Office on behalf of the Welsh Government. Cranfield University has been involved in the design and development of DeltaStream since 2007, and were a research partner for the Ramsey Project where the first full-scale DeltaStream device was tested.
DeltaStream was deployed in December 2015 in a water depth of some 35.0m approximately 1.2km from St Justinian's, Pembrokeshire (Fig. 1.1).

Ramsey Sound was chosen because of many reasons like: sheltered wind and wave conditions, good water depths close to the mainland and a suitable grid connection. In addition no turbine conflicting costal activities are conducted in the Sound like trawling and commercial shipping. The location chosen for DeltaStream is a flat bedrock shelf in the north of Ramsey Sound. There were no problems for navigation, because there will be at least 11.9m of water above the blade tips at lowest tide level. Ramsey Sound is however quite sensitive in terms of its ecology due to the presence of a colony of grey seals nearby.

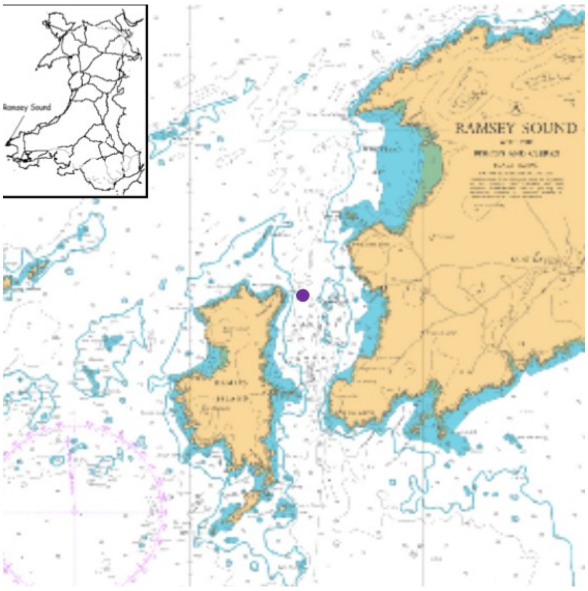

Fig. 1.1 Location of DeltaStream

1.1.3 DeltaStream design

Each complete DeltaStream device has three tidal stream turbines, made up of the nacelle, hub and rotor blades. Initially a 12m diameter rotor was installed onto DeltaStream and following successful testing of this rotor the device will be lifted from the be seabed and a 15m diameter rotor will be installed. The 15m diameter rotor will allow testing of a full scale DeltaStream device.

The rated generation capacity of the device is up to 1.2MW of electricity. Each turbine provides 400 kW power. The frame has an equilateral triangular foundation (each side 36m wide) which means that it can be securely placed on the seabed without the need for a positive anchoring system. The use of three turbines on a single triangular frame (Fig. 1.2) produces a low centre of gravity enabling the device to satisfy its structural stability requirements, including the avoidance of overturning and sliding. DeltaStream can be removed from the seabed by a carefully developed lifting procedure and taken away when the project is finished.

The blades were designed by Cranfield University, and provide a high stagger angle, that increases the Ct/Cp ratio. In this way, the drag for a given power is slightly lower but it minimises thrust loads at high tip speed ratios. The number of the blades was chosen as

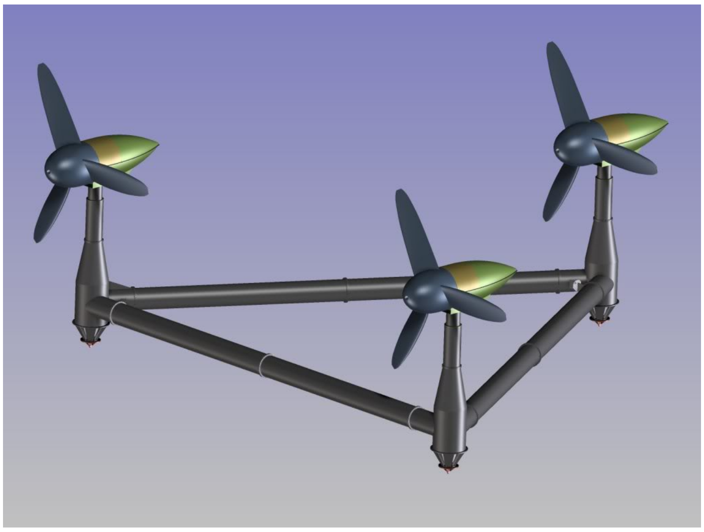

Fig. 1.2 DeltaStream

a compromise between tip loss and robust blades. Increasing the number of blades leads to a shorter rotor and to slender blades. The blade hydrodynamic design is to ensure that the thrust load decreases with the increasing of the rotational velocity of the rotor, which is facilitated through torque control of the electric generator.

Once onshore, power conversion and conditioning equipment connects the system to the National Grid.
The benefits of DeltaStream include:

1. Ease of manufacture
2. Gravity foundation
3. Fixed pitch blades dispensing pitching gear
4. Relatively slow rotational speed
5. Ease of deployment and recovery for maintenance
6. Low cost of manufacture and deployment/maintenance
7. Operates in various water depths and velocities
8. Does not require drilling or piling into the seabed
9. Low environmental impact

10. Subsurface at all tidal states

11. Avoids shipping interference

From the environmental point of view all the aspects where taken into consideration by the DeltaStream project including oceanographic environment, the presence of the mammals and diving birds and the intertidal, subtidal marine ecology assessment, fish and commercial fisheries assessment, navigation, tourism and recreation, terrestrial ecology and the cultural heritage assessment.

1.2 Unsteady loads

Much of the original information about tidal turbines loading regimes was deduced from wind turbine literature concerning the impact of turbulent fluctuations on the structure. The main difference between the two devices is the relative importance of dynamic loading: water density being three orders of magnitude larger than air, all the problems connected with inertial effects are certainly enhanced.

Thus, a close attention must be paid to all the possible sources of dynamic loading for tidal devices. According to [20] for a wind turbine the unsteady loadings due to the atmospheric turbulence can be of the same order of magnitude of those caused by the presence of an upstream turbine. The lack of a full understanding of the loading regimes, both in terms of the magnitudes and the spectral features of the hydrodynamic loads is likely to have been at the root of a number of early prototype failures.

Therefore this work will focus on the understanding of two factors:

1. the modelling of turbulence in the tidal channel and
2. the modelling of the wake generated by a turbine which is exposed to a turbulent inflow field.

This is highly dependent on the location where the device is installed.

The role played by the tidal climate in the turbine loading has been attracting the growing attention of researchers in recent years. At its root are the advances in the instrumentation that enables the obtaining of such data, Acoustic Doppler Current Profilers (ADCPs) and Acoustic Wave and Current (AWAC) profilers. These devices obtain flow data along inclined acoustic beams and are known to unreliably resolve the instantaneous three-dimensional velocity required for first-order turbulence evaluation. Therefore most of the existing turbulence data for tidal channels, obtained with this type of equipment, assumes that the second-order statistical moments of velocity are homogeneous over the beam spread [27], an assumption that is compromised by the tilting of the sensors.

Not only turbulence but also wind induced waves affect the loading of the turbines. Galloway et al. 2010 [27] investigated the effect of 0.08 m high waves with a period of 1.43s on a scaled model turbine with swept area 0.5 m2 in a towing tank. The authors found that the waves action did not impact on the average performance characteristics, thrust and power due to the reciprocating motion of the waves effectively cancelling out about the average. However large variations, of 37% of the mean for thrust, and 35% for power, due to cyclic effects were observed. These findings agree with those of Luznik [48], where average performance values were also found to be unchanged but the the power coefficient varied from the essentially average value of 0.38 to a maximum of 0.45 and a minimum of 0.25.

One of the earlier works to focus on the combined loading effects of waves and current was due to Barltrop [9], who used a combination of blade element-momentum theory and the results of wave tank tests for predicting the torque and thrust on a marine current turbine. A key finding of this work consisted in the observation that when the tip-speed ratio is maintained constant, in shorter waves a stall may take place leading to a sudden reduction in torque and increase in thrust at medium rotational speed. In longer waves, stall was not observed and hence, torque and thrust curves show more steady characteristics.

The implications for the fatigue of the turbine were studied by McCann, 2007[50], who employed Garrad Hassan's Tidal Bladed BEM code to model a generic, 22.8m diameter, 2MW turbine operating in a range of flow turbulence and sea-state environments. McCann's results showed that the fatigue stress margins for the blade root, for a combination of significant wave heights and turbulence intensity, varied from 86 to 11% as the turbulence intensity was changed from 0 to 12%. The contribution from waves was similar through the reduction in fatigue stress margin to lower than a third as the significant wave height varied from 1.5 to 6m. One of the limitations of McCann's study lay in the fact the model employed to represent the flow turbulence was the standard von Karman spectral density model used to represent atmospheric turbulence. The sea state simulations made use of a JONSWAP wave spectrum.

1.2.1 Realistic inflow conditions

The need for more realistic inflow conditions for such simulations has been raised by several authors. Adrian et al. [6] presented a review of the methods available. They mostly consist in introducing perturbations over the mean velocity profile. The consequence is that a very long computational domain is required in the direction of the flow before turbulence can develop naturally from the initial condition.

The most evident problem associated to this is that simulations become extremely computationally expensive. An interesting case could be that of a Formula 1 car following a car up-track during cornering. In order to simulate the effect on the following car, so that it can be optimised to work more efficiently in a turbulent flow, would require the simulation of both cars together. However, having the possibility of reproducing realistically the turbulent structures coming from the upstream car, one could limit the simulation to the downstream car only. The same it could be said in the case of closely spaced wind turbines in a farm.

There is a second one though which is sometimes overlooked by the community of scientists and it is mostly engineering related: most of the flows in use for practical applications cannot be reproduced at all by introducing an elongated domain. Only very simple cases such as channel, boundary layer and jet flows are of feasible application. In turbomachinery, for example, it would be impossible to reproduce via Large Eddy Simulations the flow coming from a stage and its effect on the downstream one without modelling the entire device. For an environmental flow this can be even more evident. Let's imagine that a wind turbine is positioned at some distance from a building, trees, other closely spaced turbines and some complex ground features. An accurate simulation would require the modelling of all of these features and sill it would not include the effect of others placed just some distance further away. In the case of the present work, modelling a tidal channel presents a very high level complexity to the point of being currently and for the foreseeing years to come, practically impossible.

The simulation would require capability of modelling all the complex features and shape of the seabed, the effect of wakes on the flow and the pressure gradients caused by the seasonal and semi-diurnal specific tide. An expedient and accurate method of reproducing the inflow to a particular system to be studied is then a problem that is becoming more and more important nowadays with the increase of computational power and the transition of the industry from average flow.

1.3 Aims and Objectives

The project is carried out in collaboration with the sponsor Tidal Energy Limited and concerns its three turbine Deltastream device. The final design of the first prototype has frozen at the time of the writing of this report but some aspects of its operation remain to be further resolved. This research is expected to contribute to the operating philosophy of the device as well as to the knowledge required for the development of subsequent versions of the device. Data on performance and loading were unfortunately unavailable for the validation of the models developed during the project. Tidal channel turbulence data have been acquired prior the device deployment and will also be employed to validate the assumptions that will be made during the development of theoretical models.

Furthermore the author participated to a SUPERGEN marine project in partnership with Cambridge University. For this project a test rig to be used in the IFREMER circulating water tank in France was designed and built from scratch. Alongside the main aim of studying control strategies to mitigate the dynamic loads due to turbulence, the author was able to extrapolate data for the turbine model validation and so doing compensate for the unavailability of data from the DeltaStream project.

The idea behind this doctorate work is providing a deeper understanding on how horizontal axis hydrokinetic turbines interact with turbulence generated both by environmental factors, namely the boundary layer and the influence of waves, and the presence of similar devices. This interaction can be either due to closely spaced turbines, as is the case of Deltastream, and/or from other turbines operating in a farm structure.

There is an extended literature on the subject of interaction in wind turbines [61] but not all of the techniques developed this far are applicable to the world of tidal hydrokinetic energy extraction.

Therefore the aim of the project is to develop a validated model that will enable the characterization of the flow, and hence of the structural loads, that apply to the device when operating in realistic conditions.

This aim is to be achieved through the following objectives:

- Employ a hybrid CFD-BEM model to describe the loads and performance of a horizontal axis tidal turbine.
- Implement a model for turbulence that takes into account the specificities of tidal channel flows.
- Build-up a collection of routines, scripts and procedures in order to compute loads on the device when exposed to a turbulent field.
- Obtain experimental data from the sea trials and additional model tests to validate the theoretical models.

1.3.1 Thesis Project Overview Scheme

Motivation

- water high density fluid
- underwater maintenance

hydrokinetic tidal turbines suffer turbulence induced fatigue

Current simulation tools

- Blade element momentum –> no complex flow prediction
- Computational Fluid dynamics

RANS –> turbulent effects only averaged

LES –> computationally expensive

- inflow generators –> not capable of space and time correlation

need for turbulent-resolved but lightweight simulation tool

Workflow

Numerical

OpenFOAM C++ libraries
circa 20.000 C++/Matlab/Python code lines
development of

- Inflow Generators (Novel)
- Hybrid Blade Element/CFD approach

Experimental

Cambridge SUPERGEN project

- water Tank Experimental Campaign design and realisation

Tidal channel data analysis

Achievements

- Hybrid Blade Element/CFD approach Validation
- Prediction of turbine dynamic load given specified inflow

Contribution to knowledge

- observations on tidal channel flows
- inflow generation method large impact on turbine load signature
- novel inflow generator methodology

1.4 Thesis Format

The thesis is organised into 11 chapters and 4 main overarching parts. The first part introduces the reader to the topics of this project, the second one describes the Literature Review and Theoretical Background, the third illustrates the Methodologies adopted and the final Results and Conclusions.
Follows a brief description of the content of each chapter.

Chapter1 contains a succinct introduction to the thesis topic and to the device that was at the centre of the current project, the DeltaStream turbine. The Aims and Objectives of the work are presented.

Chapter2 presents a literature review on the main models available for the representation of open rotor turbine hydro and aero-dynamics

Chapter3 describes the theoretical substrate to the work for what concerns the statistical tools used in the turbulent inflow generators

Chapter4 deepens the Proper Orthogonal Decomposition methodology used by the author for the novel inflow generator and the Ramsey Sound ADCP data analysis

Chapter6 presents a description of the test rig used in IFREMER

Chapter7 illustrates the developed inflow generators and actuator line model within OpenFOAM

Chapter9 shows the actuator line model validation vs the experimental data collected

Chapter8 applies the POD technique to the analysis of the Ramsey Sound Data and shows the results from the IFREMER experimental campaign

Chapter10 illustrates the flow fields produced making use of the implemented inflow generators in OpenFOAM and the produced signal trace on the turbine rotor axis

Chapter11 summarises the main achievements and suggestions for further works

1.4.1 Thesis Map

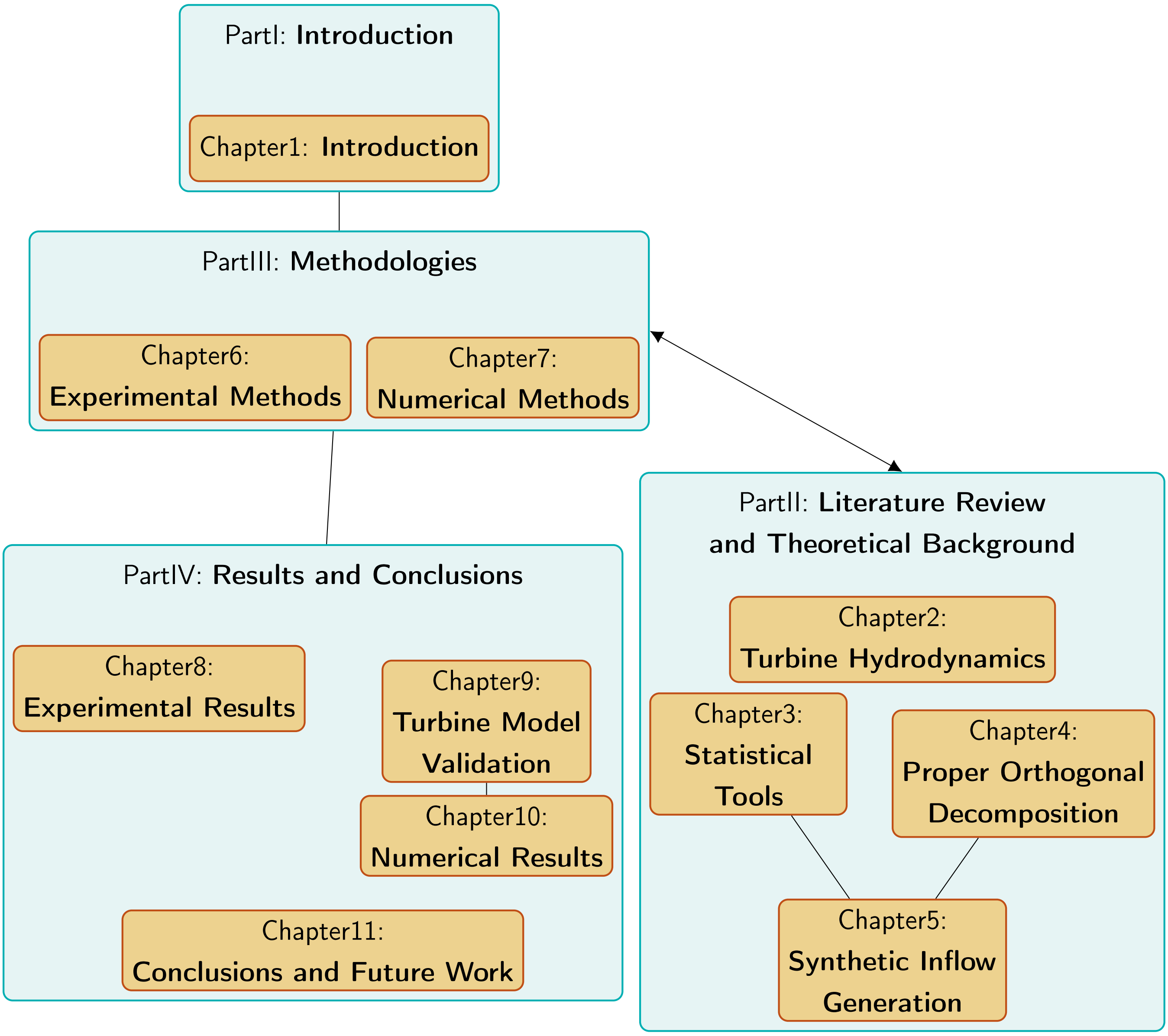

Part II

Literature Review and Theoretical Background

Chapter 2

Turbine Hydrodynamics

The aerodynamics of a open rotor turbine like the hydrokinetic tidal turbines is all that concerns the interaction between the mechanical parts of the turbine and the water investing it. The interest is focused in particular on forces exchanged being those responsible for the power production and the mechanical design of the structure both in terms of maximum and fatigue loads.

A particular importance is given to the event of the stall being this used, in particular in relatively small devices as a design instrument to reduce the loads when those result higher than the ones considered feasible and economically convenient for the construction of the machine.

In the present chapter, first in section 2.1 the main descriptors of performance are reported. In 2.2 the currently mostly utilised methods by both the industry and the academia are summarised. Finally section 2.3 describes a category of methodologies of recent development making use of CFD in combination with applied bulk forces. These represent the presence of a body in the computational domain by the forces exchanged with the field rather than via producing a boundary surface in the mesh.

2.1 Performance Coefficients

In order to estimate the performance of a horizontal axis tidal turbine the wind turbine experience is used. In fact the two devices work according to the same operational principles.

Applying the Buckingham theorem to the aerodynamics of the turbine one can deduce the principal non-dimensional group involved in the power production: the coefficient of power

$$C_P = \frac{P}{\frac{1}{2}\rho A u_{up}^3} \tag{2.1}$$

where ρ is the air density, u_{up} is the wind speed and A is the area occupied by the rotor during the rotation.

A significant role is played by the thrust coefficient as well, being representative of the thrust on the rotor plane due to the pressure drop caused by the energy extraction from the flow.

$$C_T = \frac{T}{\frac{1}{2}\rho A u_{up}^2} \tag{2.2}$$

These coefficients, where the hypothesis behind the non-dimensional theory are respected, are dependent on the speed at the tip of the blade $\Omega \cdot r$ with r radius of the tip and ω rotational speed, non-dimensionalised by the wind speed u_{up}

$$\lambda = \frac{\Omega r}{u_{up}} \tag{2.3}$$

called tip speed ratio (TSR).

In the following of the current chapter the methodologies used for the calculation of loads and performance of hydrokinetic open rotor tidal turbines are presented.

For the aim of this project, methods can be divided in two categories:

- single turbine design methods
- farm models

Those are receptively illustrated in section 2.2 and 2.3. For the basic theory one can refer to the Hansen book [30], which will not be cited in what follows, but it provided the framework of this part.

2.2 Traditional Methods

2.2.1 Actuator Disk

In the actuator disk models a open rotor the machine, like a propeller or a turbine, is described as a circular ideal surface of discontinuity in the flow.

The effects of viscosity are not directly taken in account and they can be included using corrective factors.

1D Description This description assumes the flow through the rotor as having pure axial direction. Writing the equations for the flow in the control domain represented by two stations surfaces sufficiently upstream ($_{up}$) and downstream ($_{dw}$) the rotor and the envelop of all the streamlines [1] passing via the perimeter of the rotor disk ($_d$) one can write:

- continuity equation

$$\dot{m} = \rho A_{up} u_{up} = \rho A_d u_d = \rho A_{dw} u_{dw} \tag{2.4}$$

- force exerts on the disk

$$T = \dot{m}(u_{up} - u_{dw}) = \left(p_d^+ - p_d^-\right) A_d \tag{2.5}$$

- momentum equation

$$E = \frac{1}{2} m \left(u_{up}^2 - u_{dw}^2\right) = T u_d \tag{2.6}$$

where p_d^+ and p_d^- are respectively the pressure immediately upstream and downstream the the rotor discontinuity. Combining the above equations one can find that the rotor speed is $u_d = \frac{1}{2}\left(u_{up} + u_{dw}\right)$. Introducing the axial induction factor $a = 1 - \frac{u_d}{u_{up}}$, C_P and C_T can be rewritten as

$$C_P = 4a(1-a)^2 \tag{2.7}$$

$$C_T = 4a(1-a) \tag{2.8}$$

[1] the fluid always move parallel to streamlines

. The optimum $C_P = 16/27 \backsimeq 0.59$ is reached for $a = 1/3$. This value represents the maximum energy fraction that is possible to extract from the undisturbed upstream flow. The higher the C_T is, the deeper the wake will be, with the Δp across the disk being larger.

Tangential effects due to the rotation imposed to the flow by the rotative motion of the turbomachine can be introduced considering a tangential induction factor $a' = u_t/\Omega r$. The total velocity angle ϕ with respect to the tangential direction results

$$\tan\phi = \frac{u_{up}(1-a)}{\Omega r(1+a')} \tag{2.9}$$

. The angle of attack α on the blade profile follows

$$\alpha = \phi - \theta \tag{2.10}$$

where θ is the pitch angle of the blade. Thrust and torque can be derived than from lift and drag for a certain flow direction [61].

Blade-Element Momentum The traditional and most developed tool for design of open rotors is the so-called BEM approach.

It is derived from

- blade element theory, consisting in the decomposition of the blade independent span element having an airfoil behavior and,
- momentum theory (also called Euler theory), which states that the energy exchanged between the machine and the fluid is proportional to the change in momentum of the latter

Applied to an open rotor machine it means that the actuator disk is divided into annular sections. One can find that for each section [30] thrust and torque will depend on lift and drag on the airfoil according to the next

$$dT = B\frac{1}{2}\rho U\left(C_l\cos\phi + C_d\sin\phi\right)cdr \tag{2.11}$$

$$dQ = B\frac{1}{2}\rho U\left(C_l\sin\phi - C_d\cos\phi\right)cdr \tag{2.12}$$

where U is the velocity magnitude, c is the chord length, C_l and C_d are lift and drag coefficients of the local airfoil, B the number of blades and dr the infinitive increment in the radius coordinate. From the Eulerian it is possible to obtain

$$dT = 4\pi r\rho u_{up}^2(1-a)adr \tag{2.13}$$

$$dQ = 4\pi r^3\Omega\rho u_{up}(1-a)a'dr \tag{2.14}$$

These equations together with (2.9) and the lookup tables for C_l and C_d depending on the angle of attack, represent a complete set that can be iteratively solved to obtain torque and thrust.

The BEM presents several limitation among which one can list the following

- static calculations
- no flow in radial direction
- no finite-span effects
- no turbulent wake state modeling
- no skewness effect

Despite the strong approximation that this model introduces on the real behavior of the turbine it is still the most used for the engineering purposes. This is because its quickness and maturity: Lots of corrective factors to overcome the limitations have been introduced during the last century.

- Glauert Correction
- time lag
- tip and hub loss models
- Beddoes and Leishman 1989 dynamic stall

Vorticity-Based Methods These methods try to overcome the difficulties that the BEM presents in modeling dynamic effects, tip losses, non-infinite number of blades and 3D effects. The turbulent wake state, that requires a strong correction in the Glauert theory [30] here is automatically computed by the model[70] .

On the other end they usually present a lower stability and still need corrections to take in account for the viscosity contribution [61].

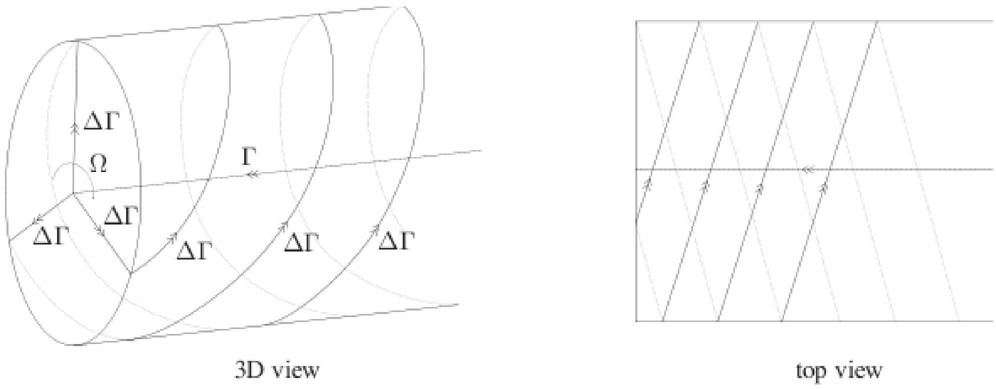

Fig. 2.1 Vortex system on 3-bladed turbine [55]

Lifting Line According to the Kutta–Joukowski theorem the lift on a body can be calculated as

$$L = \rho u_{up} \Delta\Gamma \tag{2.15}$$

where $\Delta\Gamma$ is the circulation of the velocity around the body. For the Kelvin Theorem, when its hypothesis are respected, it is true that

$$\frac{D\Gamma}{Dt} = 0 \tag{2.16}$$

Thus any bound vortex $\Delta\Gamma$ must be compensated by a vortex of the same strength downstream. The system of vortexes due to the work of a turbine in the flow is represented in Fig.2.1

The strength of the vortex on the blade is still calculated from a lookup table of values for the lift according to

$$\Delta\Gamma = \frac{1}{2} C_l c U \tag{2.17}$$

Two possible approaches are possible:

- prescribed vortex
- free wake

The first imposes the position of the vortical elements being more robust but less flexible the second allows to compute dynamic and skewed flows but presents numerical instabilities. In fact it requires the discretized solution ofArray of Turbines Design Methods a generalized potential problem governed by the same equations as the electro-magnetism problem where a scalar potential accounts for the undisturbed flow and a vectorial one for the vorticity induced by the bodies in the flow [70].

2.2.2 Navier-Stokes Equations

Solving the equations for the dynamics of a newtonian fluid it is theoretically sufficient to know everything about the forces exerted by the flow on the turbine. This approach is the most computationally expansive one because the model part of the problem compared to the calculated one is minimum.

The general form of the continuity, momentum and energy of the Navier-Stokes equations is shown in (2.18) and (2.19).

$$\nabla \cdot \mathbf{v} = \mathbf{0} \tag{2.18}$$

where

v is the vectorial velocity field and

∇ is the gradient operator

$$\rho \left(\frac{\partial \mathbf{v}}{\partial t} + \mathbf{v} \cdot \nabla \mathbf{v} \right) = -\nabla p + \mu \nabla^2 \mathbf{v} + \mathbf{f} \tag{2.19}$$

where p is the pressure, μ the viscosity, $\mathbf{f}$ the body forces and ∇^2 the laplacian operator.

Turbulent flows present deterministic chaotic, multiscale and unsteady features [53]. This makes unfeasible the solution of the discretized equations in a numerical calculator with the present computational resources. It is required part of the flow to be modeled rather than solved. Two main possible techniques are possible:

- time filter RANS
- space filter LES

The former consists in solving the equations for the average field supposing to have a big enough number of experiments and ensembling their results. The latter applies a sub-grid viscosity accounting for the part of the flow that is not solved. One can say that in order to understand the unsteady mechanical loading of a structure the second methodology result more suitable. It is true that the structure is affected by the behavior of the fluid eddies only above certain scales and all the small ones result having a zero global effect on the turbine.

Vorticity Equation In the solution of the N-S equations coupling between the continuity and momentum equation is needed. An elegant way of resolving this problem is writing the formulation for the vorticity [34].

On one hand that eliminates the problem of the coupling and provides an immediate description of the lifting properties of the turbine but on the other hand it introduces difficulties in modeling viscosity and turbulence. Furthermore numerical instabilities are usually generated by the boundary layer conditions.

Potential Solvers This category of model is represented by a vast range of solvers whose aim is presenting the solution in terms of integral function from which pressure and velocity distributions can be derived.

Generalized Dynamic Wake The aim of this model is having an embedded model for tip losses, dynamic and time lag effects and skewed wake aerodynamics. Under the hypothesis of inviscid flow and small perturbations (2.18) reduces to the Laplace's one for the pressure

$$\nabla^2 p = 0 \tag{2.20}$$

This can be solved analytically and the pressure can be substituted in the Euler equation for external flows being the (2.19) once the viscosity term is neglected [52].

2.2.3 Panel Methods

Under panel methods are all of the methodologies that use the Green Functions to write the potential formulation of the flow problem at its boundaries. Therefore problem can be solved decomposing the boundary surfaces in panels i.e. a 2D grid. The viscosity effects must be considered separately in the form of solution of the equations for the boundary layer.

An interesting ongoing project is under development in ECN [2] Using a 3D boundary elements method allows to take in account all the 3D effects in the model itself but still

[2]Energy research Centre of Netherlands

allowing shorter solution times than N-S resolution [14]. A computational hydrodynamics method for horizontal axis turbine . Panel method modeling migration from propulsion to turbine energy can be found in [44].

2.2.4 Conclusions

A brief introduction to most of the methodologies for solving the the problem of the aerodynamics of an open rotor turbine have been reported.

If the N-S and Panel Methods not require experimental data, all of the other methods relay on lookup tables for lift and drag forces on 2D sections of the turbine. 3D effects must usually be introduced in each case in order to match the experimental reality.

A deeper description of these problematics can be found in [67] and [71].

Recently more accurate experiments and studies seem to highlight how the basic assumptions of most of the models are questionable. A treatment of these matters is in [61].

2.3 Hybrid Methods

Decades of experience have been accumulated in designing open rotor turbines, especially for wind generation, and a wide collection of empirical models are available, still a full understanding of all of the phenomena behind the turbines behavior has not been achieved.

It is expected that the N-S techniques will play a rising role in the future in order to develop more optimized turbine. It is anyway true that the current computing resources are not sufficient for the solution of a farm of devices.

In order to overcome both the limitations of the actuator disk on one side and the full N-S simulations on the other hybrid methods have been so developed.

This can be grouped under four main categories:

- actuator disk
- actuator line
- actuator surface

Actuator Disk Hybrid Actuator Disk Models consist in the introduction of a Actuator Disk as described in section 2.2.1 where the axial induction a is obtained by interrogating the CFD-generated field. One can find an example in the standard OpenFOAM distribution routines under the name of "actuationDislSource". They are in general quite simplistic and only compute the blockage due to the turbine presence. In general it is of little use for resolved turbulence simulations such as LES but it could quickly provide a way to compute the device power when downstream other turbines or orographic elements.

2.3.1 Actuator Line

These methods consist in N-S solver coupled with a model taking in account for the behavior of each blade. They have been developed in recent times, being the initiator Sorensen, who solved the equation of the fluid for the vorticity as introduced in paragraph 2.2.2 coupling with a model where the element of the blade exert a body force on the flow field equal to lift and drag calculated according to the lookup tables. A extensive treatment of the method can also be found in the Mikkelsen Ph.D. thesis [51].

A regularization kernel is then used to impose the force to the elements of the grid according to the next

$$F_i^A(x,y,z,t) = -\sum_{j=1}^{N} f_i^A(x_j,y_j,z_j,t)\frac{1}{\varepsilon^3\pi^{3/4}}\exp\left[-\left(\frac{d_j}{\varepsilon}\right)^2\right] \tag{2.21}$$

[19, 20, 69, 74] where $F_i^A(x,y,z,t)$ is the force on the i grid cell due to the effects of the presence the j blade element at a distance equal to d_j.

One can recognize in the above formula the Gaussian normal distribution. The value ε that appears, regulate the width of the function. On one hand this value must be connected with the cord length of the turbine but on the other it has to be sufficiently large for convergence. The compromise between the two necessities leads to an arbitrary choice that requires to further investigated by the authors too.

The method just described consists in a blade element method, i.e. the aerodynamics of the turbine is calculated on 2D section and than projected in to the flow. The part that in the BEM is played by the momentum equation in the calculation of the induction factors here is replaced by a full 3D transient solver for the N-S, hence taking in account all the non-static effects that in the BEM are neglected and reintroduced in terms of correctors. In fact the inducted velocity in the field is extracted from the flow at the location where the blade is passing at a certain time.

This easily allows to consider effects of turbulent inlet, blade misalignment or yaw, complex terrain, free surface flow, presence of other turbines, etc. The blade element part takes care of solving the aerodynamics and the N-S part provides all of the complex physics like

- free surface tracking
- sea bed boundary layer effects
- turbulent inlet conditions

The main weakness of the model is the determination of an appropriate value for ε and the shape of forces exert on the flow does not represent the physical reality.

This model is good enough for producing quality far wake results where the effects of evolving localized vortexes is no longer visible. In the case of the object of this study the axial spacing between the upstream devices and the downstream one is less than three rotor diameters where the upstream turbine fine vortexes production still plays an important role.

2.3.2 Actuator Surface

In order to produce a better quality wake a new category of model have been developed by [74, 23, 15].

The idea behind is that the blade acts on the flow not as a line constituted by point forces but as a surface where each 2D profile is modeled as line of points. The upstream sampled velocity extracted for the Blade Element computation result more realistic improving not only the model performance in producing a quality wake but also the blade aerodynamics model. As an obvious drawback the number of nodes required to describe the flow will increase.

Body Forces In [74] the effect of the blade is still computed in terms of forces on the N-S mesh. The distribution of forces over a line is computed using XFOIL and fitting functions among the results. This methodology still allows an almost mesh independent approach and a gives to the pressure distribution around the airfoil a more similar shape when compared

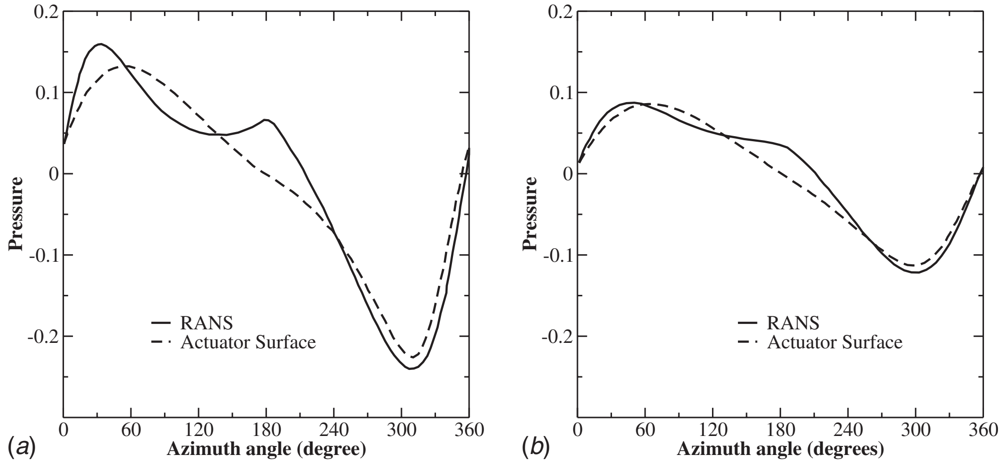

Fig. 2.2 Pressure distribution on two ellipsoidal lines around a NACA0015 airfoil for $Re = 10^6$ and $\alpha = 10$ as defined in [74]

to N-S simulations. In Fig.2.2 the pressure distribution around the airfoil is shown against RANS computation. The results show a good agreement even if local peaks are smoothed.

Pressure Loss In [23] the airfoil is replaced by a straight line in the flow. They claim to save $9/10$ of the grid size moving from RANS to their actuator surface model. The velocity from the flow field is used to evaluate point forces by a GDWT methodology but, differently from Sorensen, they convert these in pressure jump decomposing the force into an heuristic distribution of pressure between pressure and suction side as reported in Fig.2.3.

This strategy is implemented in FLUENT using a "fan“ boundary condition. A line patch in the mesh is so required where to apply the pressure jump. As a consequence a specific mesh for each turbine is required reducing the flexibility of the model when coping with rotating turbine and control systems like the pitch and yaw one. In fact mesh grid interfaces will be required making the simulation more expensive in terms of computational time and less reliable.

The velocity field around the airfoil in use by [23] is plotted against a RANS computation in Fig.2.3.

One can notice that even only from a qualitative point of view the contours show pretty different patterns. This is probably due to the simplistic function used to distribute the pressure drop on the line, and the fact that no effects parallel to the line are taken in account.

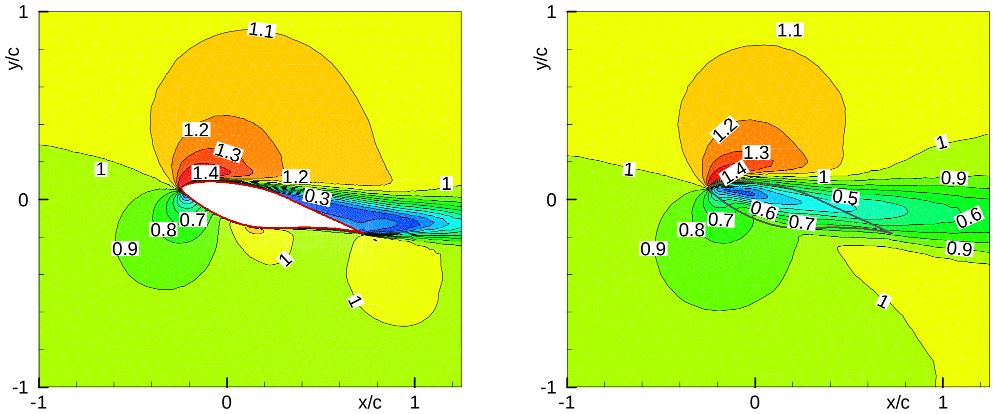

Fig. 2.3 Velocity field for S809 airfoil for $Re = 10^6$ and $\alpha = 15$ as defined in[23]

Porous Surfaces The model proposed by [15] is meant to overcome the difficulties encountered in both the Body forces and the ”fan“ boundary condition approach.
A porous surface is included in the model of a surface where they impose velocities discontinuities that respect a potential over a volume that is reported to a surface using the Green theorem. This approach is similar to a panel method from this point of view, but the actual circulation over the surface is derived from tabulated airfoil data and parallel Δu and orthogonal Δv velocity jumps across the surface are imposed in the form of heuristic functions. Δu is equal to a parabolic function

$$\Delta u_P = \frac{6\Gamma}{c^3} x_P (c - x_P) \tag{2.22}$$

where x_p is the distance of the point from the leading edge. The Δv distribution is enforced by the respect of the potential.

As shown in Fig.2.4 the methodology fails in the prediction of the C_P for the test case of the TUDelft Rotor

2.4 Methods Comparison and Selection

In the present chapter the author described a number of methodologies for the evaluation of open-rotor turbines hydrodynamics. Being this project originated from the need of describing both:

- the tidal channel turbulence inflow and
- the effect in closely spaced devices of the wake from an upstream turbine,

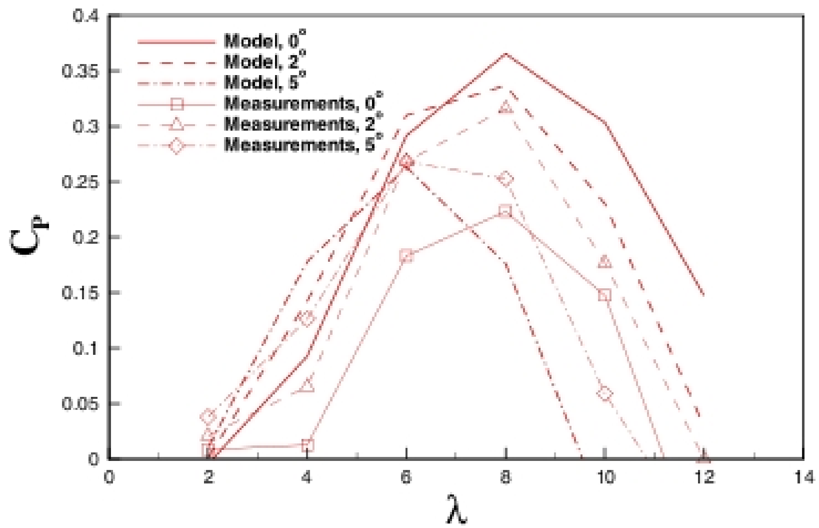

Fig. 2.4 Numerical and Experimental Results for the TUDelft Rotor from [15]

the methodologies intrinsically capable of describing both are the

- turbulence resolved Navier-Stokes equations (LES) and
- hybrid methods.

The former are well known in literature for being extremely computationally expensive [7], the latter constitutes a compromise between the need of describing dynamic load and computational time. This has been already used by Churchfield [20] specifically for the study of closely spaced tidal turbines.
The author then selected the second method for the present study. In table 2.1 the turbine performance analysis studies are compared side by side showing the main features. For the simulation and readiness line the + symbols represent the performance judgment. For the rows one to seven:

- − stands for unfeasible,
- + means that it requires empirical corrections,
- ++ is indicated when the method is suitable and finally
- +++ is shown in case of good performance of the method.

One can see how the best overall scoring method hence the selected one for this study is the Hybrid Actuator Line. Its relatives hybrid Actuator disk and surface lack the former of

Feature	Method								
	Actuator Disk	BEM	Lifting Line	RANS	LES	Panels	Hybrid Disk	Hybrid Line	Hybrid Surface
Time Turbulence	+	+	+	-	+++	+	++	++	++
Space Turbulence	-	+	+	-	+++	+	-	++	++
3D effects	-	+	+	+++	+++	+++	-	++	++
outer boundaries effect	-	+	+	+++	+++	+	++	+++	+++
viscous effects	-	+	+	++	+++	+	+	++	++
wake evolution	-	-	++	++	+++	++	+	++	++
blade near flow	-	-	+	+++	+++	+	-	+	++
simulation time	+++	+++	+++	+	-	++	++	++	++
readiness	+++	+++	++	+++	++	++	++	++	-

Table 2.1 Turbine Hydrodynamics methodologies features and selected method in gray

accuracy in the spacial description and the latter of readiness. In fact in order to describe the near blade flow a set of prescribed pressure functions across the line depending on the direction and intensity of the inflow has to be provided. Also the level of fidelity provided is actually not necessary for the scope of this work.

Chapter 3

Statistical Tools

This chapter describes two statistical methodologies that will be useful for the understanding and implementation of the LES inflow methods.

- The spectral representation method is presented in section 3.1 and
- the autoregressive moving-average model in section 3.2

These tools have been fundamental for the implementation of the inflow generators described in chapter 5 and section 7.1. The former consists in a mixed approach making use of functional analysis and random generation in order to produce multidimensional fields with given statistical correlation properties. The latter is a procedure that makes use of filtering of randomly generated signals in order to obtain correlated ones.

3.1 Spectral Representation Method

Turbulence as stochastic process has always been of successful modelling approach since Kolmogorov theorised it in 1941 [38]. It is then reasonable and historically proven to describe the behaviour of a fluctuating field by its spectral content.
Shinzuka and Deodatis presented a technique of simulation of stochastic processes by spectral representation back in 1991 [56] and then extended it to multi-dimensional field [57]. Their work is limited to homogeneous fields. The author will present an original extension to non-homogeneous fields in the methodologies part .
It is then a reasonable assumption that such work can be used for the production of a turbulent field. The present chapter mostly refers to the two above papers.
In the following, first a description of the technique applied to a 1-D signal is presented and then its extension to fields.

3.1.1 One dimensional process

$f_0(t)$ is a process having respectively zero mean and given covariance

$$\varepsilon[f_0(t)] = 0 \tag{3.1}$$

$$\varepsilon[f_0(t+\tau)f_0(t+\tau)] = R_{f_0f_0}(\tau) \tag{3.2}$$

where $\varepsilon[\,]$ represents the scalar product and the power spectral density $S_{f_0f_0}(\omega)$ results the Fourier transform of the covariance $R_{f_0f_0}(\tau)$ according to the

$$S_{f_0f_0}(\omega) = \int_{-\infty}^{\infty} R_{f_0f_0}(\tau)e^{-\iota\omega\tau}d\tau \tag{3.3}$$

$$R_{f_0f_0}(\tau) = \int_{-\infty}^{\infty} S_{f_0f_0}(\omega)e^{\iota\omega\tau}d\omega \tag{3.4}$$

In accordance with the general Fourier theory, every stationary, presenting zero mean process can be written in the form

$$f_0(t) = \int_0^{\infty} [\cos(\omega t)du(\omega) + \sin(\omega t)dv(\omega)] \tag{3.5}$$

where $du(\omega)$ and $dv(\omega)$ are orthogonal, in the sense of the product $\varepsilon[]$, increments of two one with the other orthogonal processes $u(\omega)$ and $v(\omega)$.
If the process is also periodic then it is possible to pass from the integration to the sum and write equation (3.5) as

$$f_0(t) = \sum_{k=0}^{\infty} [\cos(\omega_k t)du(\omega_k) + \sin(\omega_k t)dv(\omega_k)] \tag{3.6}$$

with

$$\omega_k = k\Delta\omega \tag{3.7}$$

. Furthermore if we plug two orthogonal processes in the functional analysis sense,

$$du(\omega_k) = \sqrt{2}A_k\cos\Phi_k, \tag{3.8}$$

$$dv(\omega_k) = -\sqrt{2}A_k\sin\Phi_k \tag{3.9}$$

living in the wavenumbers domain and having their amplitude set appropriately in order to match the time (space) spectral content

$$A_k = \left(2S_{f_0 f_0}(\omega_k)\Delta\omega\right)^{(1/2)} \tag{3.10}$$

. Then a uniform stochastic distribution of values for

$$\Phi_k \sim \mathcal{N}(0, 2\pi) \tag{3.11}$$

which is a simple numerical task in modern days (for example MATLAB's randn function) is produced and introduced in the series.
The obtained $f_0(t)$ process presents ergodic features, hence:

- possesses same mean value and
- autocorrelation function and power spectra density

as the originally considered signal over an integer numbers of periods of the harmonic functions. Differently aliasing would appear. The last considerations can be found demonstrated in [56].
In other words we are using the intrinsic power of the Fourier representation, by setting appropriately amplitudes and having uniformly distributed randomness of the phases and having as an output a much more meaningful process in the real time or space domain.

The final simulation formula is deduced by introducing (3.9) and (3.9) into (3.6):

$$f(t) = \sqrt{2}\sum_{k=0}^{N-1} A_n \cos\left(\omega_n t + \Phi_n\right) \tag{3.12}$$

where

$$A_n = \left(2S_{f_0 f_0}(\omega_n)\Delta\omega\right)^{(1/2)}, \tag{3.13}$$

$$\omega_n = n\Delta\omega, n = 0, 1, 2, ..., N-1 \tag{3.14}$$

. If $N \to \infty$ then (3.14) coincides with (3.6). Shinozuka and Deodatis [56] also demonstrate that $A_0 = 0$ for the ergodic and zero-mean properties to be respected.
The so-obtained signal presents Gaussian statistical distribution properties.

3.1.2 Multidimensional process

The above mentioned authors presented in 1996 a review of the spectral representation method extended to a multi-dimensional case [57]. The general formulas obtained are reported and explained here.
A process $f_0(\mathbf{x})$ with $\mathbf{x}$ being a m-dimensional vector is considered. The correlation functional is assumed to respect the following condition of symmetry for the power spectral density:

$$S_{f_0 f_0}(\kappa) = S_{f_0 f_0}(-\kappa) \tag{3.15}$$

in the wavevectors κ domain and its dual condition on the correlation

$$R_{f_0 f_0}(\xi) = R_{f_0 f_0}(-\xi) \tag{3.16}$$

in the real space of vector separations ξ. This is perfectly suitable for the description of homogeneous turbulence under the assumption of the Taylor hypothesis: a 4-dimensional field might be considered. 3-homogeneous space directions can be represented as such [53], the fourth one is time. According to the Taylor hypothesis on turbulence, time and space are in a linear correlation given by the average velocity of the flow. The latter is in general not respected [64],[73] for highly turbulent environmental flows but it is a reasonable assumption of common use in engineering. If the above can be used then it is sufficient a Galilean transform to bring the case to a 4-D wavevectorial description. Furthermore the $f_0(\mathbf{x})$ has mean values equal to zero. (It is easy to recover from this limitation by just adding a constant). Given the above assumptions, a stochastic field can be simulated utilising the formulation in the following (3.17).

$$\begin{aligned} f(x_1, x_2, \ldots, x_m) = &\sqrt{2} \sum_{n_1=0}^{N_1-1} \sum_{n_2=0}^{N_2-1} \cdots \sum_{n_m=0}^{N_m-1} \sum_{I_1=1, I_i=\pm 1, i=2,3\ldots,m} \\ &\sqrt{2 S_{f_0 f_0}(I_1 \kappa_{1n_1}, I_2 \kappa_{2n_2}, \ldots, I_m \kappa_{mn_m}) \Delta\kappa_1 \Delta\kappa_2 \ldots \Delta\kappa_m} \\ &\cos(I_1 \kappa_{In_1} x_1 + I_2 \kappa_{2n_2} x_2 + \cdots + I_m \kappa_{mn_m} x_m + \Phi_{n_1 n_2 \ldots n_m}^{I_1 I_2 \ldots I_m}) \end{aligned} \tag{3.17}$$

this would approach the actual process $f_0(\mathbf{x})$ for $N_1, N_2, \ldots, N_m \to \infty$.
Wavenumbers are obtained by multiplication of a fixed length $\Delta\kappa_i$ by an incremental integer n_i according to:

$$\kappa_{1n_1} = n_1 \Delta\kappa_1, \kappa_{2n_2} = n_2 \Delta\kappa_2 \ldots \kappa_{mn_m} = n_m \Delta\kappa_m \tag{3.18}$$

Same as for the 1-D case correlation at zero distance must be equal to zero, hence:

$$\begin{aligned} &S_{f_0f_0}(I_1\kappa_{1_0}, I_2\kappa_{2n_2}, \ldots, I_m\kappa_{mn_{n/}}) = S_{f_0f_0}(I_1\kappa_{In_1}, I_2\kappa_{20}, \ldots, I_m\kappa_{mn_m}) = \\ &S_{f_0f_0}(I_1\kappa_{In_1}, I_2\kappa_{2n_2}, \ldots, I_m\kappa_{m0}) = 0 \end{aligned} \quad (3.19)$$

. The indexes variation is described by the following two

$$I_1 = 1, I_i = \pm 1, i = 2, 3, \ldots, m \quad (3.20)$$

$$n_1 = 0, 1, \ldots, N_1 - 1; n_2 = 0, 1, \ldots, N_2 - 1; \ldots; n_m = 0, 1, \ldots, N_m - 1 \quad (3.21)$$

. The rationale behind this methodology is making use of the same functional space of cosines functions and spectral amplitudes as the desired process. A specific simulation can then be produced by introducing randomly uniformly distributed phases Φ in the interval $[0, \pi]$. A background on the Fourier representation theory can be found in [8]. The above described technique can be seen as a random producer of phases for intrinsic orthonormal complete set of functions (here cosines) in which the time-space reality can be decomposed. In other words the uniform randomness in the wavevectors domain, becomes coherent statistics in time-space. One further consideration can be done on the periodicity of the proposed representation. When passing from continuous to discrete steps $\Delta\kappa_j$, contingently the signal will become periodic of period $L_{x_j}0 = \frac{2\pi}{\Delta\kappa_j}$ along the x_j axis. This is due to the nature of the harmonic functions. A simplification can additionally be applied when introducing a stronger symmetry assumption then the (3.15),(3.16). One could consider a symmetry valid component-by-component

$$S_{f_0f_0}(\kappa) = S_{f_0f_0}(\mathbf{I}_{\pm}\kappa) \quad (3.22)$$

$$R_{f_0f_0}(\xi) = R_{f_0f_0}(\mathbf{I}_{\pm}\xi) \quad (3.23)$$

with $\mathbf{I}_{\pm}$ a diagonal matrix of ones whose signs are a whichever combination of positive and negative. Under the above (3.17) can be rewritten as

$$\begin{aligned} f(x_1, x_2, \ldots, x_m) = &\sqrt{2} \sum_{n_1=0}^{N_1-1} \sum_{n_2=0}^{N_2-1} \cdots \sum_{n_m=0}^{N_m-1} \sum_{I_1=1, I_i=\pm 1, i=2,3\ldots,m} \\ &\sqrt{2S_{f_0f_0}(\kappa_{1n_1}, \kappa_{2n_2}, \ldots, \kappa_{mn_m})\Delta\kappa_1\Delta\kappa_2\ldots\Delta\kappa_m} \\ &\cos(I_1\kappa_{In_1}x_1 + I_2\kappa_{2n_2}x_2 + \cdots + I_m\kappa_{mn_m}x_m + \Phi_{n_1n_2\ldots n_m}^{I_1I_2\ldots I_m}) \end{aligned} \quad (3.24)$$

This assumption makes much simpler the evaluation of the spectral amplitudes. They are so obtained from the power spectral density functional in its positive range also called one-sided PSD function.

2-D and 3-D Processes The reader can find below the equation (3.24) specified for $m = 2$ and 3 respectively in (3.25) and (3.26). These will return useful in the following of this thesis dissertation and make more clear the above formulation for more practical cases.

$$\begin{aligned} f(x_1,x_2) =& \sqrt{2}\sum_{n_1=0}^{N_1-1}\sum_{n_2=0}^{N_2-1}\sqrt{2S_{f_0f_0}(\kappa_{1n_1},\kappa_{2n_2})\Delta\kappa_1\Delta\kappa_2} \\ & \left[\cos(\kappa_{1n_1}x_1+\kappa_{2n_2}x_2+\Phi^1_{n_1n_2})+\cos(\kappa_{1n_1}x_1-\kappa_{2n_2}x_2+\Phi^2_{n_1n_2})\right] \end{aligned} \tag{3.25}$$

$$\begin{aligned} f(x_1,x_2,x_3) = & \sqrt{2}\sum_{n_1=0}^{N_1-1}\sum_{n_2=0}^{N_2-1}\sum_{n_3=0}^{N_3-1}\sqrt{2S_{f_0f_0}(\kappa_{1n_1},\kappa_{2n_2},\kappa_{3n_3})\Delta\kappa_1\Delta\kappa_2\Delta\kappa_3} \\ & \left[\cos(\kappa_{1n_1}x_1+\kappa_{2n_2}x_2+\kappa_{3n_3}x_3+\Phi^1_{n_1n_2n_3})\right. \\ & \cos(\kappa_{1n_1}x_1-\kappa_{2n_2}x_2+\kappa_{3n_3}x_3+\Phi^2_{n_1n_2n_3}) \\ & \cos(\kappa_{1n_1}x_1+\kappa_{2n_2}x_2-\kappa_{3n_3}x_3+\Phi^3_{n_1n_2n_3}) \\ & \left.\cos(\kappa_{1n_1}x_1-\kappa_{2n_2}x_2-\kappa_{3n_3}x_3+\Phi^4_{n_1n_2n_3})\right] \end{aligned} \tag{3.26}$$

3.2 Autoregressive-moving-average Model

The autoregressive moving-average filter model is a mathematical technique providing step-by-step a vectorial process X_t of cross and auto correlated variables i.e. variables depending on their own time history and on the others' starting from a white noise array namely ε_t. The ARMA methodology is adopted by Hœpffner and al. [33] for the generation of multiplicative terms associated to a particular function representing a flow structure. A more detailed description can be found in section 5.4.1. It is generally used in the description of mechanical, hydraulic and electronic models and in the study of historical series and economics. Differently from the previously illustrated method it does not have a functional basis such as the Fourier one, but purely algebraic. Compared to the spectral representation method where white noise is passed as phases Φ for the harmonic functions of the Fourier series, the produced output is an array of variables not necessarily associated to any spacial position and it is not a field (function of space). Outputs X_t are a linear combination of the values assumed by

- the uniform random input ε_t and
- themselves at the past steps.

As a consequence such models can be analysed with relative ease when compared to others even though presenting a relatively high level of fidelity. They have

- the property of linearity hence additivity $X(\varepsilon)+Y(\varphi)=Z(\varepsilon+\varphi)$ and homogeneity of degree 1 $\alpha X(\varepsilon)=X(\varepsilon\alpha)$
- and temporal invariance.

They are composed of two parts, an autoregressive model usually abbreviated as AR(p) with p the order and a moving average one MA(q) of q order.

Autoregressive Model An autoregressive model of p order can be described as

$$X_t = c + \sum_{i=1}^{p} \varphi_i X_{t-i} + \varepsilon_t \tag{3.27}$$

where φ_i are the coefficients of the linear regression representing the dependency on the past occurrences of the vector X_t. In other words it is a lag operator introducing in the present time a fraction of the past values. The order p expresses the number of previous steps involved in the computation of the present time.

Moving average model The moving average part of the model

$$X_t = \mu + \varepsilon_t + \sum_{i=1}^{q} \theta_i \varepsilon_{t-i} \tag{3.28}$$

is always a linear regression but based on the previously assigned white noises ε_{t-i} rather then the actual occurrences as for the autoregressive one.
Physically it is equivalent to applying random impulses to a system an propagating their effects for a q number of steps.

ARMA model Finally the complete ARMA(p,q) is a combination of the two described parts resulting in

$$X_t = c + \varepsilon_t + \sum_{i=1}^{p} \varphi_i X_{t-i} + \sum_{i=1}^{q} \theta_i \varepsilon_{t-i} \tag{3.29}$$

Model estimation The main difficulty related to the use of the model described in the present section is the estimation of the coefficients. A good paper on the topic is [54]. In the current work the author did not focus on developing a specific estimator for the parameters of the ARMA model. The MATLAB's embedded ARMAX algorithm was utilised. One can refer to the MathWorks website [MathWorks] for any further detail on the strategy adopted.

Chapter 4

Proper Orthogonal Decomposition

4.1 Introduction

Proper orthogonal decomposition is a methodology aiming to construct an optimal basis in the functional analysis sense. Proper orthogonal decomposition is a well known technique in functional analysis and it consists in the search of an optimal base in which the description of a problem results simplified.
Here for basis it is intended a orthonormal system of functions in a domain Ω A very simple and explanatory example is the solution of a typical early university physics problem such as a mass m spring k concentrated elements model. One can write the equation of the motion $x(t)$ and its initial conditions as

$$\begin{cases} m\ddot{x} + kx = 0 \\ \ddot{x}_0 = 0 \\ x_0 = A \end{cases} \tag{4.1}$$

if rather than describing this problem in the normal space domain, we "change" coordinates applying the

$$x(t) = e^{(\alpha y)} \tag{4.2}$$

then the problem in (4.1) can be rewritten as

$$m\alpha^2 e^{(\alpha y)} + k e^{(\alpha y)} = 0 \tag{4.3}$$

then the (4.1) becomes equivalent to finding the root of a polynomial of the second order

$$m\alpha^2 + k = 0 \tag{4.4}$$

A purely algebraic relation now describes the motion of a mass and spring being in the real space a complex motion described by a differential equation. This very simple example shows that the choice of an appropriate reference space of functions containing some intrinsic information about a specific system, makes the solution of a physical problem simplified and meaningful.
In general given also a generic forcing $F(t)$ term on the right hand side of the (4.1), then applying the Fourier decomposition a differential problem becomes an algebraic sum of an infinite number of functions by a relative coefficient. In practical problems for numerical purposes the series is truncated at the point where the description is considered sufficiently accurate. The rate of convergence with the number of modes utilised is as a consequence a topic of particular interest.
The methodology is traditionally extended to the solutions of multidimensional physical and engineering problems such as heat transmission, diffusion, deflection of a plate, etc. [8],[68]. An identical procedure has been applied for decades to the solution of homogeneous turbulence via the so-called spectral solvers [53].
The equivalent of finding this meaningful optimal basis in a more general case of non uniform turbulence requires the use of POD [46] [31] [13] [12] also known as Karhunen-Loève expansion.
This methodology has been used fluid dynamics POD mainly:

- similarly to the Fourier decomposition for the development of a class of pseudo-spectral solvers [31, 41, 26]
- for the individuation of coherent structures in a flow [59] even though same author believe it is still an open problem
- for the generation of inflow conditions for turbulence resolved simulations [33, 24]

The author himself developed a novel inflow generator making use of this technique and implemented the existing one by Haepfner [33] extending it and providing some modifications according to the insides provided by section 4.2.1 on the use of symmetries.

4.1.1 POD definition

The treatment below follows mainly from Holmes book [31].
The mentioned proper orthogonal decomposition can be written as

$$u(x,t) = \sum_{i=1}^{N} a_i(t)\varphi_i(x) \tag{4.5}$$

Given a generic scalar product $(\cdot,\cdot)$ defining a Hilbert space where everything is sufficiently regular and square integrable (L^2). This consists in finding an optimal orthogonal basis

$$\{\varphi_i\}_{i=1}^{N} \subset L^2(\Omega) \tag{4.6}$$

that:

- respects the boundary conditions of the problem,
- presents the highest possible energy in the first modes hence

$$\max_{\varphi\in\Omega} = \frac{\langle|(u,\varphi)|\rangle}{\|\varphi\|^2} \tag{4.7}$$

The former condition is a requirement for the functions to be a basis for the problem to be resolved. The latter is mathematically translated as being the basis with the smallest possible mean square of the truncation error.

$$\min_{\varphi\in\Omega} = \langle\|u - \frac{(u,\varphi)}{\|\varphi\|^2}\varphi\|^2\rangle \tag{4.8}$$

From the above (4.7) a variational problem rises

$$J[\varphi] = \langle|(u,\varphi)|\rangle - \lambda\left(\|\varphi\|^2 - 1\right) \tag{4.9}$$

and the minimisation of the functional $J[\varphi]$ can be shown to consist in solving

$$(\langle(\varphi,u)\,u\rangle,\psi) - \lambda\,(\varphi,u) \tag{4.10}$$

where ψ is the variation and λ result an eigenvalue for the linear operator

$$R\varphi = \langle(\varphi,u)u\rangle \tag{4.11}$$

reducing the search for φ to the search of the eigenfunctions of the operator R.

4.2 Field POD

When defining the R operator from a velocity field $\mathrm{u}(\mathrm{x},t)$ defined in a space $\Omega \subset \mathbb{R}^3$ having the properties defined in the previous section, the scalar product between two vector fields u and v can be written according to the following functional definition

$$(\mathrm{u},\ \mathrm{v})_\Omega \ := \int_\Omega \mathrm{u}\cdot\mathrm{v}\,\mathrm{dx} \tag{4.12}$$

Both u and v are required to be L^2 (square integrable) in Ω.
Given the inner product the norm then results

$$\|\mathrm{u}\|_\Omega := \sqrt{(\mathrm{u},\mathrm{u})_\Omega} \tag{4.13}$$

The Hilbert-Schmidt theory (in a similar fashion to the Gram-Schmidt orthogonalisation) assures the diagonalisation of the averaged autocorrelation function

$$R(\mathrm{x},\ \mathrm{y}) = \overline{\mathrm{u}(\mathrm{x},t)\otimes\mathrm{u}(\mathrm{y},t)} \tag{4.14}$$

is always possible being R positive semidefinite. It can be written as the eigenvalue problem

$$\int_\Omega \mathrm{R}(\mathrm{x},\ \mathrm{y})\varphi_i(\mathrm{y})\,\mathrm{dy} = \lambda_i\varphi_i(\mathrm{x}) \tag{4.15}$$

The mentioned theory also assures real positive eigenvalues and ordered in decreasing order $\lambda_1 \geq \lambda_2 \geq \lambda_3 \geq \ldots > 0$.

By making use of the property of orthogonality

$$(\varphi_i,\ \varphi_j)_\Omega = \delta_{ij} \tag{4.16}$$

and given (4.5) and the scalar product definition one can write

$$\mathrm{u} = \sum_{i=1}^{N}(\mathrm{u},\varphi_i)\varphi_\mathrm{i} \tag{4.17}$$

This is the field reconstruction by use of the eigenfunctions φ_{i} multiplied by the coefficients $a_i = (\mathrm{u}, \varphi_i)$ given by the projection of the field on the mentioned eigenfunctions basis. If u is a function of both space x and time t it can be noticed that

$$a_i(t) = (\mathrm{u}(\mathrm{x},\ t),\ \phi_i(\mathrm{x}))_\Omega \tag{4.18}$$

The resulting coefficients are only time-dependent. This variables separation procedure is well known in literature for the solution of partial differential equations [8]. It has been used by the author to separate the space correlation from the time correlation in the developed inflow model. The expression for the autocorrelation function making use of the found eigenfunctions

$$\mathrm{R}(\mathrm{x},\ \mathrm{y})\ := \sum_{i=1}^{\infty} \lambda_i \varphi_i(\mathrm{x}) \otimes \varphi_i(\mathrm{y}) \tag{4.19}$$

can be specialised to write the Reynolds stresses tensor by applying $\mathrm{x} = \mathrm{y}$. It is then immediate to give to the eigevalues λ_i the meaning of turbulent kinetic energy associated to each mode φ_i over the entire domain Ω:

$$\mathrm{K}_\Omega = \frac{1}{2}\overline{(\mathrm{u}', \mathrm{u}')_\Omega} = \frac{1}{2}\sum_{i=1}^{\infty} \lambda_i \tag{4.20}$$

4.2.1 Homogeneity Directions

When a field is translation invariant hence its characteristics don't change with coordinates variations than it is true that its two point correlation tensor R respects $\mathrm{R}(x, x') = \mathrm{R}(x, -x')$. then it can be written as [8]

$$\mathrm{R}(x - x') = \sum c_k e^{2\pi i k (x - x')} \tag{4.21}$$

with c_k eigenvalues and $e^{2\pi i k (x-x')}$ Fourier basis. As a direct consequence

$$\mathrm{R}(x, -x') = \sum c_k e^{2\pi i k x} e^{-2\pi i k x'} \tag{4.22}$$

This property is particularly useful in multidimensional spaces. Specifically the author used it in order to simplify and increase the rate of convergence of the series of the λ_i in (4.20). For example in 2-d one could immediately remove one direction from the determination of the eigenfunctions if that direction is a direction of homogeneity. Let us consider x_1, then

$$\mathrm{R}(x_1, x_1', x_2, x_2') = \mathrm{R}(x_1 - x_1', x_2, x_2')$$

In the typical channel or local atmospheric flow the spanwise and crossstream directions could be considered of homogeneity leaving only the orthogonal-to-the-wall direction of non homogeneity. POD is in fact strictly the only way to represent synthetically non-homogeneous turbulence. Applying the Fourier system in a direction of non-homogeneity would consequently produce a homogeneous field conversely to what is erroneously stated by Huang et Al. [32]. In the case of the present work the author implemented in OpenFOAM POD analysis for 2d ad 3d domains having respectively 1 and 2 directions of homogeneity. When applying the above to x_1 and x_3, the Reynolds stresses result of the form $\mathrm{R}(x_1 - x_1', x_2, x_2', x_3 - x_3')$. Considering a rectangular box of bounds $[0,\ L_1] \times [0,\ L_3]$ one can obtain the following decomposition

$$\mathrm{u}(\mathrm{x},\ t) = \sum_{k_1} \sum_{k_3} \sum_{n} a_{k_1,k_3,n}(t) \mathrm{e}^{2\pi \mathrm{i}(\frac{k_1 x_1}{L_1} + \frac{k_3 x_3}{L_3})} \varphi_n(k_1, k_3, x_2)$$

with mixed space-wavevector eigenfunctions $\varphi_n(k_1, k_3; x_2)$. The same of the above specialised for a boundary patch such as an inlet one can be written as

$$\mathrm{u}(\mathrm{x},\ t) = \sum_{k_3} \sum_{n} a_{k_3,n}(t) \mathrm{e}^{2\pi \mathrm{i}(\frac{k_3 x_3}{L_3})} \varphi_n(k_1, x_2)$$

The space dependency is all contained in the eigenfunction while the coefficients $a_{k_3,n}(t)$ retain the time information and are still time cross-correlated.

The described decomposition is used in the state of the art tools for the description of wall-bounded turbulent flow [12] [31] and in the so-called spectral solvers [16] and specifically of the Navier-Stokes equations for turbulence [31]. Traditional spectral solvers only make use of the sole Fourier decomposition and resolve partial differential equations under the assumption of homogeneity. As described in the Holmes et al. book [31] it is possible to generalise the spectral methodologies by making use of the POD basis in place of the Fourier one. The original contribution of this work is using such decomposition for the prescription of the boundary conditions in a spatial resolved turbulence simulation.

4.2.2 Snapshots Method

The snapshot method introduced by Sirovich in [59]. is a numerical methodology for the computation of the POD from the knowledge of just a few instances of a field $\{\mathrm{u}^i\}_{i=1}^{M}$ (

space fields at a specific time) given that they are taken sufficiently far one from the other so that they can be assumed to be considered linearly independent. This is an assumption based on experience: an instantaneous turbulent field is assumed to be independent from another if a time longer than the slowest turbulence eddy in the flow. In general the linear independence is not guaranteed by any theoretical framework. In general the solution of (4.11) on a computational grid of the size N [59, 31] would result in a $N \times N$ a eigevalues problem.
Considering M realisations of the field of size N picked so that they are linearly independent, they naturally constitute a basis for the problem. The eigenvectors of the POD could then be written as

$$\varphi = \sum_{k=1}^{M} a_k \mathrm{u}^k \tag{4.23}$$

a linear combination of these $\{\mathrm{u}^i\}_{i=1}^{M}$ selected fields. The determination of the coefficients a_k is equivalent of finding the eigevectors of the original problem.
In fact by substituting (4.23) into (4.11) one can find

$$(\frac{1}{M}\sum_{i=1}^{M} \mathrm{u}^i(\mathrm{u}^{\mathrm{i}})^{\mathrm{T}}) \sum_{k=1}^{M} a_k \mathrm{u}^k = \lambda \sum_{k=1}^{M} a_k \mathrm{u}^k. \tag{4.24}$$

By association this can be rewritten as

$$\sum_{i=1}^{M}[\sum_{k=1}^{M} \frac{1}{M}(\mathrm{u}^k,\ \mathrm{u}^{\mathrm{i}}) a_k]\mathrm{u}^i = \lambda \sum_{k=1}^{M} a_k \mathrm{u}^k. \tag{4.25}$$

demonstrating that the search for the a_k

$$\sum_{k=1}^{M} \frac{1}{M}(\mathrm{u}^k,\ \mathrm{u}^i) a_k = \lambda a_i; i = 1, \ldots, M \tag{4.26}$$

would return the actual first M eigenfunctions $\{\varphi^i\}_{i=1}^{M}$. Summarising the problem by resolving the eigenvalues problem for a set of snapshots rather than the entire autocorrelation matrix reduces the computation in case of few selected $M << N$.

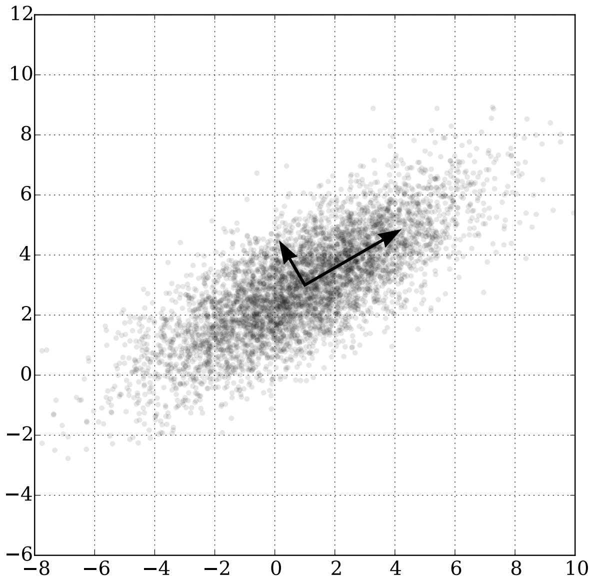

Fig. 4.1 Principal axis search for scattered points from Wikipedia

4.3 Principal components analysis

The principal components analysis is an orthogonal transformation technique applied to a data set in order to rearrange the vector components $x_1, x_2, ..x_N$ so that they are arranged with decreasing variances.
A second feature is that the final set of coordinates is ideally much smaller or at most the same size as the starting system $M \leq N$. The first assertion is very similar to finding the principal axis of rotation of a rigid body. A visual explanation of the found principal axis for a 2d case can be found in figure 4.1. It can also be seen as the discrete equivalent of POD.
From a computing point of view the author implemented a PCA over the grid data rather than analytically computing the field which is in practice impossible due to the binary nature of computers.
For the practical computation of the POD modes a $N \times M$ matrix like the following

$$\mathrm{X} = [\mathrm{u}^1 \ \ldots \ \mathrm{u}^M] \tag{4.27}$$

where u^k are M snapshots have been generated. The problem in (4.11) specialised for the system of N data results in a $N \times N$ matrix

$$\frac{1}{M}\mathrm{XX}^T \varphi = \lambda \varphi \tag{4.28}$$

with

$$\varphi = Xa \tag{4.29}$$

eigenvectors of the vectors of the problem $a = (a1, \dots, a_M)$. The problem is reduced to a M-dimesioned one by the snapshots method and by taking only a M subset of the original N data

$$\frac{1}{M}\mathrm{X}^\mathrm{T}\mathrm{Xa} = \lambda \mathrm{a}$$

PCA is defined as

$$\mathrm{X} = \mathrm{U}\Sigma\mathrm{V}^\mathrm{T} = \sum_{j=1}^{r} \sigma_j \varphi_j \mathrm{v}_j^\mathrm{T} \tag{4.30}$$

where

- the matrix X is $N \times M$ according the definition given at the beginning of the current section
- $\mathrm{U} = [\varphi_1 \, \dots \, \varphi_N]$ and $\mathrm{V} = [\mathrm{v}_1 \, \dots \, \mathrm{v}_M]$ respect the condition of orthonormality $\mathrm{U}^\mathrm{T}\mathrm{U} = \mathrm{I}_{N\times N}$ and $\mathrm{V}^\mathrm{T}\mathrm{V} = \mathrm{I}_{M\times M})$
- and finally

  $$\Sigma = \begin{bmatrix} \Sigma_1 \\ 0 \end{bmatrix}, \; N \geq M, \; \Sigma = [\Sigma_1 \; 0], \; N \leq M \tag{4.31}$$

  with Σ_1 the diagonal matrix of the eigenvalues σ_j of the problem disposed according to their magnitude from the largest to the smallest.

Replacing this definition (4.30) into the snapshots problem (4.28), one can find that

$$\frac{1}{M}\mathrm{XX}^T \varphi_\mathrm{i} = \frac{1}{M}\sum_{j=1}^{r}\sum_{k=1}^{r} \sigma_j \sigma_k \varphi_j \mathrm{v}_j^\mathrm{T} \mathrm{v}_k \varphi_k^\mathrm{T} \varphi_i = \frac{1}{M}\sigma_i^2 \varphi_\mathrm{i} \tag{4.32}$$

This is because of the orthogonality of the v_k and φ_k. By comparison of (4.32) and (4.28) it is of immediate individuation that $\lambda_{\mathrm{i}} = \sigma_i^2/M$.
The numerical equivalence of the two method came evident to the author during the development of the tools used in this thesis work.

Chapter 5

Synthetic Inflow Generation

This chapter presents the current state of art of turbulent inflow generation techniques recently developed for turbulence resolved simulations such as LES and DNS. The models performance is evaluated in terms of ability to satisfy the continuity equation and simultaneously reproduce the desired flow statistics. The methods described are the Smirnov's random flow generation, the Huang's remapping and realigning algorithm, the Yu's vector potential method, the vortons method, the Benovitz's spectral representation and coherence functions and the Haepffner's POD coefficient reconstruction via ARMA.

5.1 Introduction

Conceptually, the most straightforward way to solve the inflow problem is to generate realistic data via a precursor simulation. This method requires to obtain spatially developed solutions, typically, using periodic or rescaling boundaries and feed time varying values from a given plane into a target simulation. The main disadvantage of this approach is the associated computational cost. Examples of such simulations can be found in [47, 42, 36]. Also only statistically steady state flow fields can be reproduced.

One early approach for generating synthetic turbulence was proposed by Kraichnan in [40] who developed a method for constructing a random divergence-free velocity field for a homogeneous turbulence from a predefined energy spectrum. Only delta of Dirac and Gaussian spectra were reproducible. A family of method was subsequently developed based on that approach. In [60] an a homogeneous field is generated by selecting wave-vectors from a single Gaussian spectrum and the extension to inhomogeneous field is performed by scaling and rotation based on Reynolds stresses. A realigning and remapping technique of wave-vectors was developed [32] and subsequently extended in [17]. Both articles use spectra

of inhomogeneous turbulence. In [75] the authors describe a violation of mass continuity conditions and develop a method combining Kraichnan approach and stream formulation. All of these approaches can serve as both inlet conditions and flow field generation method. An interesting methodology was also presented by [11] for the assessment of bridges dynamic forcing due to wind. This is somehow similar to the above mentioned but presents an approach coming from the Shinozuka's [57] described in Chapter 3 where the spectra $S(\kappa_1, \kappa_2)$ is made explicit as $S(\kappa, \omega)$ making use of a coherence function.
Another comparative study has been carried in [37] and more recently in [65]. They describe a class of methodologies consisting in the production of a white noise successively treated in order to produce turbulence. From those works one can say the production of such turbulence is short living in the downstream-the-inlet domain region. For this reason they are not treated in the dissertation that follows.
Furthermore only recently in [33] an innovative technique making use of

- the intrinsic flow structures represented by the POD modes and relative
- coefficient via an auto-regressive moving average model

has been introduced. This makes use of random generation techniques but being connected to the POD structures returns an accurate description of the original flow.
In the following section the mentioned methodologies are described more in detail.
The author of this work implemented them in OpenFOAM succeeding in utilising the Smirnov and the Haepffner ones. The Vortons model is already available in the LEMOS library [LEM] for OpenFOAM.

5.2 Spectral Methods

5.2.1 Smirnov's method

In [60] a random flow generation (RFG) technique is proposed. Using inverse Fourier transform and a predefined Gaussian spectrum it constructs the homogeneous velocity field and then performs a transformation based on local information of Reynolds stresses. The procedure is summarised below briefly:

1. Given the anisotropic Reynolds stress tensor R_{ij} find an orthogonal transformation that diagonalises R_{ij}:

$$a_{mi}a_{nj}r_{ij} = \delta_{mn}c_n^2 \tag{5.1}$$

$$a_{ij}a_{kj} = \delta_{ij} \tag{5.2}$$

2. Construct the homogeneous field $\mathbf{v} = (v_1, v_2, v_3)$ by:

$$\mathbf{v}(\mathbf{x},t) = \sqrt{\frac{2}{N}} \sum_{n=1}^{N} \left[\mathbf{p}^n \hat{x}_j + \omega_n \hat{t}) + q^n \hat{x}_j + \omega_n \hat{t})\right] \tag{5.3}$$

$$\hat{x}_i = \frac{x_i}{l}, \quad \hat{t} = \frac{t}{\tau}, \quad c = \frac{l}{\tau}, \quad \hat{k}_i^n = k_i^n \frac{c}{c_i} \tag{5.4}$$

$$p_i^n = \varepsilon_{ijm} \zeta_j^n k_m^n, \quad q_i^n = \varepsilon_{ijm} \xi_j^n k_m^n \tag{5.5}$$

$$\zeta_j^n, \xi_j^n, \omega_n \sim \mathcal{N}(0,1), \quad k_i^n \sim \mathcal{N}(0,1/2), \tag{5.6}$$

where the repeated indices imply summation, l and τ are predefined length and time scales, respectively. $\mathcal{N}(\mu, \sigma^2)$ is the normal distribution with mean μ and standard deviation σ. The choice of k_i^n leads to the following energy spectrum of the homogeneous field:

$$E(k) = 16\sqrt{\frac{2}{\pi}} k^4 \exp(-2k^2). \tag{5.7}$$

3. Apply the scaling and rotation from 1) to the homogeneous field

$$w_i = c_i v_i \tag{5.8}$$

$$u_i = a_{ik} v_k \tag{5.9}$$

Equations 5.5 enforce orthogonality between wavevectors and Fourier transformed velocity $\mathbf{p}^n$ and $\mathbf{q}^n$ causing the resulting velocity field $\mathbf{v}$ to be divergence free. The scaling and rotation in point 3 may not preserve that property and therefore it is assumed that c_i are slowly varying functions of position causing the field $\mathbf{u}$ to be nearly divergence free. Note also, that length and time scales are single parameters and the only spatial variation is introduced through c_i. The authors suggest to obtain those values from a precursors RANS simulation.

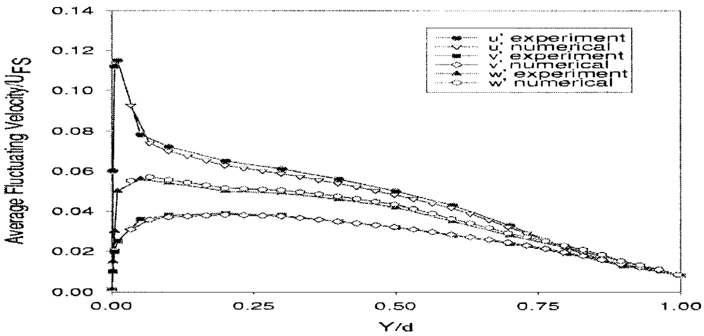

(a) Reynolds Stresses for boundary layer flow-field compared with LES data Speziale [63]

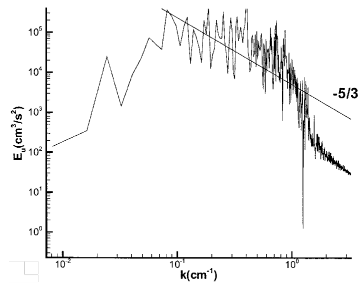

(b) Turbulence spectrum generated

Fig. 5.1 Pictures from Smirnov paper [60]

In Figure5.1a one can see reported the Reynolds Stresses and the turbulence spectrum from the Smirnov paper. The data shown is a comparison between the experimental data used as input and the flow field generated by this method when truncating the series in equation (5.3) to the harmonic $N = 1000$. One can see from Figure5.1a that the method reproduces accurately the Reynolds stresses of the target experiment. Given the Gaussian nature of the coefficients in (5.5) the turbulence spectrum generated is that of the equation (5.7) and does not strictly obey to the $-5/3$ turbulence spectrum law [53]. In Figure5.1b the spectrum generated by the method is shown. The shape is in accordance with the above consideration.

5.2.2 Huang's method

Huang in [32] introduces novel features to Smirnov method that allow to reproduce any anisotropic energy spectrum. The velocity is now decomposed as:

$$\mathbf{u}(\mathbf{x},t) = \sum_{m=k_0}^{k_{\max}} \mathbf{u}_m(\mathbf{x},t) = \sum_{m=k_0}^{k_{\max}} \sum_{n=1}^{N} \mathbf{p}^{m,n} \cos(\tilde{\mathbf{k}}^{m,n} \cdot \mathbf{x} + \omega_{m,n} t) \\ + \mathbf{q}^{m,n} \sin(\tilde{\mathbf{k}}^{m,n} \cdot \mathbf{x} + \omega_{m,n} t). \tag{5.10}$$

The Fourier transform coefficients contain two upper indices m, and n with the first one denoting the wave-vector length and their index within one group. The actual Fourier

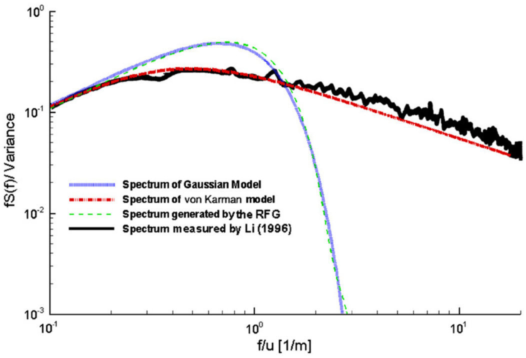

(a) Turbulence spectrum generated by the Smirnov method (RFG) vs wall bounded turbulence according to Li [43]

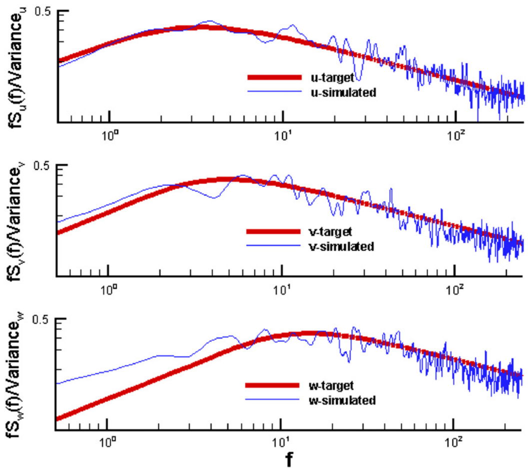

(b) Turbulence spectrum generated by the Huang method (RFG) vs reference von Karman model

Fig. 5.2 Turbulence spectra from Huang et al. paper [32]

coefficients are obtained by aligning and remapping:

$$p_i^{m,n} = \text{sign}(r_i^{m,n})\sqrt{\frac{4}{N}E_i(k_m)\frac{(r_i^{m,n})^2}{1+(r_i^{m,n})^2}}, \tag{5.11}$$

$$q_i^{m,n} = \text{sign}(r_i^{m,n})\sqrt{\frac{4}{N}E_i(k_m)\frac{1}{1+(r_i^{m,n})^2}}, \tag{5.12}$$

where $r_i^{m,n}$ are independent, identically distributed random variables with zero mean and standard deviation of 1.

In Figure5.2 one can see the claimed improvement point on the Smirnov method of the one presented in this section. Turbulence in general present a peculiar spectral shape depending on the generating and decaying conditions and does not correspond to the Gaussian model reproduced by the Smirnov method (Figure 5.2a). For example wall bounded pressure driven flows are well described by the von Karman model [43, 53]. Huang et al. assert their method can reproduce a generic spectral shape and they show how it can be used to recreate the von Karman spectra in Figure 5.2b.

5.2.3 Yu's method

Yu and Bai in their recent paper [75] introduce an alternative way of producing a divergent-free velocity field by means of taking the curl of a synthesized complex vector potential Φ

$$\mathbf{w}(\mathbf{x}) = \nabla \times \Phi(\mathbf{x}). \tag{5.13}$$

$\mathbf{w}$ are the velocity components in the reference frame of the orthogonalised Reynolds' stresses. The produced velocities undergo a rotation procedure $u_i(\mathbf{x}) = a_{ij}(\mathbf{x})w_j(\mathbf{x})$ like (5.9) which preserves continuity as demonstrated by [60]. The scaling operation in (5.8) is applied to the vector potential rather than used to re-proportion the velocity fluctuation at the end of the generation procedure as for the methods in sections 5.2.1 and 5.2.2. By doing so the derived velocities respect continuity.
The generic vector potential $\Phi(\mathbf{x})$ is obtained from a homogeneous vector potential $\Psi(\mathbf{y})$ by multiplication times a scaling function $\mathbf{f}(\mathbf{x})$

$$\Phi_i(\mathbf{x}) = \Psi_i(\mathbf{y}(\mathbf{x}))f_i(\mathbf{x}), i = 1,2,3 \tag{5.14}$$

where $\mathbf{y}$ are the coordinates in a fictitious auxiliary domain on which Ψ is computed.

If the coordinate transform is described by

$$y_i(x_i) = \int_{x'=0}^{x_i} \frac{1}{\bar{c}_i(x_i')} dx_i' \tag{5.15}$$

where $\bar{c}_i(x_i')$ is a function of its own coordinate only, one can write the transformation function as

$$f_i(\mathbf{x}) = \frac{\bar{c}_1\bar{c}_3\bar{c}_3}{\bar{c}_i}\sqrt{\left(\frac{c_1^2}{\bar{c}_1^2} + \frac{c_2^2}{\bar{c}_2^2} + \frac{c_3^2}{\bar{c}_3^2}\right) - 2\frac{c_i^2}{\bar{c}_i^2}} \tag{5.16}$$

Here the c_i have the same meaning as in (5.8) and they provide the required scaling on the velocity fluctuations. Ψ is generated similarly to the velocities in the methodologies described in sections 5.2.1 and 5.2.2 but making use of the complex Fourier series

$$\Psi(\mathbf{y},t) = \sum_{n=1}^{N_T} \left[\hat{\Psi}(\mathbf{k}^n) \exp\imath(\mathbf{k}^n \cdot \mathbf{y} + \omega^n t) + \hat{\Psi}^*(\mathbf{k}^n) \exp -\imath(\mathbf{k}^n \cdot \mathbf{y} + \omega^n t)\right]. \tag{5.17}$$

The complex coefficients result

$$\hat{\Psi} = (D_1^Y D_2^Y D_3^Y)^{-1/2} \sqrt{\frac{E(k/2\pi)}{2\pi(k/2\pi)}} \frac{\mathbf{z}^n}{\mathbf{z}^n \times \mathbf{k}^n} \tag{5.18}$$

where

D_i^Y are the $\mathbf{y}$ domain sizes;

k_i^n are the wave vectors components selected according to $k_i^n = 2\pi m i_i / D_i^Y$ with $m_i \in [0, N_i/2] \wedge m_1 > 0 \cup m_1 = 0 \cap (m_2 > 0 \cup (m_2 = 0 \cap m_3 > 0))$ and N_i number of domain cells in each direction;

$E(k/2\pi)$ is the desired turbulence spectrum;

$\mathbf{z}^n$ is a random vector.

The real and imaginary parts of the latter are constructed according to the following

$$(\Re, \Im)(\mathbf{z})/\mathfrak{m}_{\Re,\Im} = \cos \varphi_{\Re,\Im} \frac{\cos \vartheta_{\Re,\Im} \cdot (\mathbf{n} \times \mathbf{k})/|\mathbf{n} \times \mathbf{k}| + \sin \vartheta_{\Re,\Im} \cdot \mathbf{n}/|\mathbf{n}|}{|\cos \vartheta_{\Re,\Im} \cdot (\mathbf{n} \times \mathbf{k})/|\mathbf{n} \times \mathbf{k}| + \sin \vartheta_{\Re,\Im} \cdot \mathbf{n}/|\mathbf{n}||} \tag{5.19}$$

(5.20)

with

$\mathbf{n}$ arbitrarily chosen real vector perpendicular to $\mathbf{k}$,

$\varphi_{\Re} \wedge \varphi_{\Im} \in [-\varphi^R, \varphi^R]$ with $0 \leq \varphi^R < \pi/2$,

$\mathfrak{m}_{\Re} \wedge \mathfrak{m}_{\Im} \in (0, 1]$,

$\vartheta_{\Re} \wedge \vartheta_{\Im} \in [-\pi, \pi]$.

Yu and Bai suggest the following choice for the spectrum

$$E(k) = 10\sqrt{2/\pi} u_{rms} k^4 L^5 \exp(-2k^2 L^2) \tag{5.21}$$

valid for shear flows with u_{rms} root mean square of the velocity fluctuations and L reference integral length scale.

In Figure5.3 velocity fluctuations magnitude of one instantaneous field and Reynolds stresses for a channel flow are reported. Figure5.3b shows the methodology is capable of generating a 3D field obeying to a assigned spacial shape of Reynolds stresses curves while remaining divergence-free according to the Authors' claims.

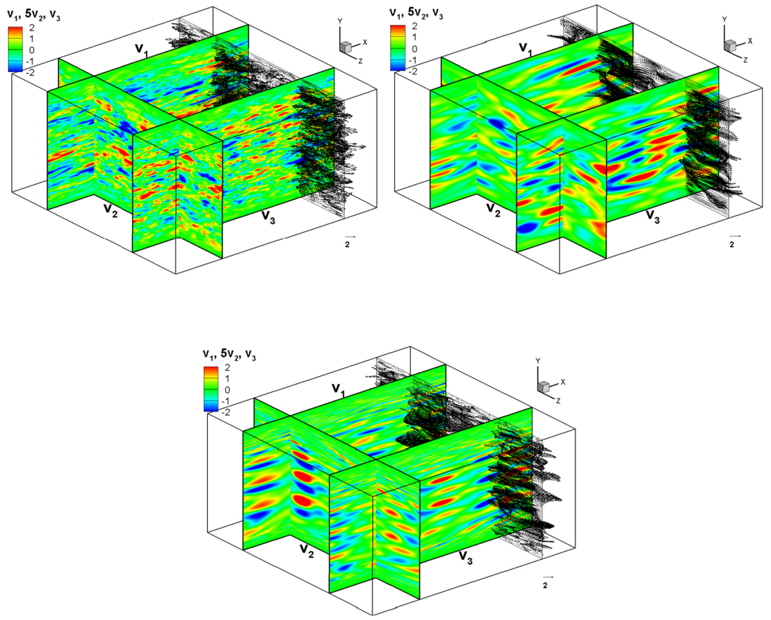

(a) Velocity fluctuations magnitude of one instantaneous field. Bottom picture: Smirnov method. Top Right: Yu and Bai method in production of Gaussian Spectrum. Top Left: Yu and Bai method in production of spectrum in (5.21)

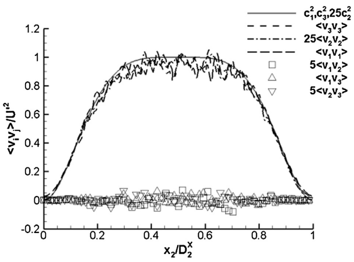

(b) Reynolds stresses produced vs target

Fig. 5.3 Reproduction of channel flow from Yu and Bai paper [75]

5.3 Vortex Methods

5.3.1 Vortons method

The method developed in Rostock University [39] and implemented in the freely available LEMOS library [LEM] consists in the superposition of a number of local, compact velocity fields called Turbulent Spots. Each turbulent structure has a velocity field described by

$$u_{si} = \frac{\pi^{3/2}\sqrt{2+\dfrac{\pi}{L^2}}}{2L^2}\exp\left(-\frac{1}{4}\left[2+\frac{\pi}{L^2}x^2\right]\right), i=1,2,3 \tag{5.22}$$

with L length scale. The velocity field so defined, describes a point-core vortex respecting the energy spectrum

$$E(k) = k^4\exp(k^2/k_0^2) \tag{5.23}$$

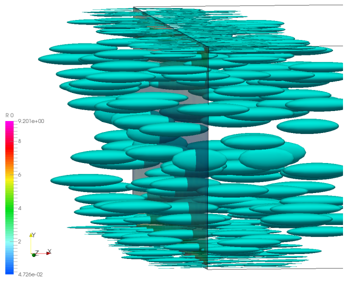

(a) Spacial representation of vortices convected through the inlet of a computational domain

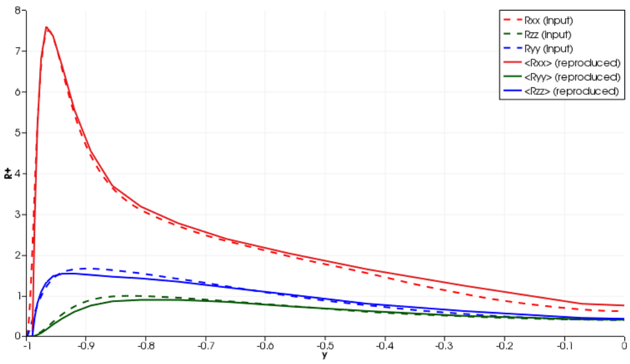

(b) Reynolds stresses produced vs target

Fig. 5.4 Reproduction of channel flow making use of the Vortons method [39]

of decaying turbulence. The velocity fluctuations field is reconstructed as a sum of structures $\mathbf{u_s}$ depending on a random position $\mathbf{x_s}$ and multiplied by ad random number ε_s

$$\mathbf{u}(\mathbf{x}) = \sum_{s=1}^{N} \varepsilon_s \mathbf{u}_s(\mathbf{x} - \mathbf{x}_s) \tag{5.24}$$

. The generated velocities are homogeneous and isotropic, have zero mean and present unitary amplitude. In order to match a prescribed Reynolds stresses field the transform described in [47] is applied to the fluctuations and the mean velocity profile summed according to

$$\mathbf{U} = \langle \mathbf{U} \rangle + A\mathbf{u} \tag{5.25}$$

where

$$A = \begin{pmatrix} 3\sqrt{R_{11}} & 0 & 0 \\ R_{21}/A_{11} & \sqrt{R_{22} - A_{21}{}^2} & 0 \\ R_{31}/A_{11} & (R_{32} - A_{21}A_{31})/A_{22} & \sqrt{R_{33} - A_{31}{}^2 - A_{32}{}^2} \end{pmatrix} \tag{5.26}$$

with R_{ij} local Reynolds Stresses. The dependency on $\mathbf{x}$ has been omitted for clarity.

The main limitations of the method are the possibility of reproducing only isotropic length scales L, the generation of generally divergent fields and the limited fixed turbulence spectra reproducible. In fact even though the $\mathbf{u}_s$ are divergence-free, the transformation in (5.25) does not preserve the property. Also in the LEMOS implementation the spectral shape in (5.23) is produced. This is rigorously correct only when specifying scales of turbulence smaller than the Taylor's hence not generally true for shear flows. In Figure5.4 one can see how also this method is capable of generating the prescribed Reynolds stresses of a channel flow.

5.4 POD Methods

In the past decades a number of researchers introduced the Karunen-Loeve decomposition in the statistical study of turbulent flows.
A fundamental breakthrough has been the snapshots technique introduced by Sirovic [59] presented in section 4.2.2. This allows obtaining the POD decomposition from a limited number of uncorrelated fields, making it particularly appealing in the study of PIV data.
In s recent publication Adrian et al. [45] presented a study providing a possible interpretation to the POD functions as turbulent coherent structures. They individuate the notorious hairpin vortices discovered in low-Reynolds number turbulent wall flows in a combination of POD modes. This is still an open discussion [33] and it is likely to continue in the next years.
One of the main applications is the extension of homogeneous turbulence *spectral solvers* to more general cases of inhomogeneous turbulence. Spectral solvers typically make use of the Fourier decomposition in order to transform the Navier-Stokes partial differential equations into a set of interconnected ordinary differential equations, resulting much simpler and efficient to solve turbulence [31], [53]. Such solvers can only be utilised in the case of homogeneous turbulence for the nature of the Fourier system [8]. Though when replacing the algebraic functional substructure of harmonics with an appropriate basis it is still possible to obtain a set of ODE but representing non-homogeneous turbulence.
Finally also inflow methodologies where introduced. Initially a more signal-like method was the generation of signals at each inlet boundary face centre.Each signal was time and space cross correlated. This methodology is not of simple use due to the large number of signals that require to be generated as the mesh size increases.
Druault et al. [24] show the idea of a mixed technique making use of POD for the reproduction of large scales and Fourier decomposition for the small ones in order to reduce the numerical complexities and produce an inflow starting from a limited number of experimental probes. They failed though to reproduce a full experiment and their paper is limited to the methodology explanation and showing only very simple 2D test cases from simulation data.
Finally Haepfner et al. [33] introduced the idea of decoupling space and time correlation. This is done by a technique somehow similar to the POD solvers: POD projection is used to take care of the spacial correlation and the resulting coefficients only require to be time auto

and cross correlated.
More detail is provided in the following section.

5.4.1 Haepffner method

Haepffner et Al. [33] provided an effective methodology for the production of statistically coherent fields.
Recalling equation (4.5)

$$\mathrm{u}(\mathrm{x},t)=\sum_{i=1}^{N}a_i(t)\varphi_{\mathrm{i}}(\mathrm{x})$$

one can say that by decomposing according to the POD technique the eigenfunctions $\varphi_{\mathrm{i}}(\mathrm{x})$ contain the whole space correlation information, and the time evolution is left to a set of time auto and cross correlated coefficients $a_i(t)$. Haepffner suggests the use of an ARMA model such as that in 3.29 for the continuous production of the coefficients $a_i(t)$. This is proven to be very effective in the generation of non-homogeneous inflows. In fact the generalisation from a Fourier basis such as that used in the spectral methods to a POD basis let the turbulence flow naturally non homogeneous, not requiring expedients such as stretching and rotating the components of the turbulent fluctuations produced. Also Haepffner shows the importance of the time correlation of the $a_i(t)$ coefficients by progressively activating features of the ARMA model in reproducing a reference 2d simulation with convected vortices (figure 5.5a)

- POD modes associated with Gaussian random coefficients in 5.5b
- time autocorrelation only but not cross correlation in 5.5c
- full correlation in 5.5d

In Figure5.6 the Reynolds stresses for the simulations in Figure5.5 are shown. One can see from Figure5.6b how the method generates a match for the reference simulation while when deactivating cross-correlation between the coefficients or both time and cross-correlation the space downstream required for the curves to match the reference increase. This is also confirmed by the stresses plotted on the centreline shown in Figure5.6a. It can also be noted how even for the full correlation case the instantaneous flow in 5.5d qualitatively differs from 5.5a while being able to develop very similar vortex patterns close to the inlet section.

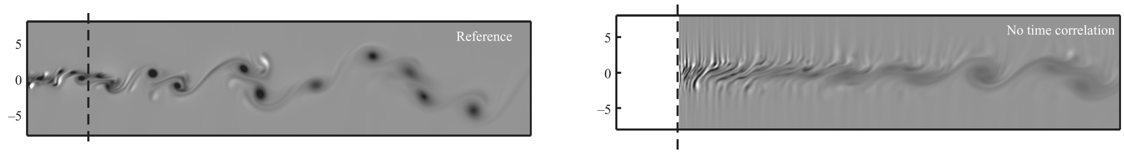

(a) Reference simulation

(b) No time correlation

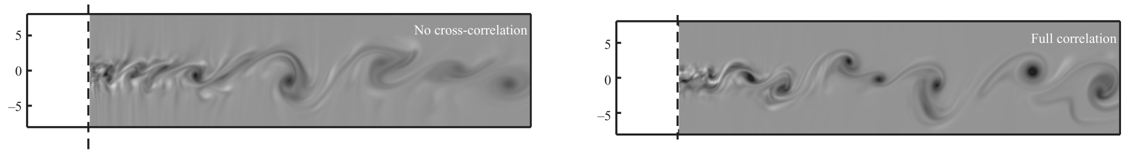

(c) No time coefficients cross-correlation

(d) Full correlation

Fig. 5.5 From Haepffner paper [33] synthetic flow reproduction via use of POD basis for space correlation

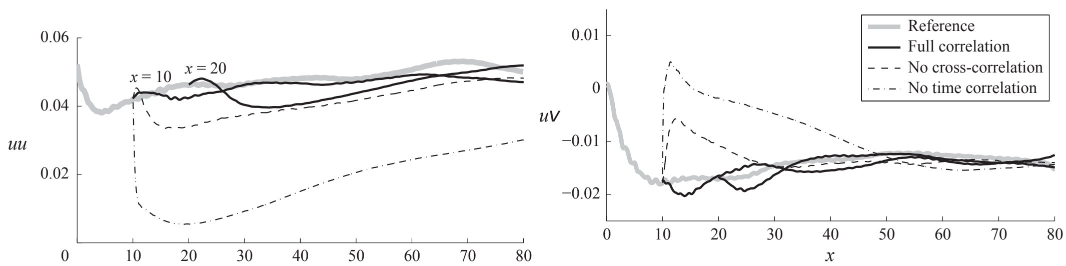

(a) Reynolds stresses on centreline

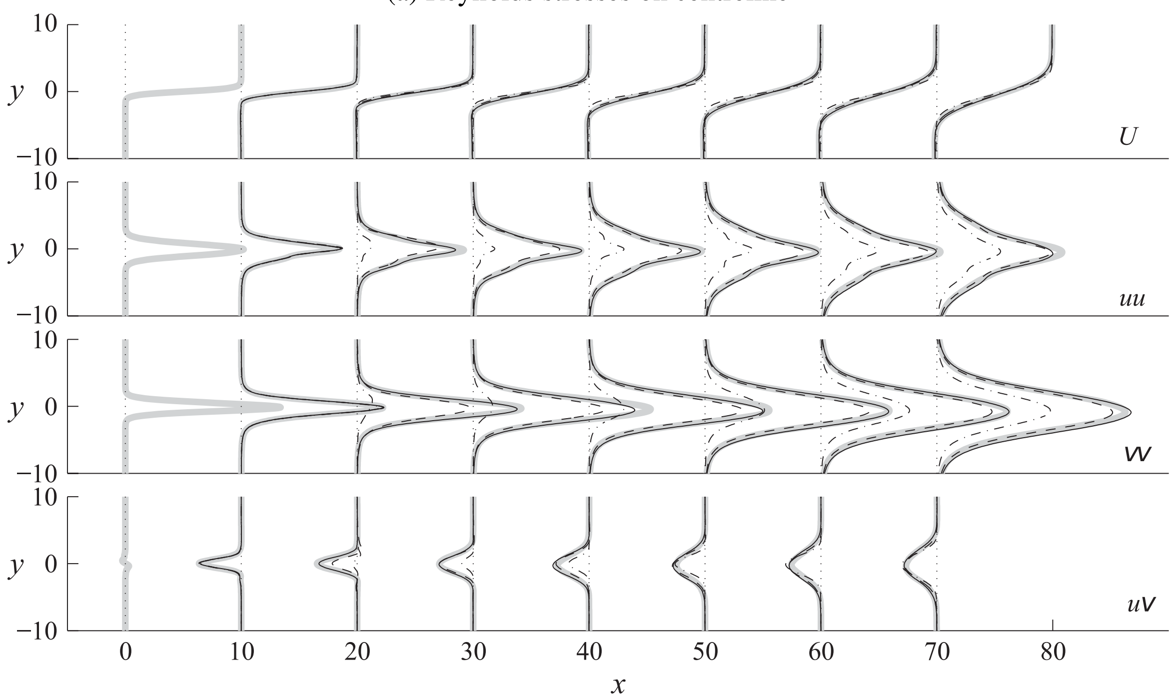

(b) Cross-wise Reynolds stresses at different downstream locations

Fig. 5.6 Reynolds stresses of convected vortices in a 2D domain making use of the Haepffner et al. method [33]. x distance downstream the inlet, y cross-wise direction

	Method					
Feature	Random	Smirnov	Huang	Yu	Vortons	Haepffner
Spatial Correlation	no	yes	yes	yes	yes	yes
Time Correlation	only through under-relaxation	yes	yes	yes	yes	yes
Reynolds Stresses	intensity only	yes	yes	yes	yes	yes
Spectrum	white noise	Gaussian	yes	yes	decaying turbulence	yes
Divergence-free flow	no	homog. only	yes	yes	homog. only	yes
Flow Structures	no	homog.	homog.	homog.	homog.	yes
Required Info	statistics only					flow history

Table 5.1 Summary table of Inflow Methods

5.5 Conclusions

In this chapter the author presented the state of the art of inflow generators for turbulence-resolved simulations such as LES and DNS. In Table5.1 a summary of the capability of each method is shown alongside a more classical turbulence random field generator. The random field generator produces uncorrelated white noise that is scaled according to the turbulence intensity required and under-relaxed in time in order to maintain a defined degree of time correlation. In other words each time step is blended to the previous according to a certain percentage.

One can notice how the rightermost method is the definite answer to the need of accurate boundary conditions. The main drawback is that it required a previous space and time knowledge of the flow in order to be able to reproduce it. On the other hand all the other methods are only capable of producing the flow structures of homogeneous and isotropic turbulence, that then get transformed to fit the statistics required. It should be noted how the divergence-free condition is required only for the generation of an entire field. In fact when limited to the generation of a sole bi-dimensional boundary of a domain, the flow generated is used as a boundary condition for (A.5) while the irrotationality is assured by the pressure correction equation (A.7).

Given its potentiality the author will present in this study a generalisation of the Haepffner method to 3D and to flows with a direction of homogeneity such as channel or boundary layer flows.

Part III

Methodologies

Chapter 6

Experimental Campaign Description

6.1 Introduction

Alongside the numerical work the author participated to an experimental water tank campaign within the framework of a SUPERGEN marine project in partnership with Cambridge university.

The author was in charge of developing a control strategy technique able to mitigate the effects of unsteady loads due to turbulence possibly effecting the fatigue life of hydrokinetic tidal turbines.

The work was seen as an opportunity to acquire data for the validation of the numerical methods under development. The original idea was to reproduce the experiment in a virtual environment and to validate the dynamic reaction of the model to different levels of turbulence and control strategies.

Unfortunately the author was only able to use the acquired data for the:

- tuning of the turbine aerofoil data to be inputed in the actuator line model (Chapter9).
- The dynamic validation of correspondence between upstream turbulence and thrust and torque signature at the shaft has to be left to further studies.

In the following section a description of the experimental setup used for the water tank campaign is described.

6.2 Test Rig Description

The author designed from scratch and constructed a system comprising the following assemblies:

- Acquisition system and motor drive cabinet
- Instrumented nacelle and turbine holding structures
- 2 Acoustic Doppler Velocimeters (ADV) and relative 2-axis positioning table
- NREL-Phase VI 1:10 scaled turbine model [28]

to be used in the recirculating water tank in the French town of Boulogne-Sur-Mer owned by the IFREMER research institute. A Labview program was also developed in order to provide control over the test rig turbine and ADCP position and at the same time acquire and store data from the deployed sensors.

The acquisition system is composed of:

- National Instruments PXI cabinet controlled by a Laptop via a PCIexpress-to-PXI bridge
- A NI PXI-6289 M Series DAQ (32 Analog Inputs, 4 Analog Outputs) acquisition and control card capable of non-simultaneous analogue inputs and outputs
- A NI-4472B 24-bit real-time simultaneous acquisition card

The motor drive was provided by Bosch and it is capable of both constant speed and constant torque control. Furthermore a resistor bank is placed alongside the controller in order to dissipate the energy generated by the turbine. In order to reduce the inertias of the control system a direct connection between the motor and the turbine has been implemented. An over-dimensioned motor in terms of power has been used to match the expected torque requirements from the turbine. From the below illustration one can see the instrumented nacelle layout. A torque sensor is attached via bevel couplings to the motor on one side and to the turbine-shaft assembly on the other.

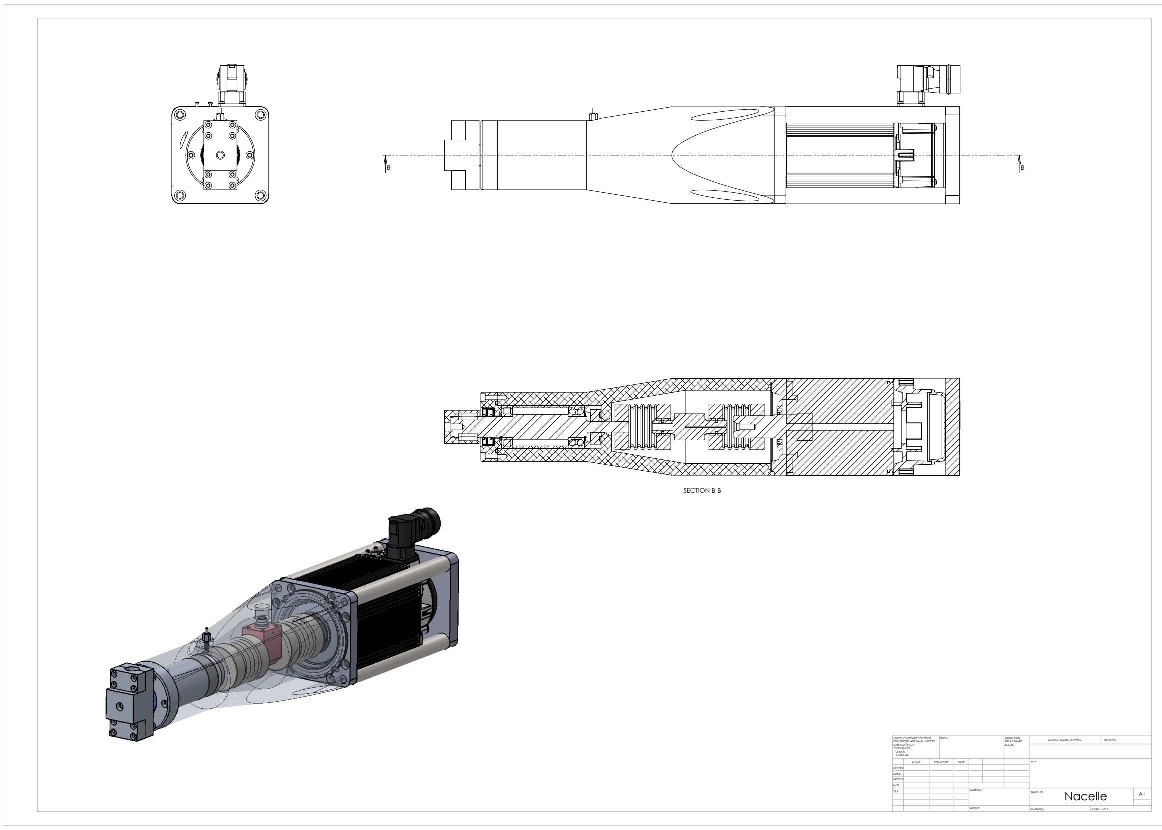

Fig. 6.1 Assembly of turbine nacelle

The shaft thrust measurement is provided by a ring load cell designed for bolts tension and here readapted.

Shaft size is locally reduced accordingly to have a free rotating and translating fit in the orifice.

Additionally an ADV was positioned 1 meter upstream the turbine and a second one free to move in a 1m downstream x 0.5m crosswise area thanks to a 2-axis positioning table. This was intended for turbulence spatial correlation measurements, unfortunately due to the poor seeding of the water in the tank the author could never get a sufficiently clean signal to do so.

The positioning of the movable ADV was controlled by the national instruments cards outputting an analogue voltage signal to two Arduino Uno prototyping cards with motor controller shield. The shields were connected to two stepper motors controlling one axis movement each.

The ADV were instructed to provide instantaneous velocity analogue signals via the proprietary Nortek Software interface and they were acquired by the above mentioned acquisition card.

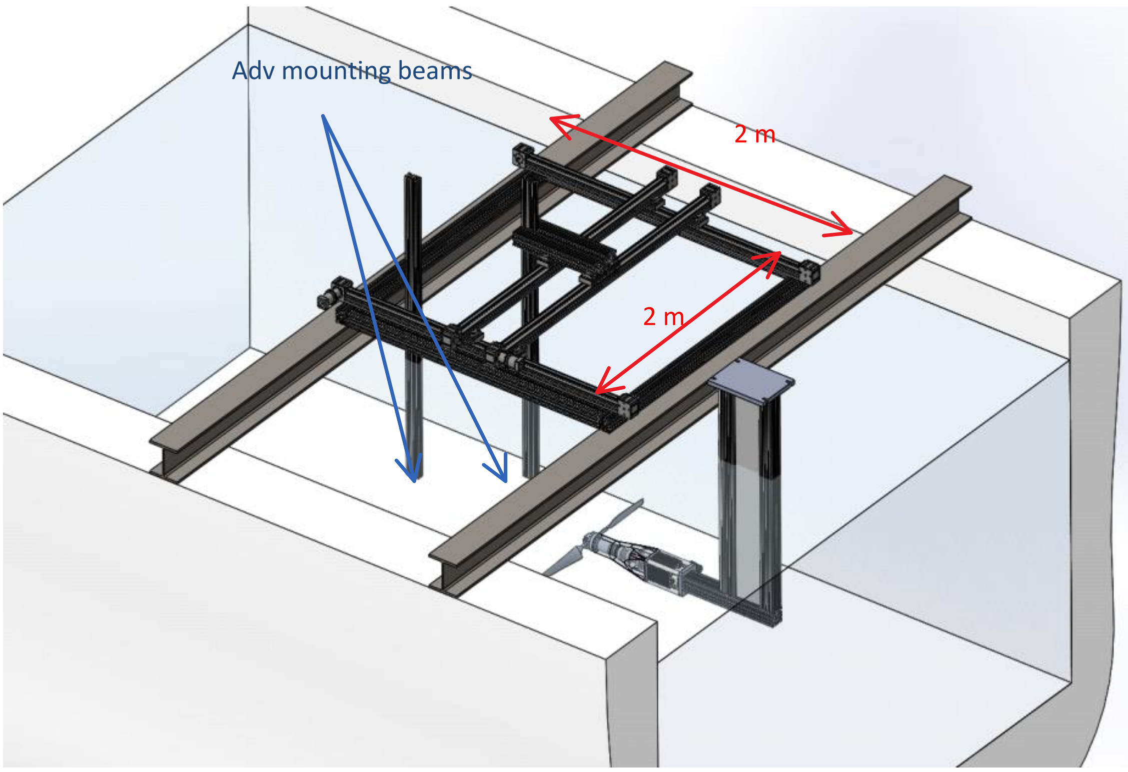

Fig. 6.2 Test Rig Rendering

The acquisition rate was set to 5kHz for all the instruments included those not providing fast response due to hardware and software limitations. Finally the utilised turbine rotor is a 1:10 scaled rotor geometrically congruent with the 10m one used in the NREL-Phase VI experiment described in [28]. It was picked up mainly for the experimental data already available and the large interest demonstrated by the academic community. In picture 6.4 the peculiarity of the cut of $0.3mm$ at the trailing edge is shown. The blades have been manufactured in aluminum via 6-axis CNC machining and hand polished. In picture 6.3 one can find a CAD rendering of the turbine-nacelle assembly.

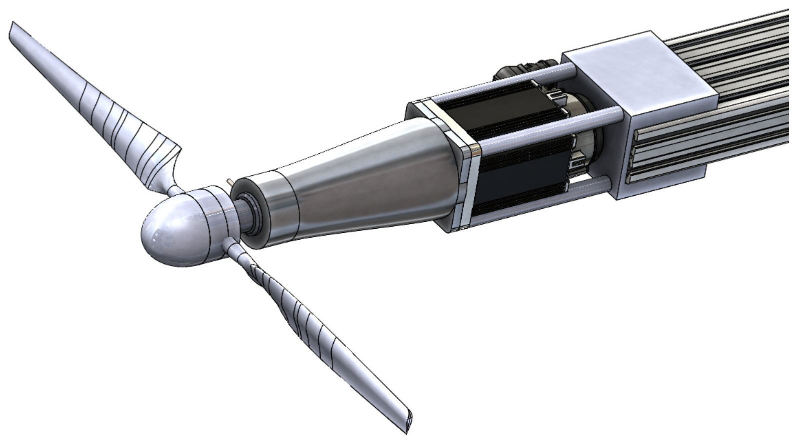

Fig. 6.3 Assembly of turbine nacelle

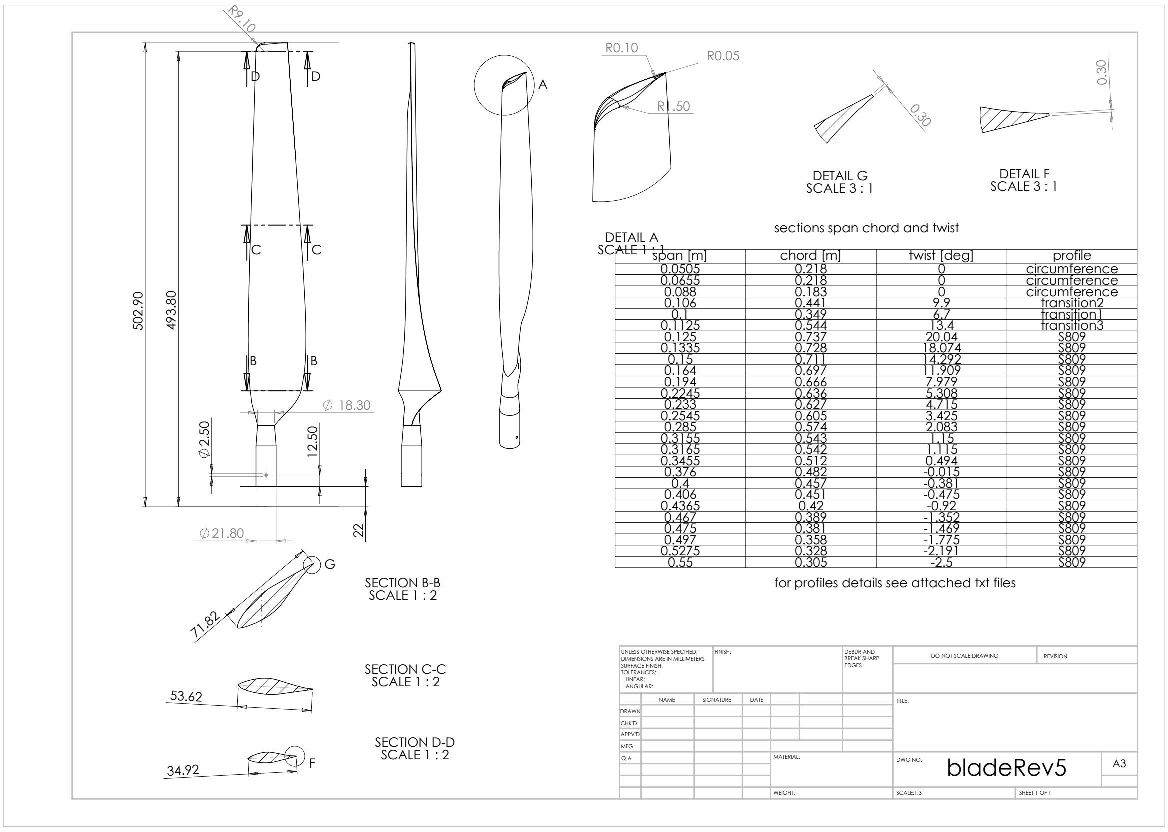

span [m]	chord [m]	twist [deg]	profile
0.0505	0.218	0	circumference
0.0655	0.218	0	circumference
0.088	0.183	0	circumference
0.106	0.441	9.9	transition2
0.1	0.349	6.7	transition1
0.1125	0.544	13.4	transition3
0.125	0.737	20.04	S809
0.1335	0.728	18.074	S809
0.15	0.711	14.292	S809
0.164	0.697	11.909	S809
0.194	0.666	7.979	S809
0.2245	0.636	5.308	S809
0.233	0.627	4.715	S809
0.2545	0.605	3.425	S809
0.285	0.574	2.083	S809
0.3155	0.543	1.15	S809
0.3165	0.542	1.115	S809
0.3455	0.512	0.494	S809
0.376	0.482	-0.015	S809
0.4	0.457	-0.381	S809
0.406	0.451	-0.475	S809
0.4365	0.42	-0.92	S809
0.467	0.389	-1.352	S809
0.475	0.381	-1.469	S809
0.497	0.358	-1.775	S809
0.5275	0.328	-2.191	S809
0.55	0.305	-2.5	S809

Fig. 6.4 Blade drawing

Chapter 7

Numerical Methods

7.1 Author's Inflow Methods

The author developed two innovative methodologies:

1. one consists in a combined approach of those of Huang and Smirnov. It results in adding the possibility of generating a generic spectrum to the latter.

2. a second one takes advantage of the POD methodology in order to introduce the inhomogeneity in the normal-to-the-wall direction

They are described in the following sections.

7.1.1 Single Point Method

In this section the authors propose a new method which combines the methods in 5.2.1 and 5.2.2. The first method is capable of reproducing a specified Reynolds stresses field at the cost of producing a divergent field. It is though limited to Gaussian isotropic spectral shapes. The second permits the generation of a generic non-isotropic spectral shape by sampling with a Dirac delta the wanted spectrum of the turbulence but it can't produce strictly inhomogenenous turbulent fields. The divergency free characteristic is crucial for the generation of a initial condition but not so limitative in case of inlet inflows. In fact the velocity field is applied on a 2D patch of the domain and the continuity equation can compensate the mass unbalances by varying the value of pressure. The PISO algorithm utilised for the scope is described in Appendix A. This is possible when the condition on the pressure field is of Neumann kind at the same boundary where the velocity is imposed.

7.1.2 Y direction POD Method

In the directions of homogeneity POD decomposition coincides with the Fourier one and POD modes with harmonic functions [46].

The proposed technique applies to those flows that exhibit one direction of non-homogeneity. In order to account for spatial coherence the method combines a partial Fourier spectral description in the homogeneity direction and a proper orthogonal decomposition of the Fourier coefficients in the non-homogeneity. A subsequent projection of the velocity field produces a time varying set of coefficients associated to each POD mode. Turbulence synthesis is performed by generating cross-correlated signals and to this aim we utilise an FFT procedure for the simulation of multi-variate weakly-stationary stochastic processes. Overall the inflow generation method satisfies the condition of a divergence free free field and reproduces statistical information encoded in the covariance tensor. An implementation based OpenFOAM library is presented and a practical application to channel flows is finally shown in order to demonstrate its effectiveness.

In figure 7.1 the first, tenth and hundredth POD eigenfunctions are reported for uniform homogeneous turbulence. Where the vertical direction is the parallel to the two walls. Figures 7.1b,7.1c,7.1d come from a classical snapshots POD study. The snapshots method present its limitations: the first modes shown are not harmonic as expected from the theory. This is probably due to a certain degree of linear correlation between the selected fields. A close-to-harmonic behaviour is recovered at high mode number. Figures 7.1e,7.1f,7.1g were derived making use of the mixed technique where the eigenfunction are function of the physical space in the direction normal to the wall and function of the wavenumber in the direction of homogeneity parallel to the wall. It can be noticed the typical symmetric structure of the FFT where the first rows of data at the bottom and the top present higher magnitudes when compared to the centre where the minimum is reached for the max frequencies. Moving from lower to higher order the lateral peaks drop.

From figure 7.2 on can notice how for the mixed FFT method introduced by the author the energy contained in the first modes is higher giving a more efficient representation of the field with a lower number of modes to be considered. Conversely for the physical space decomposition high wavenumber modes still present a relevant energy content. As a consequence it is numerically possible to truncate the series at a lower number, requiring less snapshots for the Sirovich procedure and a smaller matrix for the ARMA coefficients generator. For the showed case at the 15th mode almost the entire energy content has been included while for the standard procedure a much higher order is required to obtain the same integral energy (area under the curve in figure 7.2). This increased efficiency is mainly due

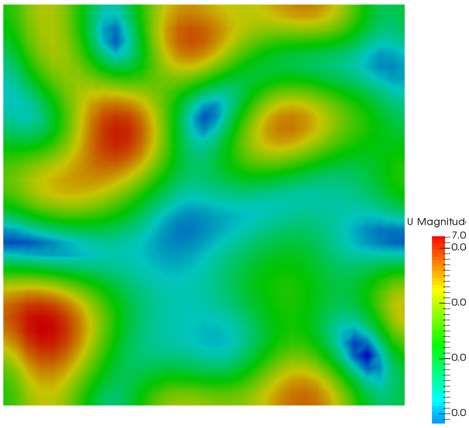

(a) Reference simulation

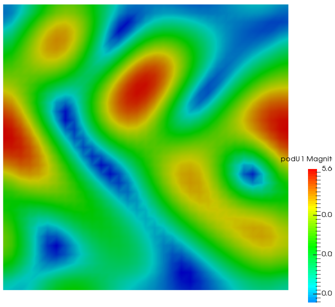

(b) Space eigenfunction 1

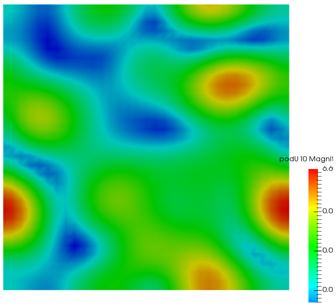

(c) Space eigenfunction 10

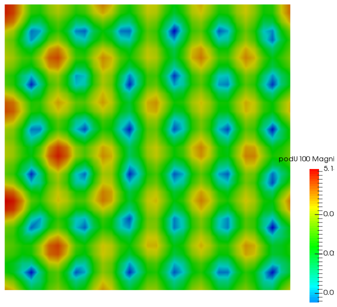

(d) Space eigenfunction 100

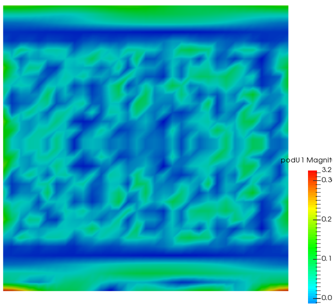

(e) Mixed eigenfunction 1

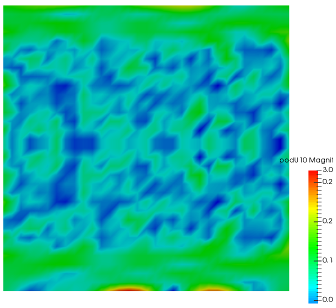

(f) Mixed eigenfunction 10

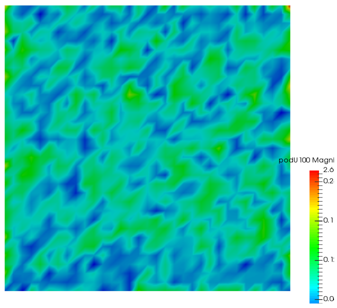

(g) Mixed eigenfunction 100

Fig. 7.1 Comparison between standard POD decomposition and mixed FFT POD decomposition

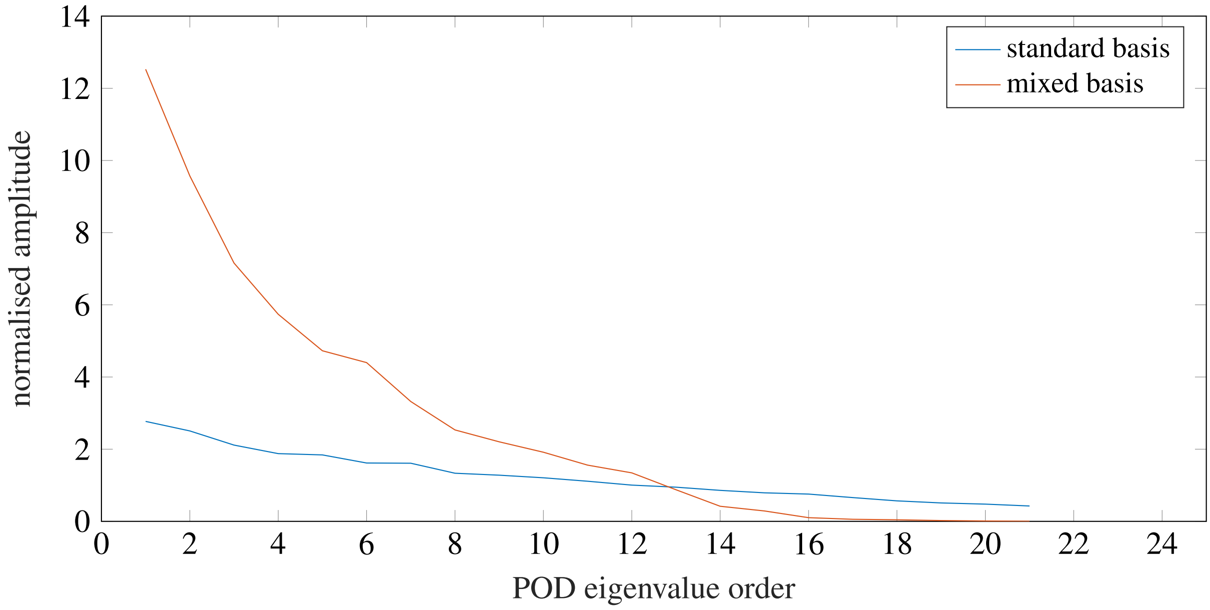

Fig. 7.2 Energy content of first 20 POD modes for the standard POD and the mixed space-wavenumber one

to the fact that rather than making the snapshots procedure to find the optimal basis for the problem, this learning process is guided by the knowledge of the homogeneity features of the field and a sine-cosine basis is forced via the FFT. In fact for the uniform homogeneous turbulence represented a fully bi-dimensional FFT procedure would be even more efficient. In case of flows bounded by a wall though the assumption of homogeneity stands only on planes perpendicular to the mentioned Y direction of non homogeneity. Hence the author implemented this methodology for the description of environmental turbulence.

7.2 Turbine Model

As previously mentioned in this thesis report, in hybrid methods the turbine is represented by forces in the computational domain rather than boundaries as in standard CFD. The flow deflection created as a consequence, generates a wake that influences the behavior of the turbine itself. Locally the sharp features of the turbine blade are not modeled as they would in standard CFD. The turbulence scale modeled are those of the size of the blade chord. This is reasonable being the mesh cells size the same order of magnitude.
The interaction mechanism between the blade element and the flow field requires appropriate mesh size and shape, solution time step and turbulence model parameters.

7.2.1 Continuous Forcing Approach

The model adopted falls in the category of the immersed boundary methods. It consists in the imposition of a source term f_i on the right hand side of (7.1).
The "NREL" organization developed the "SOWFA" libraries, [18], allowing the solution of an open rotor turbine with an actuator line strategy. The blade is modeled as set j of nodes at which the instantaneous velocity is converted, according to lookup tables (dependency on α angle of attack), into forces $\hat{f}_i^A$

$$\hat{f}_i^A(x_j, y_j, z_j, t) = \hat{g}_i\left(C_l(\alpha_j), C_d(\alpha_j), c, |\mathbf{U}|, l\right) \tag{7.1}$$

where $\hat{f}_i$ depends quadratically on $\mathbf{U}$, the sampled velocity and linearly on $c \cdot L$ product of the aerofoil local section and l length of the actuator line element, [19, 20, 69, 74, 51]. A regularization kernel is used to impose the force to the grid nodes where $f_i^A(x, y, z, t)$ is the force on the i grid cell due to the effects of the presence the j blade element at a distance equal to d_j.

$$f_i^A(x, y, z, t) = -\sum_{j=1}^{N} \hat{f}_i^A(x_j, y_j, z_j, t) \frac{1}{\varepsilon^3 \pi^{3/4}} e^{\left[-\left(\frac{d_j}{\varepsilon}\right)^2\right]} \tag{7.2}$$

One can recognize in the above formula the Gaussian normal distribution. ε regulates the width of the function. After an early stage of testing, the author developed a completely independent routine for the calculation of turbine actuator line forces making use of the standard OpenFOAM classes in order to improve the accuracy and stability of the code. The main difference achieved are

- the use of the framework of "finite volume functions“ within OpenFOAM allowing for higher flexibility
- and most importantly a more elaborated embedded algorithm of calculation of the velocities by making use of mesh cell centres, face centres and points allocated data rather than linear interpolation of the closest cells to the actuator line point.

In Figure7.3 an example of the flow field generated by the actuator line model is shown. The turbine depicted is similar to the three bladed T.E.L. design. This was intended at the beginning of the project to be used for the study of turbulence coming from a closely spaced upstream device. The magnitude of the velocity field in Figure7.3b shows how the method is capable of generating a dynamic blockage of the flow corresponding to the blades position.

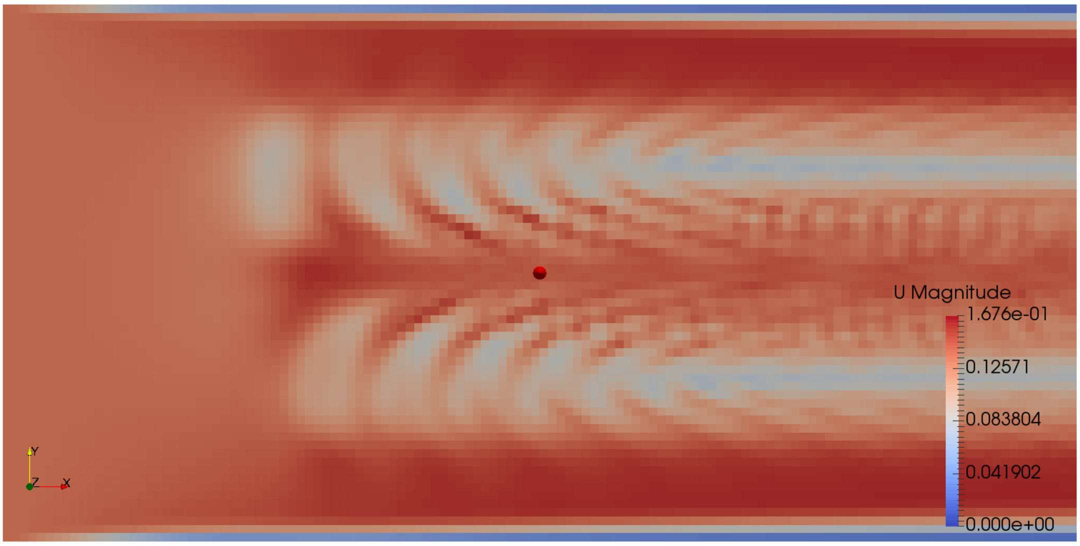

(a) Magnitude of instantaneous velocities turbine axial section

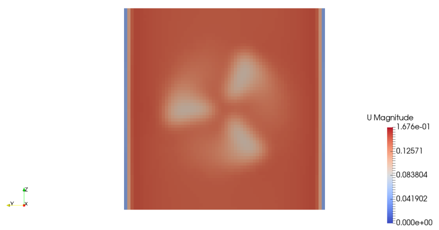

(b) Magnitude of instantaneous velocities on turbine plane of rotation

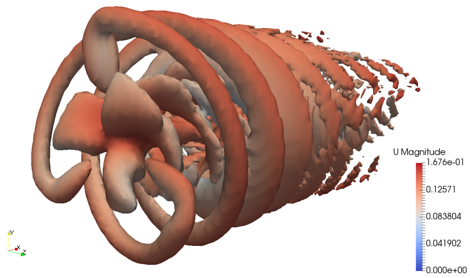

(c) Second invariant of the velocity gradient tensor

Fig. 7.3 Non-turbulent flat-inlet flow and wake generated by the actuator line forces, non-slip top and bottom walls

This blockage propagates downstream generating the turbine wake visible in Figure7.3a. A contour plot for the second invariant of the velocity gradient tensor is shown in Figure7.3c in order to highlight the generation of blade end vortices in correspondence to the tip and the hub of the turbine and the rotation introduced in the flow by the presence of the body forces.

Part IV

Results and Conclusions

Chapter 8

Experimental Results

In the present chapter the gathered data from two experimental campaigns is reported and post-processed. In section 8.1 the author analyses Acoustic Doppler Current Profiler data collected in the Ramsey Sound location in the place were is at the present time operating the TEL hydrokinetic tidal turbine. The study is carried out making use of the advanced statistical tools previously illustrated such as POD and shows some interesting peculiarities of the local flow and features of the Karhunen–Loève decomposition. The experimental setup in section 8.2 is briefly described in chapter 6. The author designed and assembled the test rig and conducted the Campaign. The turbine torque and thrust signature are compared for two different controllers in the attempt of minimising dynamic loads hence fatigue on a channel deployed machine.

8.1 Ramsey Sound ADCP Data Analysis

Three velocity sets (figures 8.2, 8.3, 8.4) have been extracted from a 11-days history and studied according to the traditional methods such as

- statistical ordinary methods (Mean, Reynolds stresses, turbulence spectra) and
- POD analysis and time coefficients turbulence spectra.

The mean data velocity components (Figure 8.5) show that the considered site has a peculiar boundary layer shape generally non in accordance with the laws obtained for smooth walls. The vertical component present a residual velocity that could be due to a misalignment of the measuring device but it is also possible that locally a non flat seabed could cause an average flow.

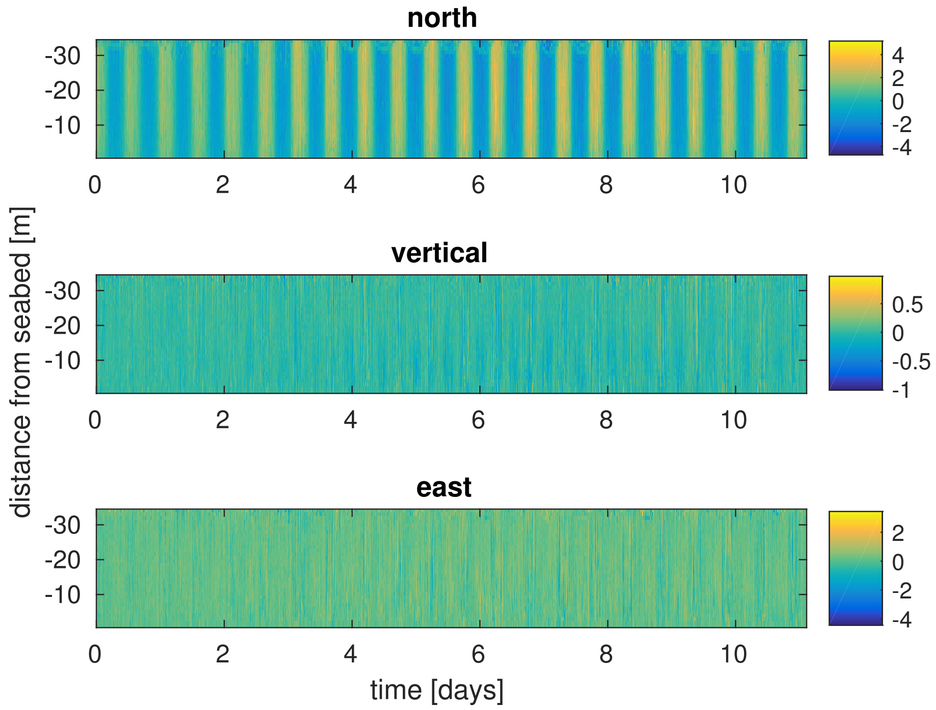

Fig. 8.1 "Ramsey Sound" Site Velocity components over a period of 11 days during Strong Spring Tides

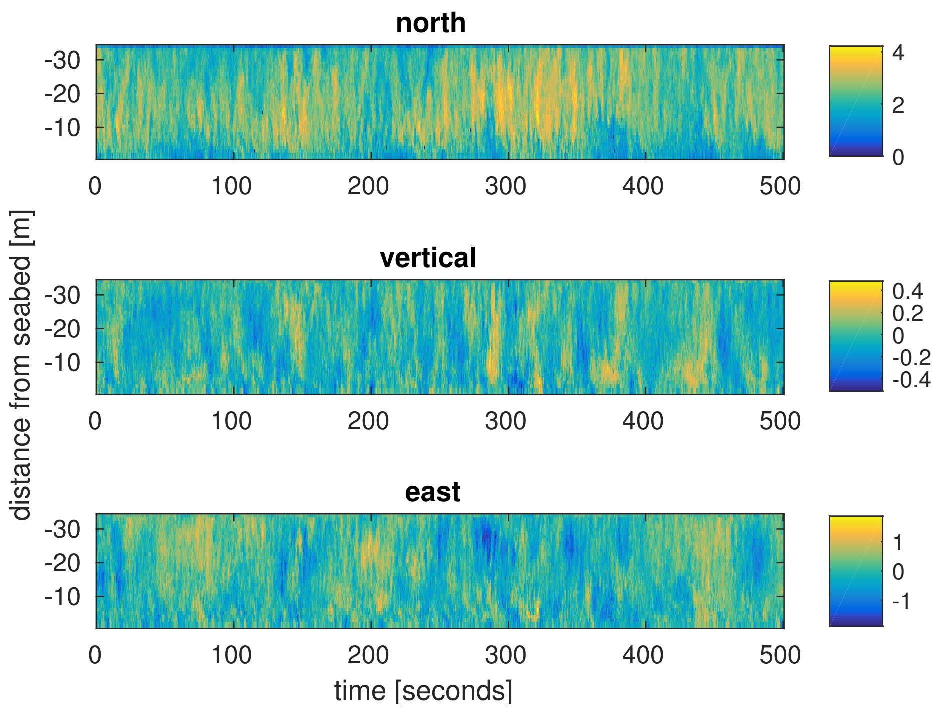

Fig. 8.2 "Ramsey Sound" Site Velocity components set 1

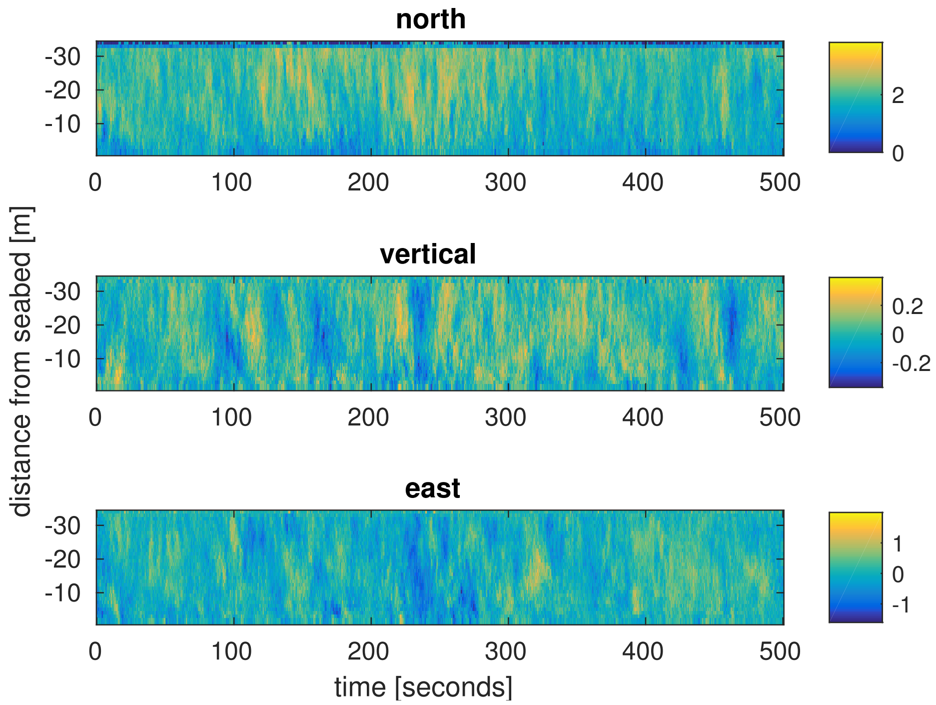

Fig. 8.3 “Ramsey Sound” Site Velocity components set 2

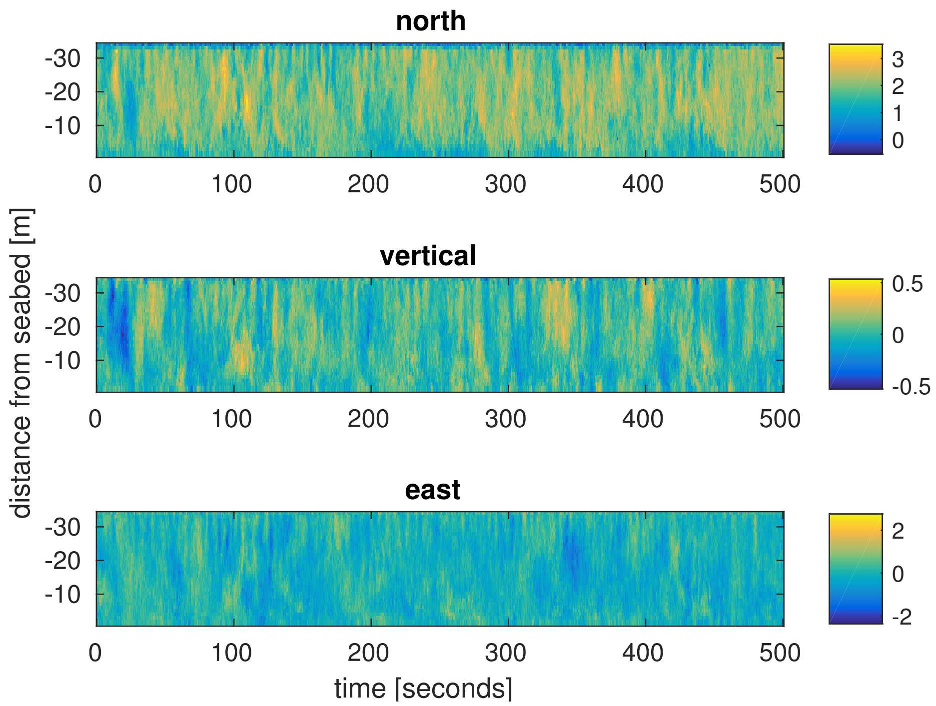

Fig. 8.4 “Ramsey Sound” Site Velocity components set 3

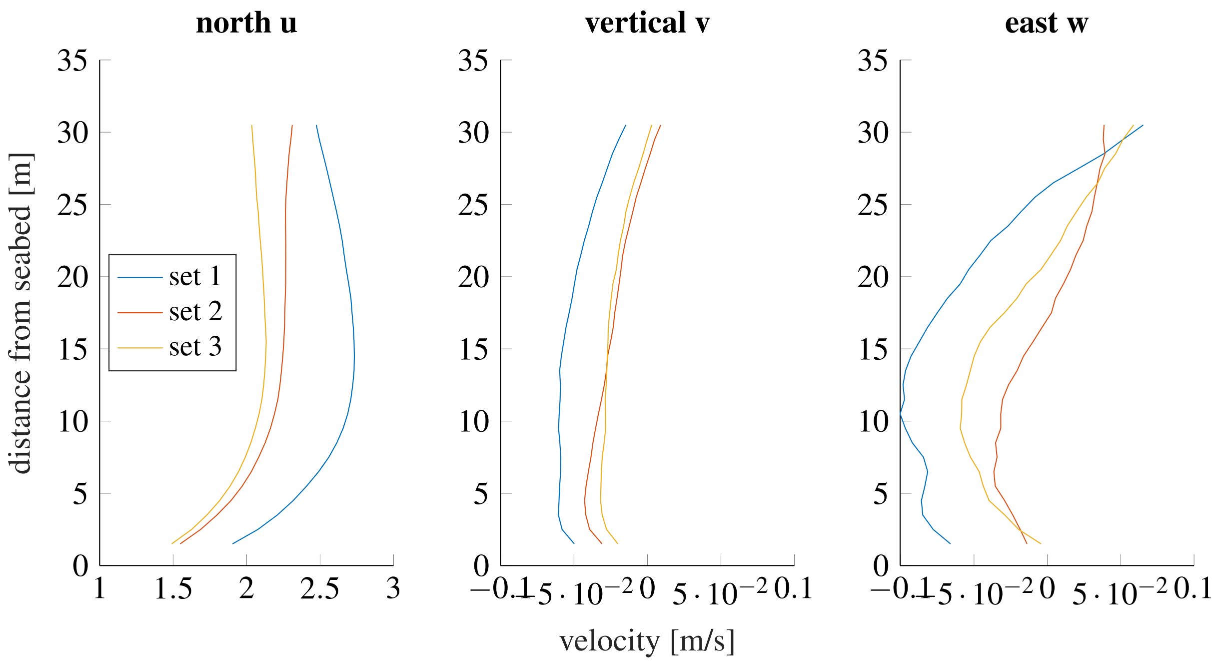

Fig. 8.5 “Ramsey Sound” Mean Velocity Components for selected fields in figures 8.2,8.3,8.4

Set 2 and 3 present very similar mean velocity profiles while Set 1 was selected in the strongest flow condition occurring in the data set analysed. When looking at the Reynolds stresses (Figure 8.6) on the other hand set 3 differs in particular close to the sea surface probably due to a condition of strong wave motion.

The POD techniques of analysis showed by the author in chapter 3, were applied to the three sets with the final aim of translating to an inflow condition for the turbine model developed. The coupling of the two is postponed to possible further studies.

In figures 8.7 and 8.8 the POD eigenfunctions in their north component are reported. One can notice the first mode for each set has a shape very close to the mean flow in accordance with the POD theory. As we move through the numbers the arched shape of the first modes is replaced by harmonics. Harmonics are eigenfunctions of homogeneous flows invariant with translation in the plotted direction. It is a very interesting result that after just 3-4 modes homogeneity is recovered. Homogeneous turbulence can be produced with relative ease hence a combined system of few POD modes in addition to an appropriate Fourier system could constitute a interesting field of research for inflow generation techniques. This was proposed by Drault et Al. [24] but the mentioned author was not able to carry out the idea to a working stage.

It is also particularly significant the result obtained in figure 8.9. In fact the three reported time histories present different statistics. This is in particular true for set 3 when compared to

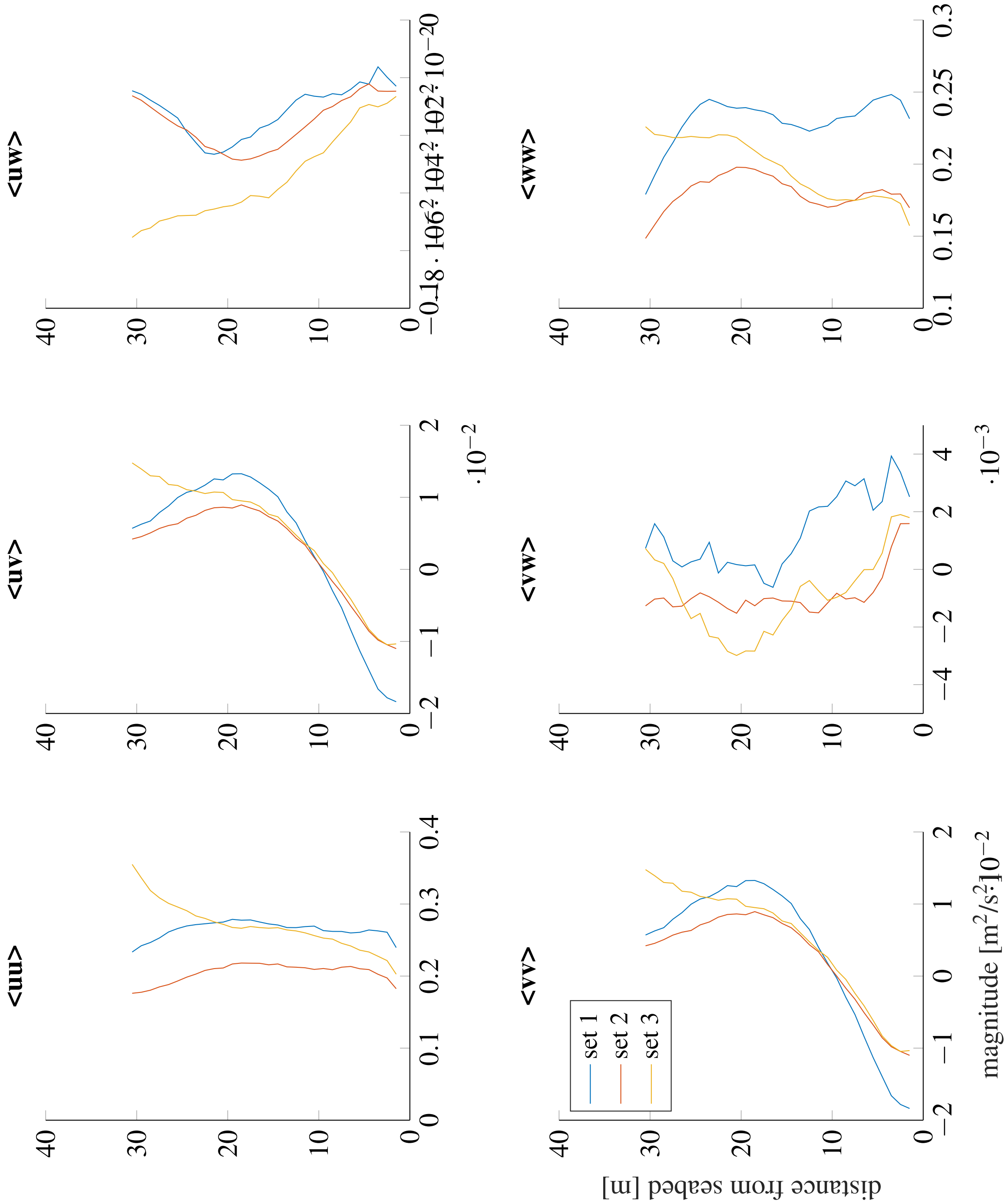

Fig. 8.6 "Ramsey Sound" Reynolds Stresses for selected fields in figures 8.2,8.3,8.4

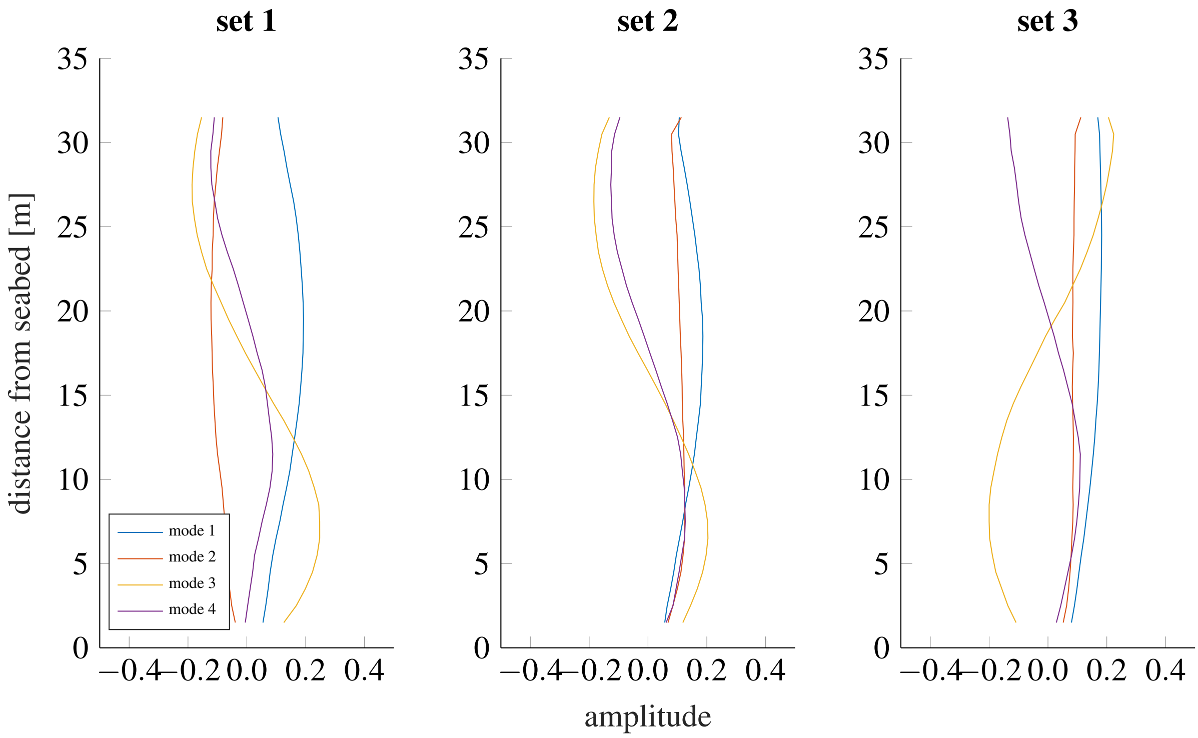

Fig. 8.7 “Ramsey Sound” POD modes 1 to 4 in the flow direction x for selected fields in figures 8.2,8.3,8.4

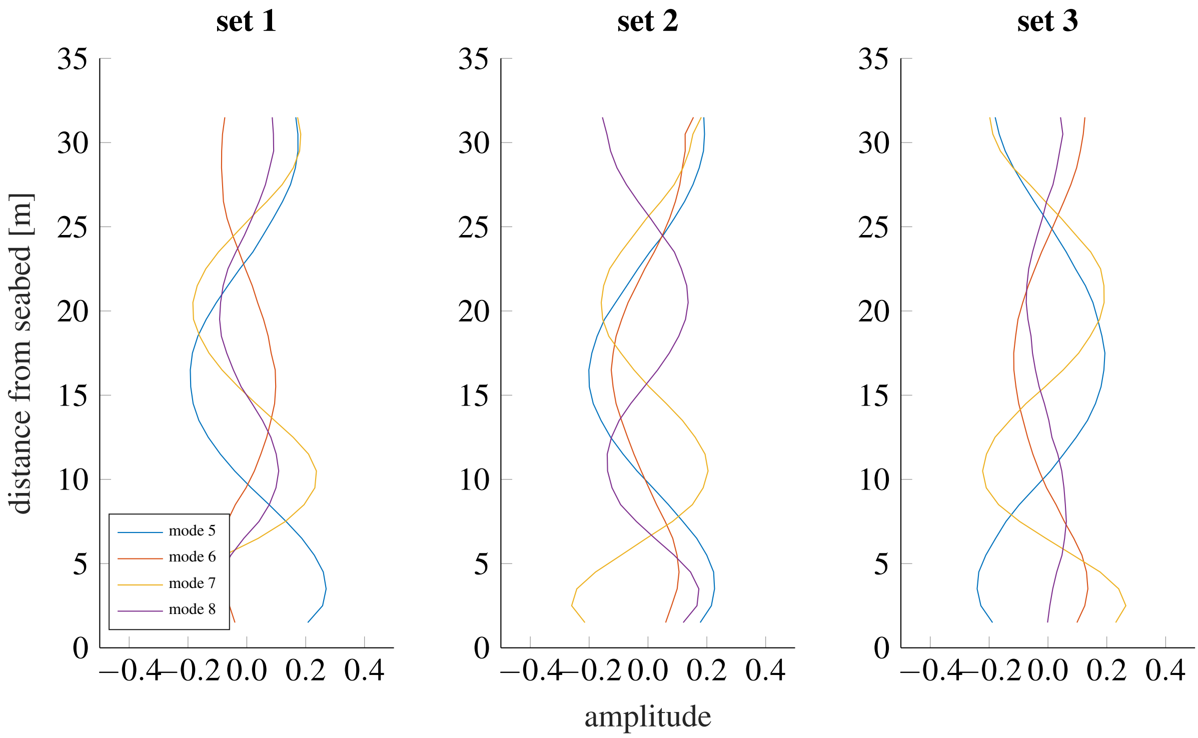

Fig. 8.8 “Ramsey Sound” POD modes 5 to 8 in the flow direction x for selected fields in figures 8.2,8.3,8.4

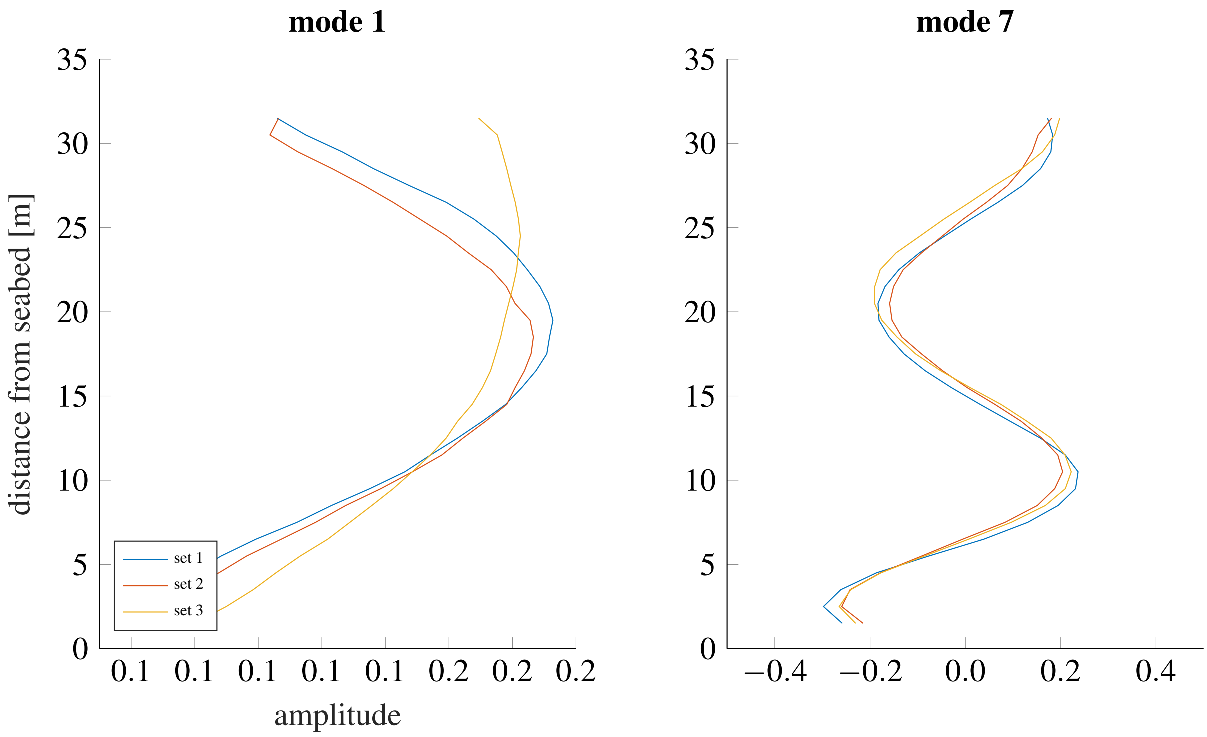

Fig. 8.9 “Ramsey Sound” POD modes 1 and 7 in the flow direction x for selected fields in figures 8.2,8.3,8.4

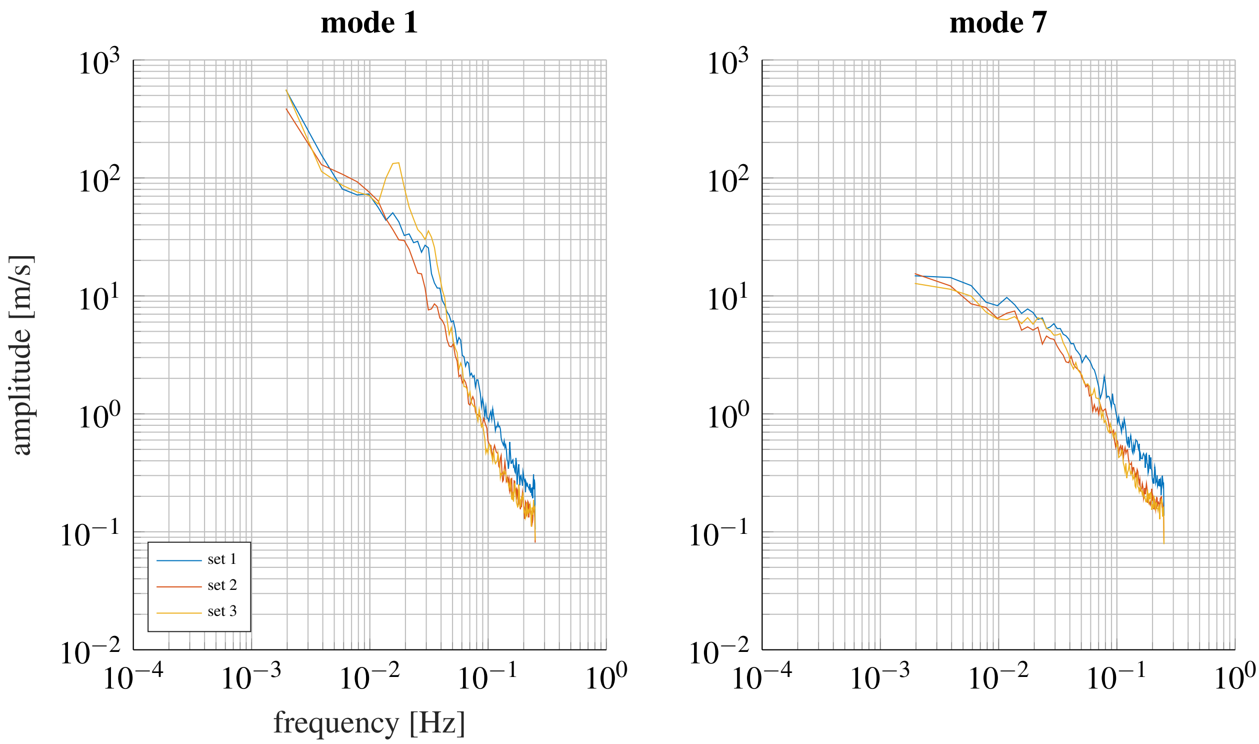

Fig. 8.10 “Ramsey Sound” POD modes 1 and 7 time coefficients power spectral estimation for selected fields in figures 8.2,8.3,8.4

1 and 2. Given this difference one would not expect the them to present just at the 7th mode the exact eigenfunction shape. This is once more confirming that in the Ramsey Sound site turbulence even though particularly strong, has still homogeneous features at relatively large scales. The period of the harmonic function in figure 8.9 is around 15-20m.

The recovery of homogeneity has a consequence also on the pseud-spectrum of the time coefficients $a(t)$ of the decomposition in figure 8.10. A peak of the frequency spectra in the north direction is reflected into a peak in the pseudo-spectrum for set 3. The pseudo-spectrum of the coefficient $a(t)_7$ seems instead associated to vertical movements being very similar to those in the central column in figure 8.11. Also the differences evident among the three sets seem to vanish in this particular mode. In conclusion in the present session the author reported and original analysis of the retrieved data making use of the POD technique. The main outcome is the confirmation the description making use of POD eigenfunction is optimal in representing the peculiar features of a flow: in just a few modes homogeneity is recovered. This result evidences the power of such a description that can be utilised in flow generation methodologies.

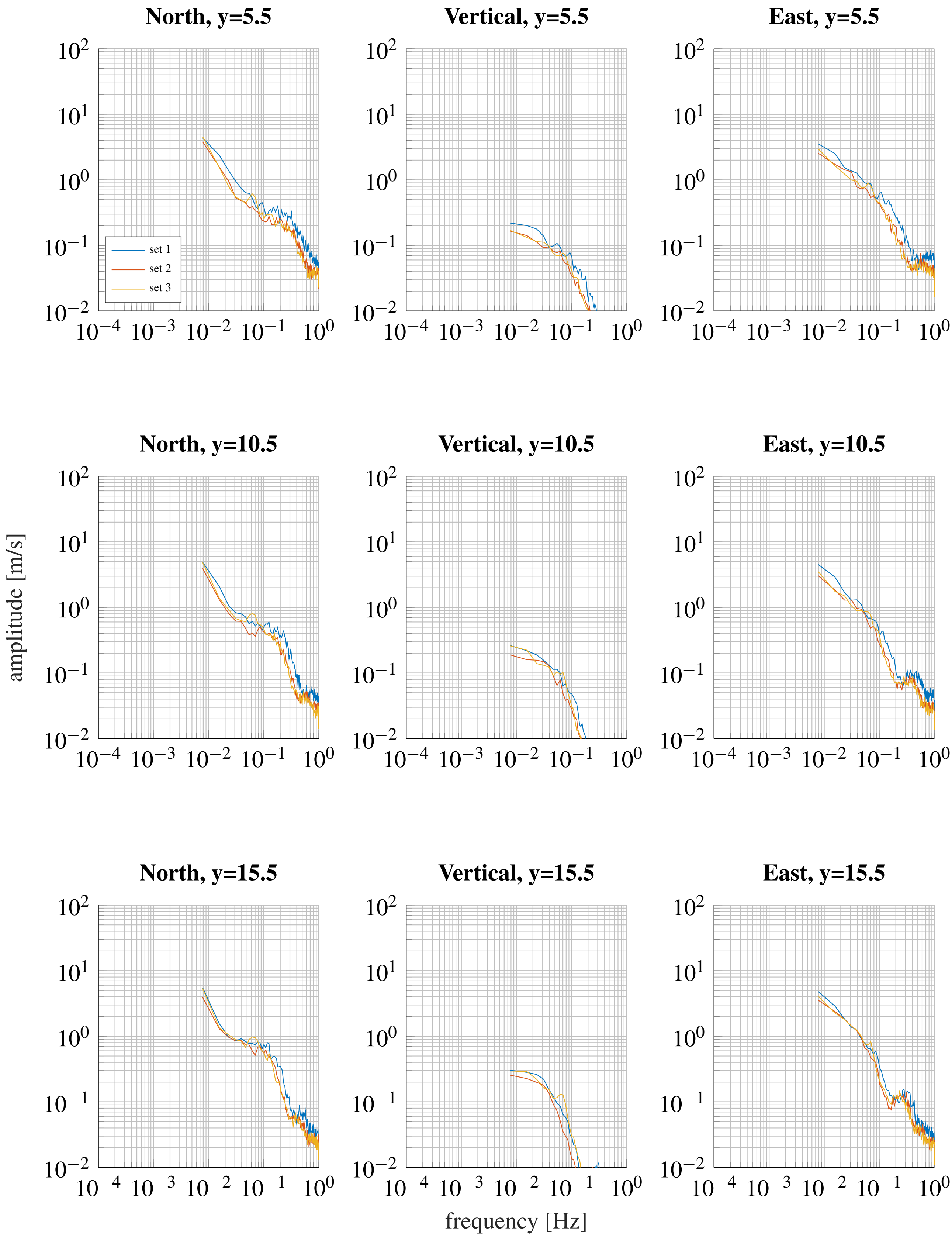

Fig. 8.11 “Ramsey Sound” Power Spectral Density of flow velocity components for selected fields in figures 8.2,8.3,8.4

8.2 IFREMER Experimetal Campaign

8.2.1 Turbine Mean Response

The author conducted the experimental campaign making use of a own-designed test rig with the aim of studying fast control techniques for the alleviation of dynamic loads caused by turbulence. The campaign is summarised in a cloud of points in the characteristics power and thrust coefficient - tip-speed-ratio plane. The point cloud is presented alongside predictions making use of the validated NREL BEM code called FAST. It shows how the turbine characteristics result lower in power and thrust when compared to the 10m full rotor wind turbine due to Reynolds effects. The turbine was pitched to 6° in order to test whether the patented method by Tidal Energy Limited of increasing the rotor speed to reduce the load could be also applied to the unsteady forcing case.
Furthermore this data is used in chapter 9 in order to validate the steady-state performances of the turbine model developed.

8.2.2 Turbine Controllers Comparison

The author tested a number of 4 controllers respectively trying to keep rpm, torque, thrust and power constant. As shown in figure 9.7, the thrust and power controllers were proven to be inadequate. They have been implemented in Labview making use of the controllers toolbox.
Of better success where the torque and rpm controllers provided by Bosch for their permanent magnet motor controlling the turbine. The latter two were tested in two tank turbulent conditions consisting in:

1. $0.9m/s$ of average flow velocity and 2% turbulent intensity
2. same average flow as the above but a wave maker generator was activated producing waves at a frequency of $0.5Hz$ and peak-to-peak amplitude of $280mm$

One can see in figure 8.14 the velocity spectra for these two conditions coming from the Nortek ADV positioned a meter upstream the turbine. Due to poor seeding of the tank the data was particularly dirty and required substantial smoothing and outliers removal.

In waves-on condition a peak appears in the time spectra of the streamwise and cross stream directions corresponding to the period of 2 seconds of movement of the wave-generating paddles.
Finally the controllers performances is reported in figure 8.15 in terms of power spectral

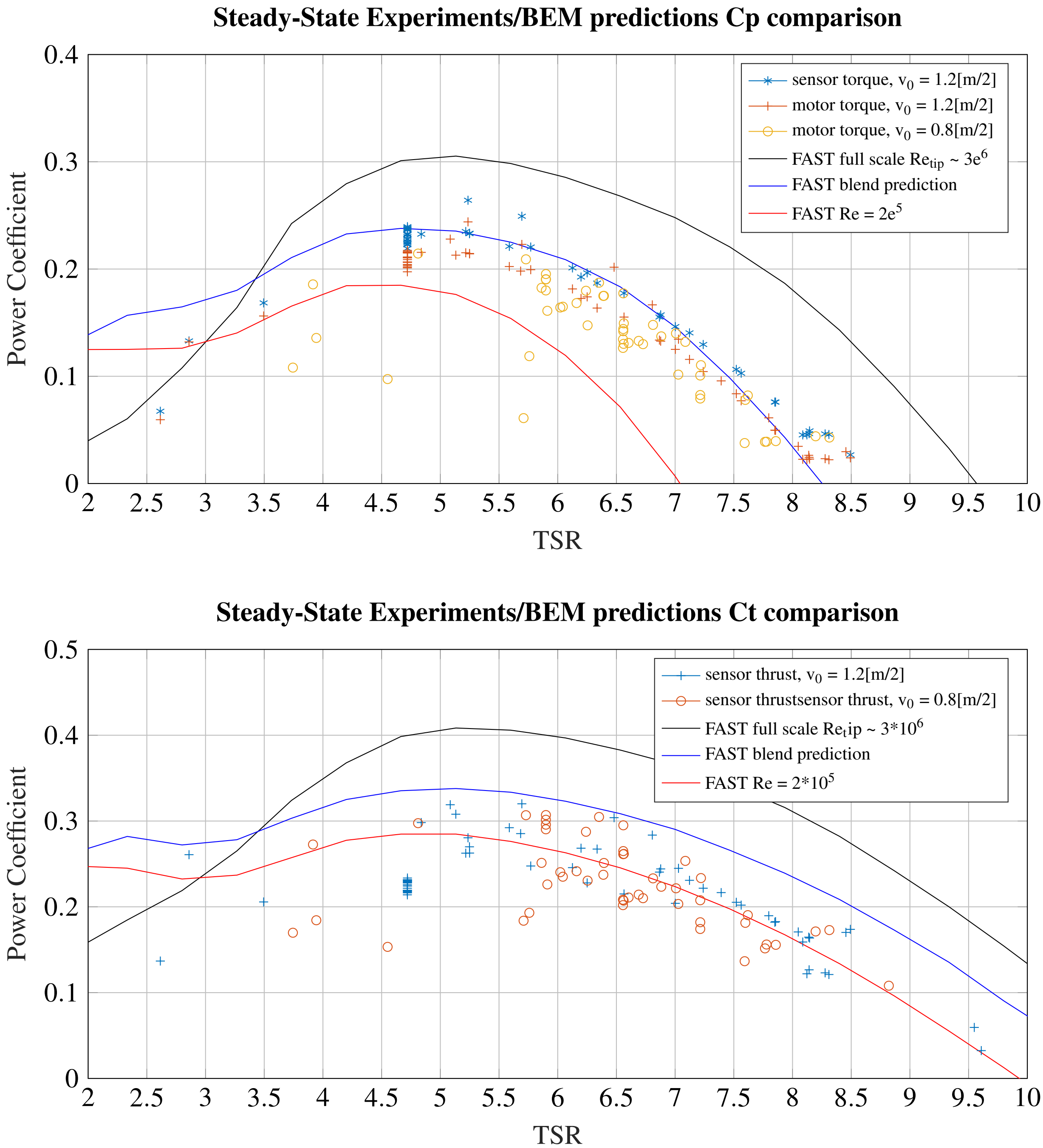

Fig. 8.12 Power and Thrust Characteristics cloud from IFREMER campaign

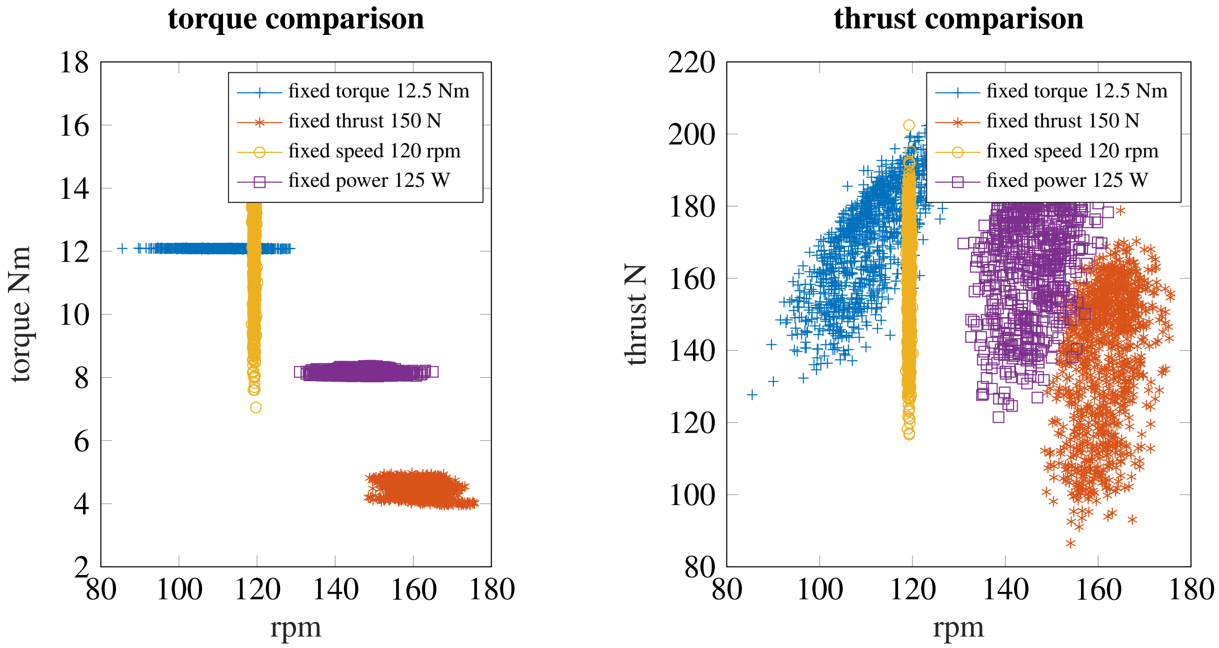

Fig. 8.13 Dynamic Power and Thrust Loci vs RPM for constant RPM and constant Torque controllers

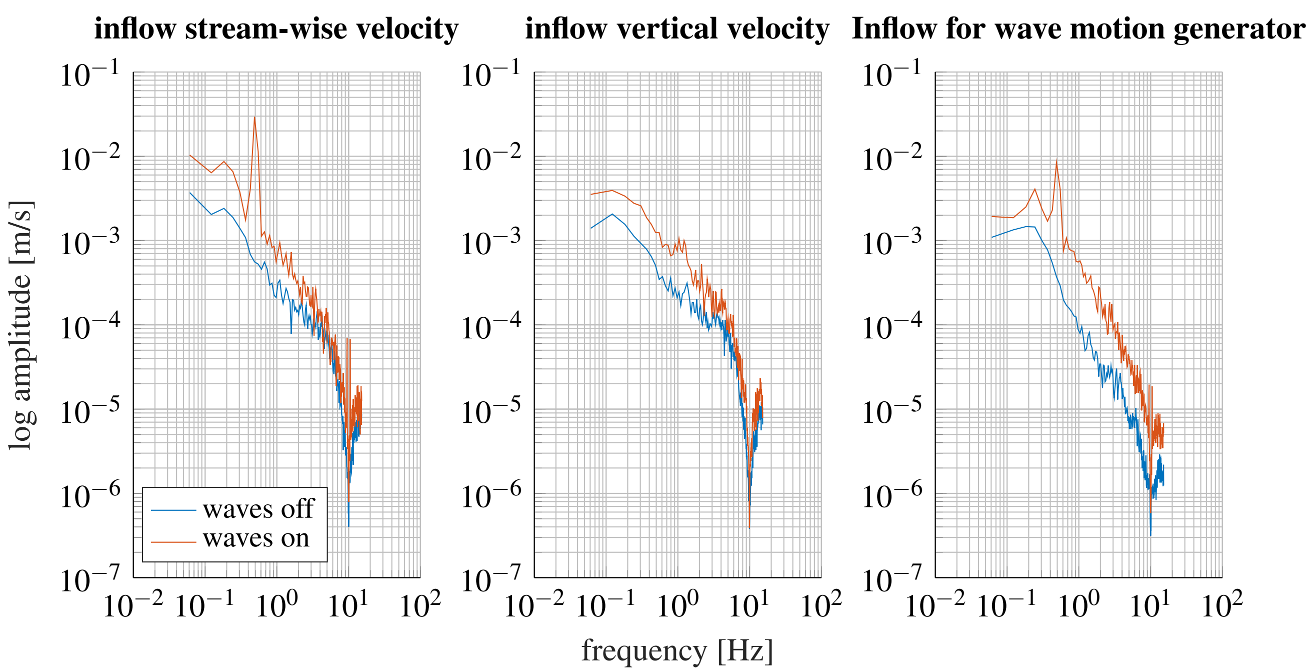

Fig. 8.14 "IFREMER" Power Spectral Density of flow velocity components from ADV

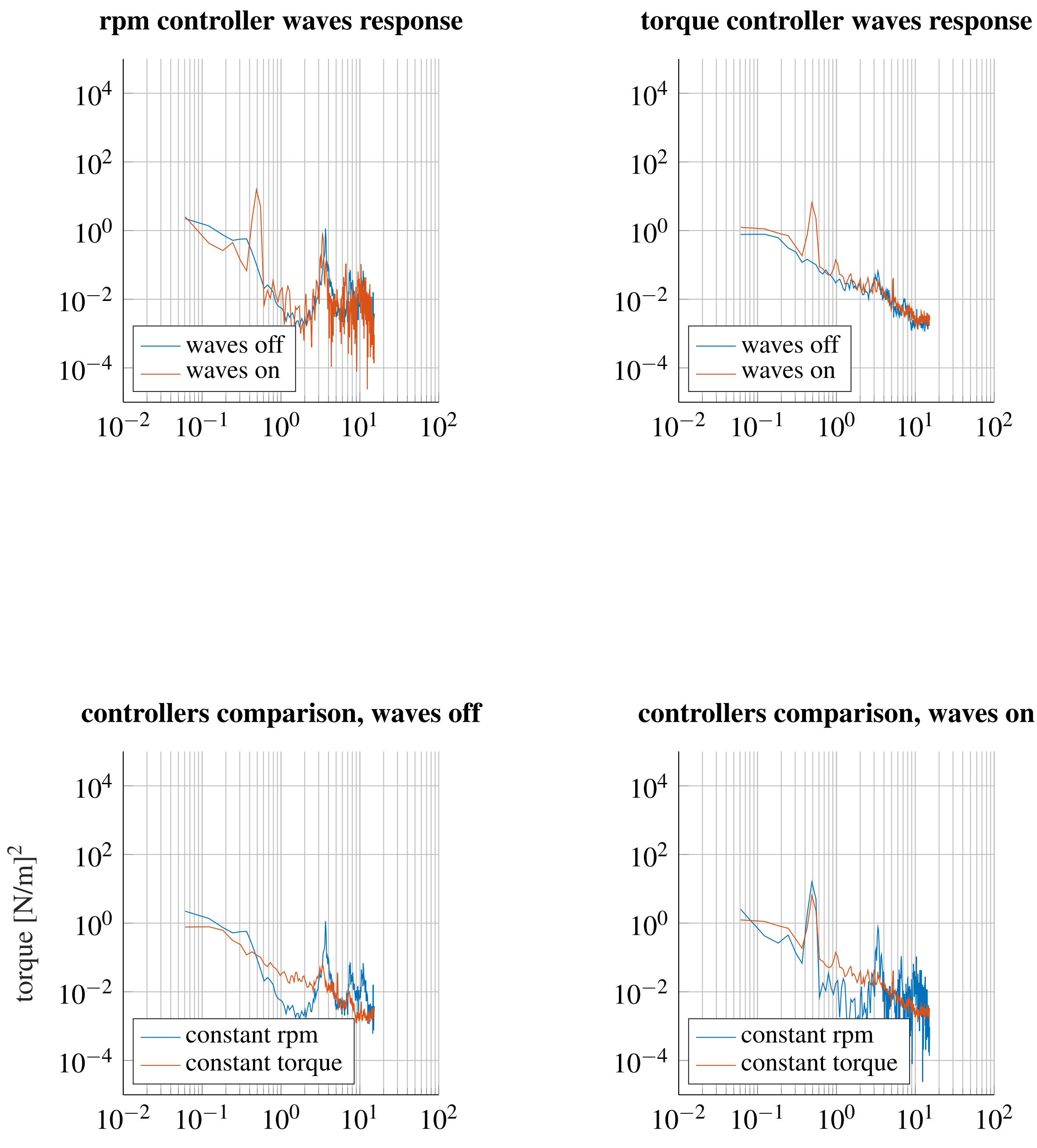

Fig. 8.15 “IFREMER” Torque PSD for constant RPM and constant Torque controllers

density of the torque signature and in 8.16 in terms of thrust.
One can see how the fast constant torque operation does not smooth out the slow $0.5Hz$ peak neither in the torque nor in the thrust signature. Also does not present any visible advantage over the constant speed controller in reducing the fluctuations in thrust due to turbulence. Conversely it proven effective in dampening torque fluctuations at high frequency.

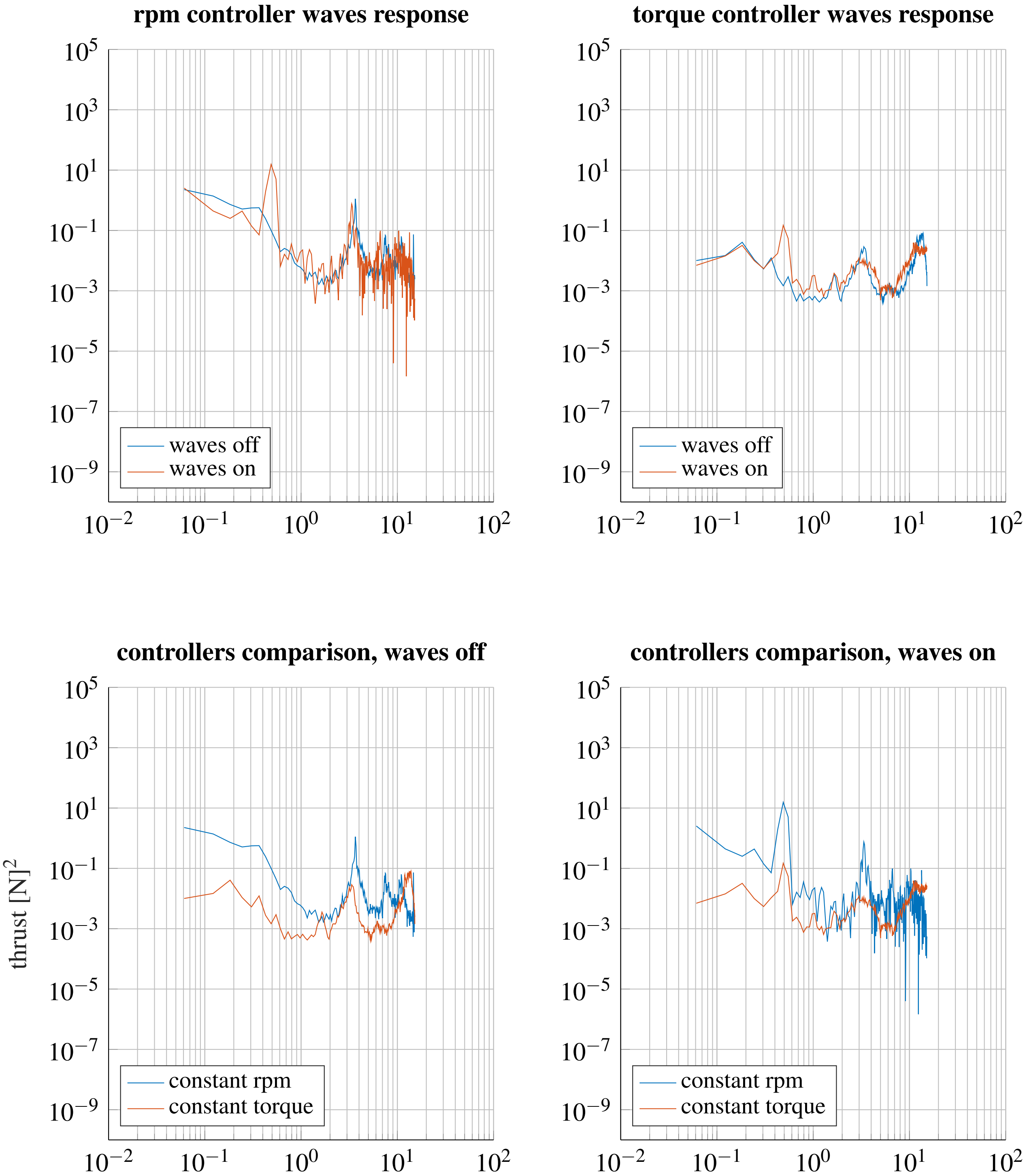

Fig. 8.16 “IFREMER” Thrust PSD for constant RPM and constant Torque controllers [x-axis in Hz]

Chapter 9

Turbine Model Validation

The current chapter aims to verify the performance matching between the experimental data acquired and those produced by the model described in Section 7.2. It is divided into two main sections:

- in Section 9.1 the sensitivity to simulation parameters such as mesh density, time stepping and ε parameter is investigated
- in Section 9.2 the actuator line model input parameters are tuned in order to match the experimental characteristics.

The base OpenFoam case used for this analysis consists in a parallelepiped bound of size $4x2x4$ units (equivalent to meters in the experimental set-up). The mesh is made of hexaedral cells in the number of $40x20x40$. The turbine is a 1-m diameter rotor oriented according to the first Cartesian direction, namely x, and oriented towards the inlet positioned in the lowest range of the x axis.

- On two boundary planes orthogonal to the y axis periodic boundary conditions are imposed.
- The top and bottom bounds, normal to z, present free-slip conditions.
- At the inlet a laminar flat flow of intensity 1 representing the experimental $1[m/s]$ is applied.
- At the outlet zero-gradient conditions are applied.

The initial condition for each single simulation is mapped from a similar-to-free-wheeling turbine simulation in order to minimise the transitory effects of the wake generation inside the considered numerical domain.

9.1 Parameters Dependency Study

This section aims to study the dependency of turbine performances on the case set up. All the studies reported in the continuation are carried out in flat-profile and laminar flow inlet. The turbine rotational speed is regulated linearly from a maximum of 20 to a min of $0[rad/s]$ in order to obtain tip speed ratio power and thrust coefficient characteristics spanning from 10 to 0. In the pictures below only the range 3 to 9 is reported being the part of major interest.

Sweep Speed The first parameter investigated is the dependency of the curves on the time period taken to complete the rotational velocity span.

In picture 9.1 one can see that for both power and thrust from time periods of 5 to 25 curves are practically overlapped. The only curves differing are for 1,2 and 3. $t = 5[s]$ is the minimum period for dynamic effects not to be visible on the curves. Hence it is selected as computationally optimal choice in the continuation of the current chapter.

Inlet and Outlet Distance It is well know in CFD that results of an analysis can be severely affected by the vicinity of a boundary. Also open rotor turbines such as hydrodynamic tidal turbines are constrained in power extraction by the so-called Betz limit. Positioning, for example, the inlet excessively close to the turbine rotor would fictitiously increase its ideal performances by increasing the rotor flow axial velocity up to the undisturbed values. This would bring the ideal performance limit from the Betz one to the one for close rotor turbines if the inlet coincides with the rotor plane. In Figure9.2 the number 0 in the legend stands for unchanged position to the reference 1 unit from the inlet. 0.75 represent the closest position to the inlet (0.25 from it) and -2 the furthest.

Blockage Factor Some percent of deviation is visible when the mesh result 40% of the base case, around the size chosen there is no relevant variation.

Mesh Refinement A relevant shift of the power and thrust curves is only visible for the first three characteristics. Mesh refinement of 1 corresponds to 5 elements across the blade span.

ε Parameter This parameter is that responsible for the force spread in the computational domain. Ideally it should be kept in a constant relation with the local blade chord size for physical meaning. Churchfield [20] claims for computational instabilities it has to be at least the double of the mesh size. In the showed data the criterion has been strictly respected

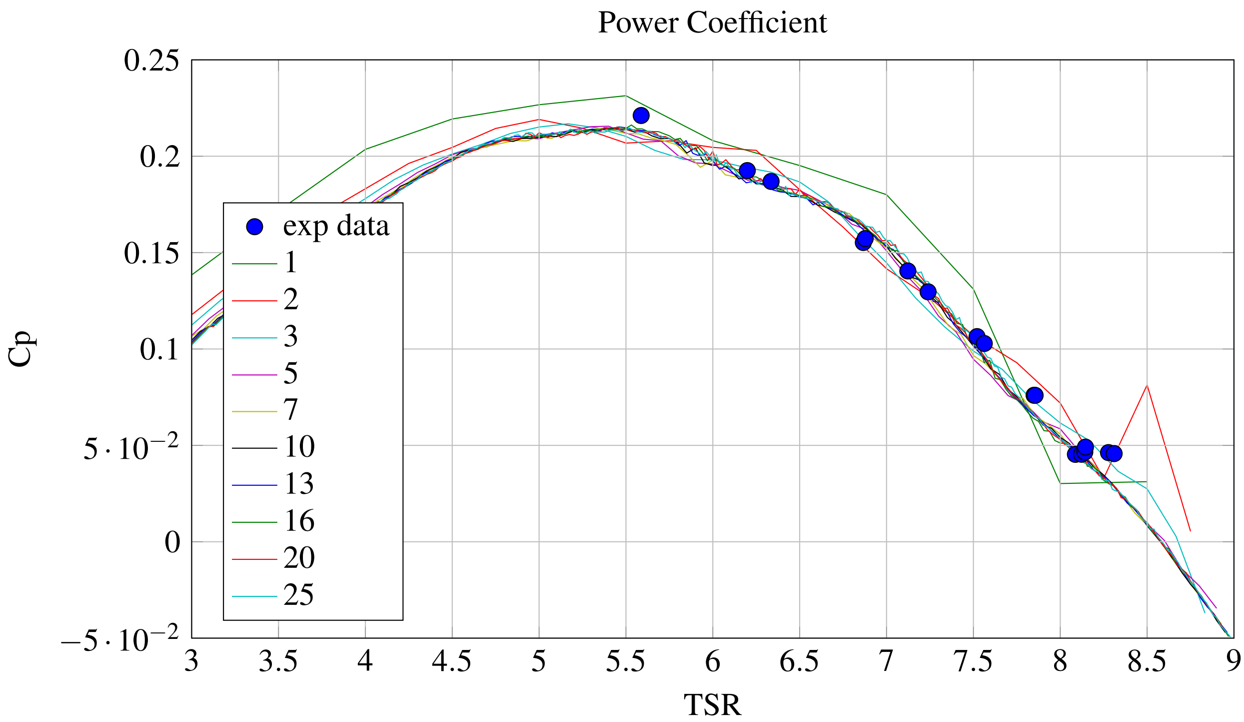

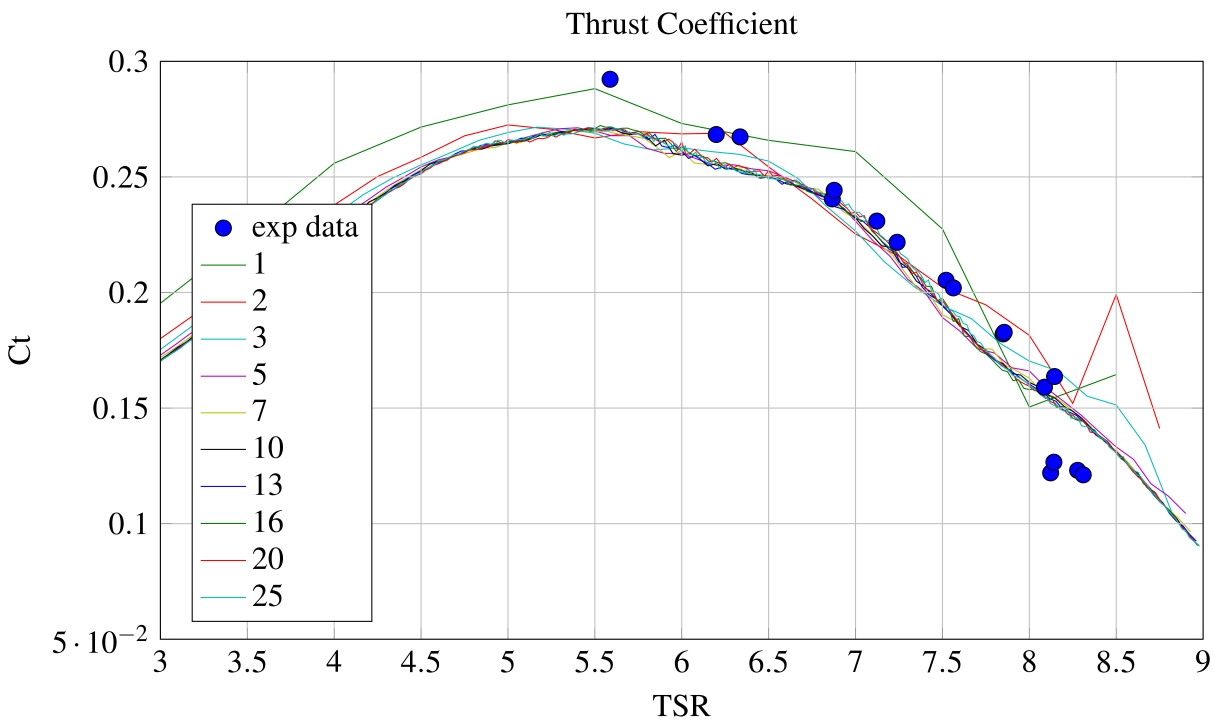

Fig. 9.1 Power and Thrust Characteristics dependency on TSR sweep period in time units $[s]$

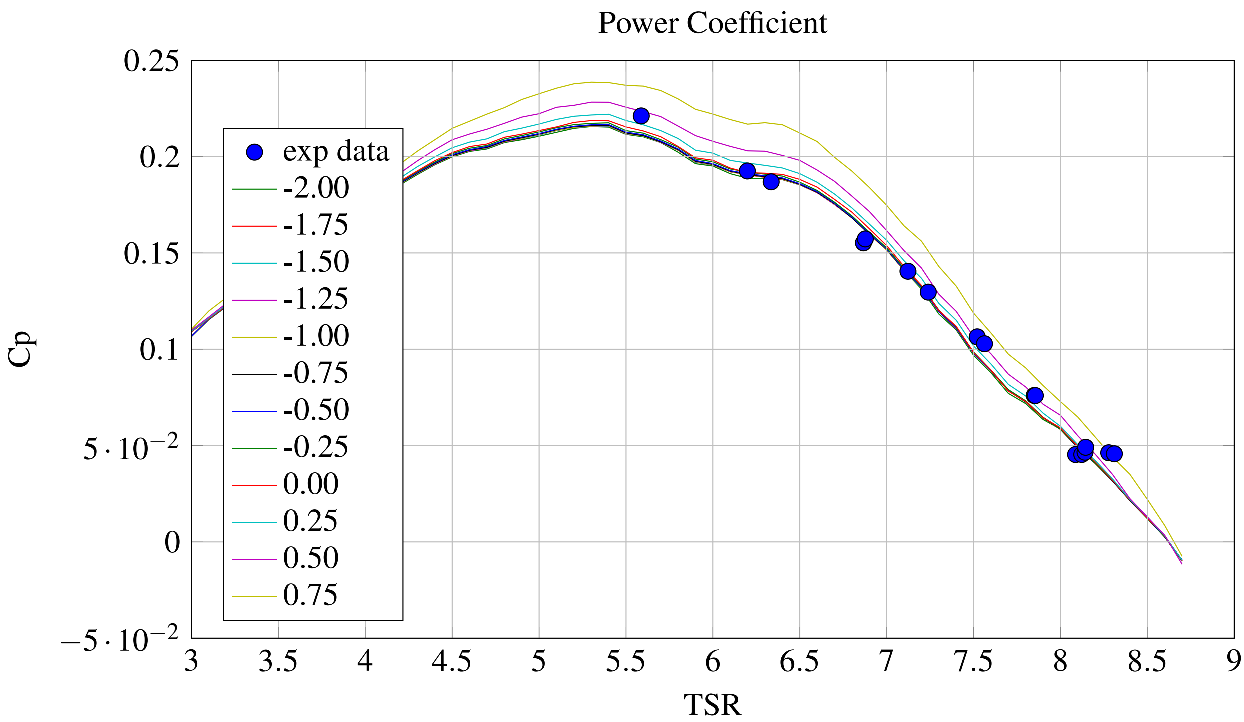

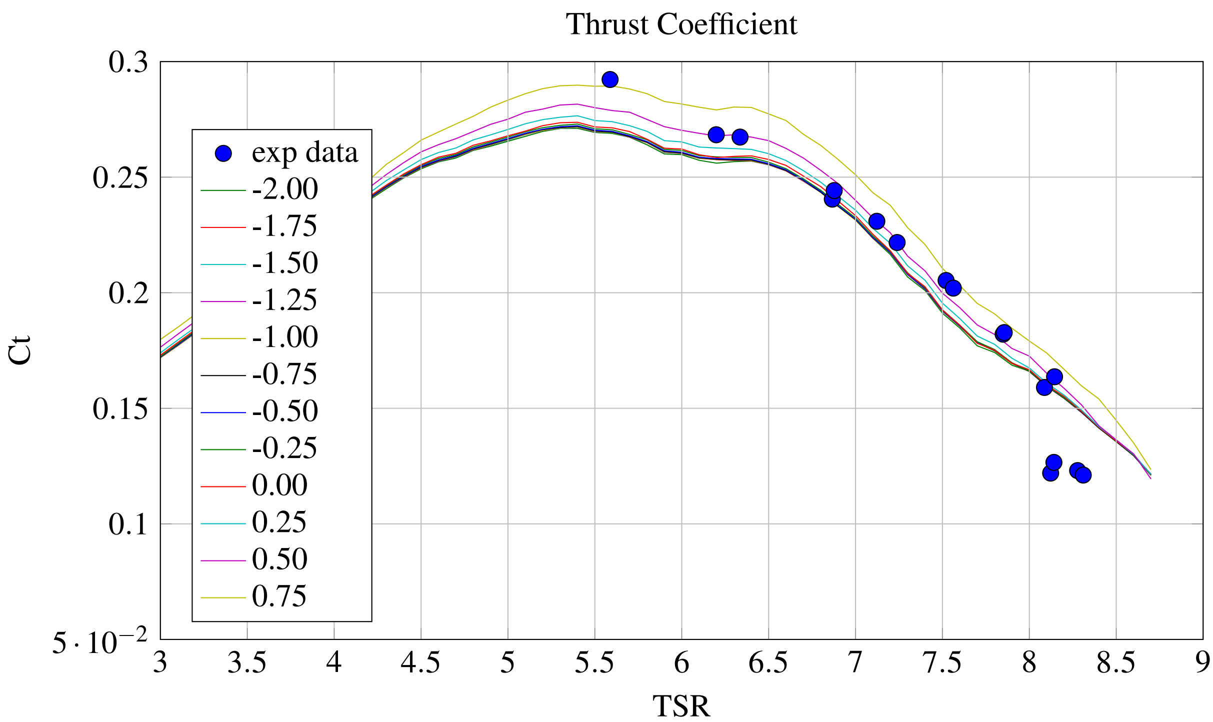

Fig. 9.2 Power and Thrust Characteristics dependency on inlet boundary x position. Turbine is in $x = 1$

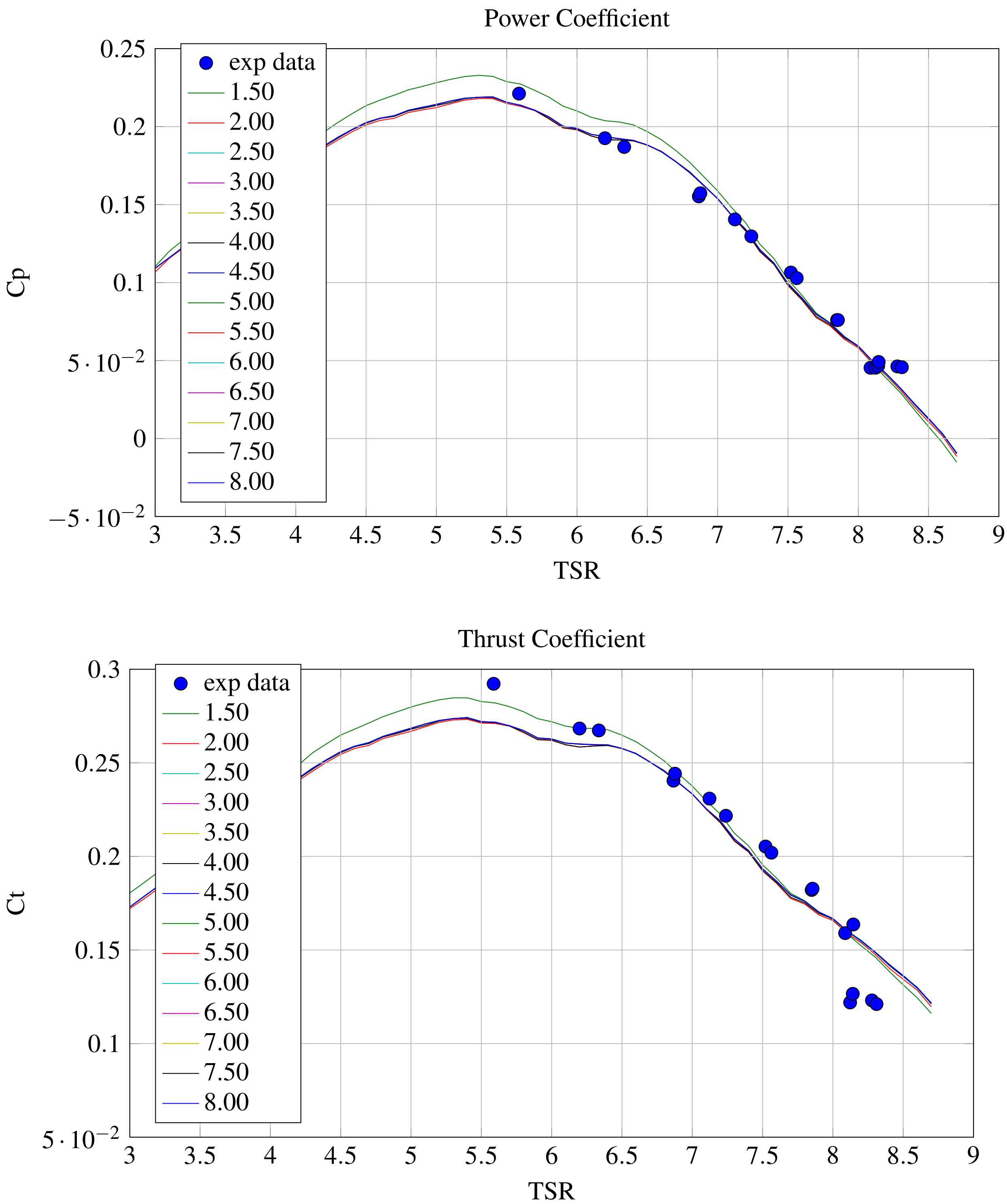

Fig. 9.3 Power and Thrust Characteristics dependency on outlet boundary x position. Turbine is in $x = 1$

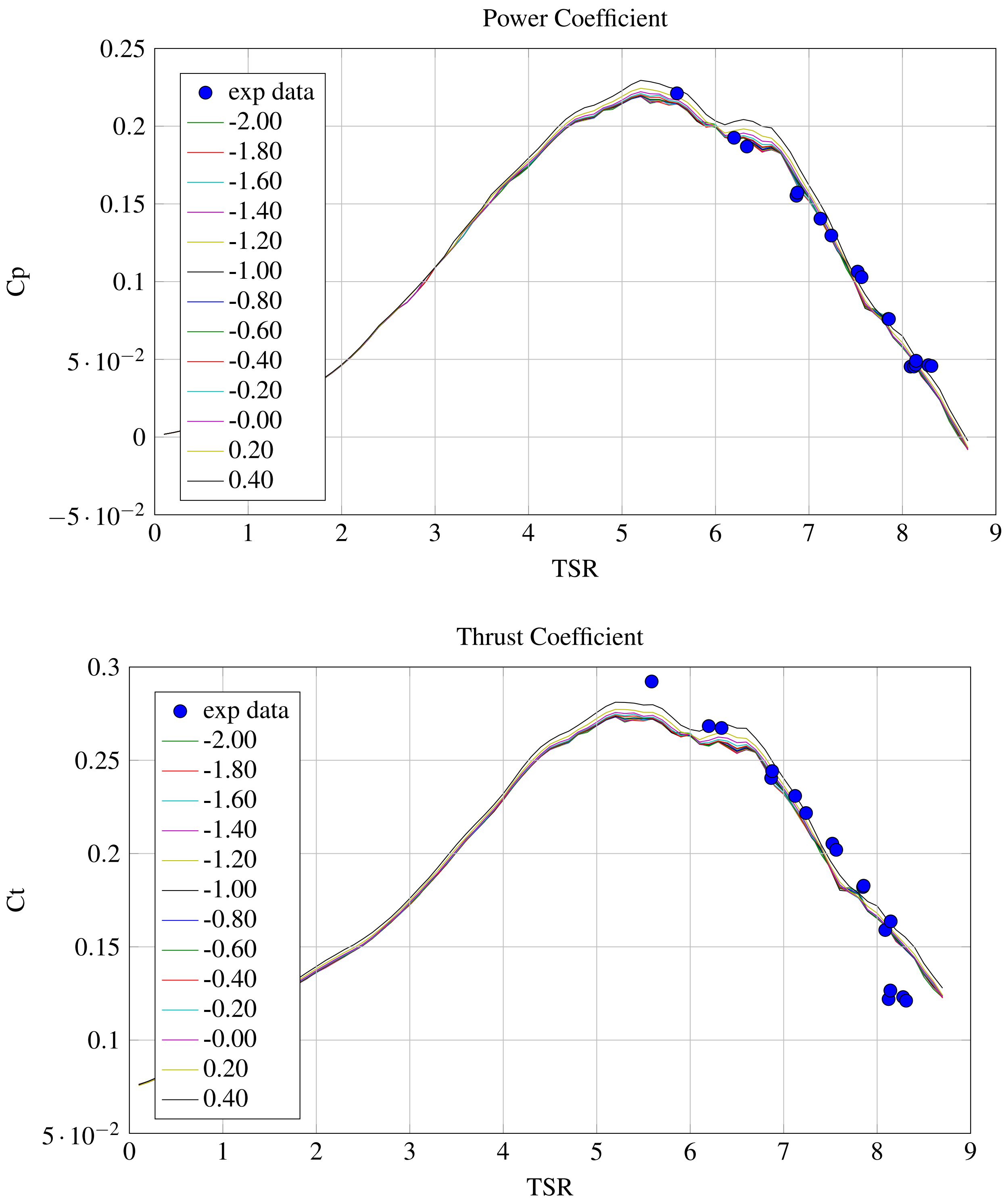

Fig. 9.4 Power and Thrust Characteristics dependency on the mesh size fraction relative to the reference (blockage factor study).

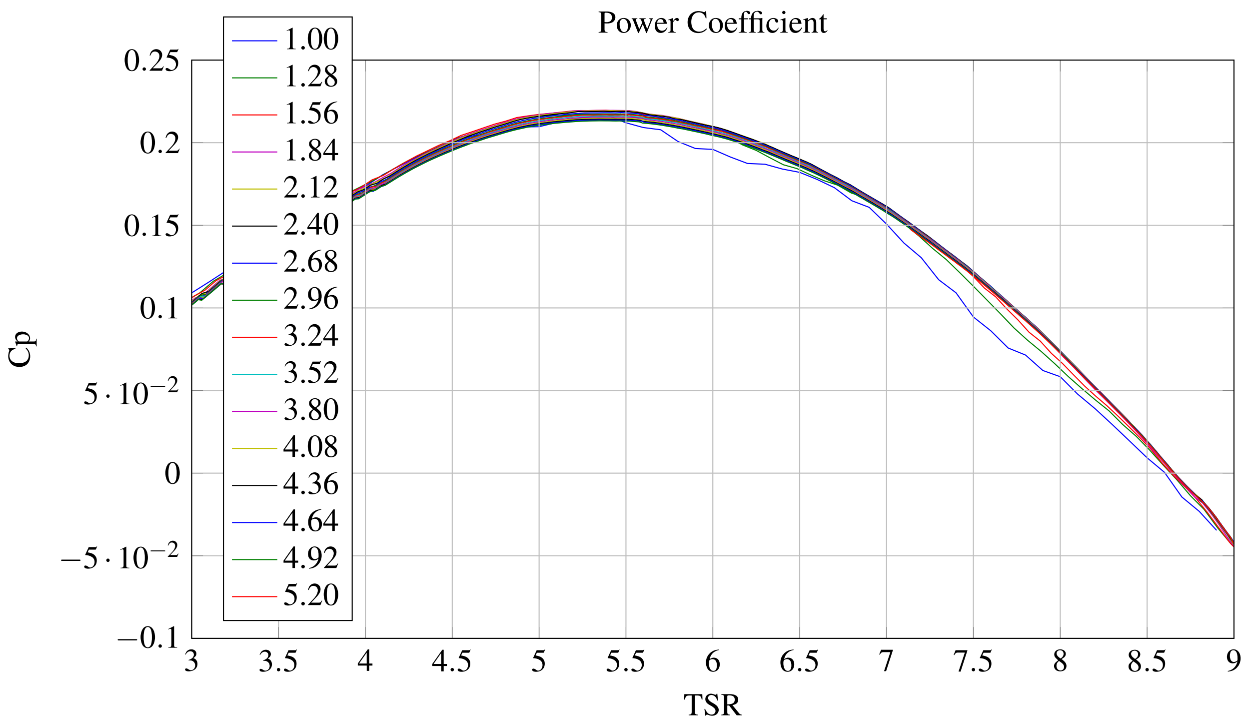

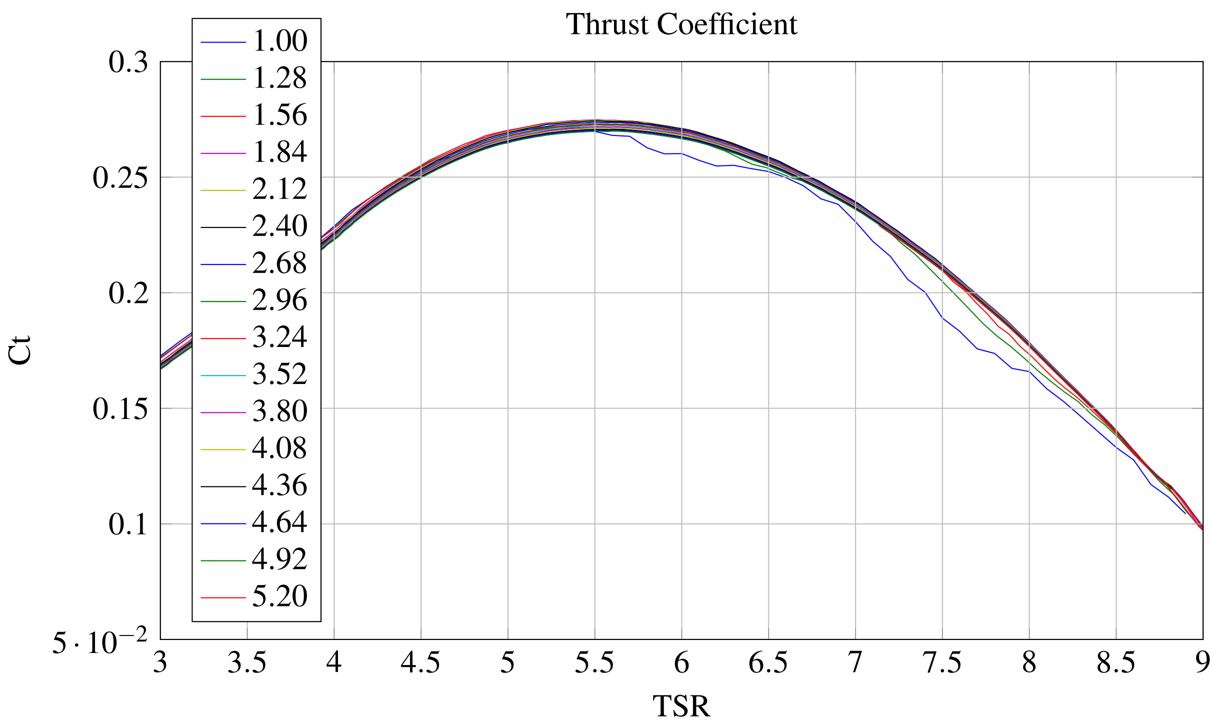

Fig. 9.5 Power and Thrust Characteristics dependency on mesh refinement. Base case presents $40x20x40$ cells. In the legend the refinement level for each simulation is indicated

keeping it equal to 2 and refining and coarsening the mesh consequently. The data show a relevant variation: the larger ε is, the more power the turbine produces and thrust is exerted by the flow. Intuitively the device is so capable of causing a larger blockage in the flow.

Time Stepping Finally the influence of time stepping is investigated. Very little spread is visible in the data. This indicates the delta time choice will be limited by the LES simulation Courant Number limit rather than stability and accuracy of the turbine code. Some early studies conducted by the author making use of the [18] library showed unstable behaviour requiring the Courant Number to be lower than a percent. The improvement is due to the fact the author's model uses the embedded OpenFOAM interpolation libraries rather than linear interpolation of the velocity between the surrounding closest couple of mesh cells.

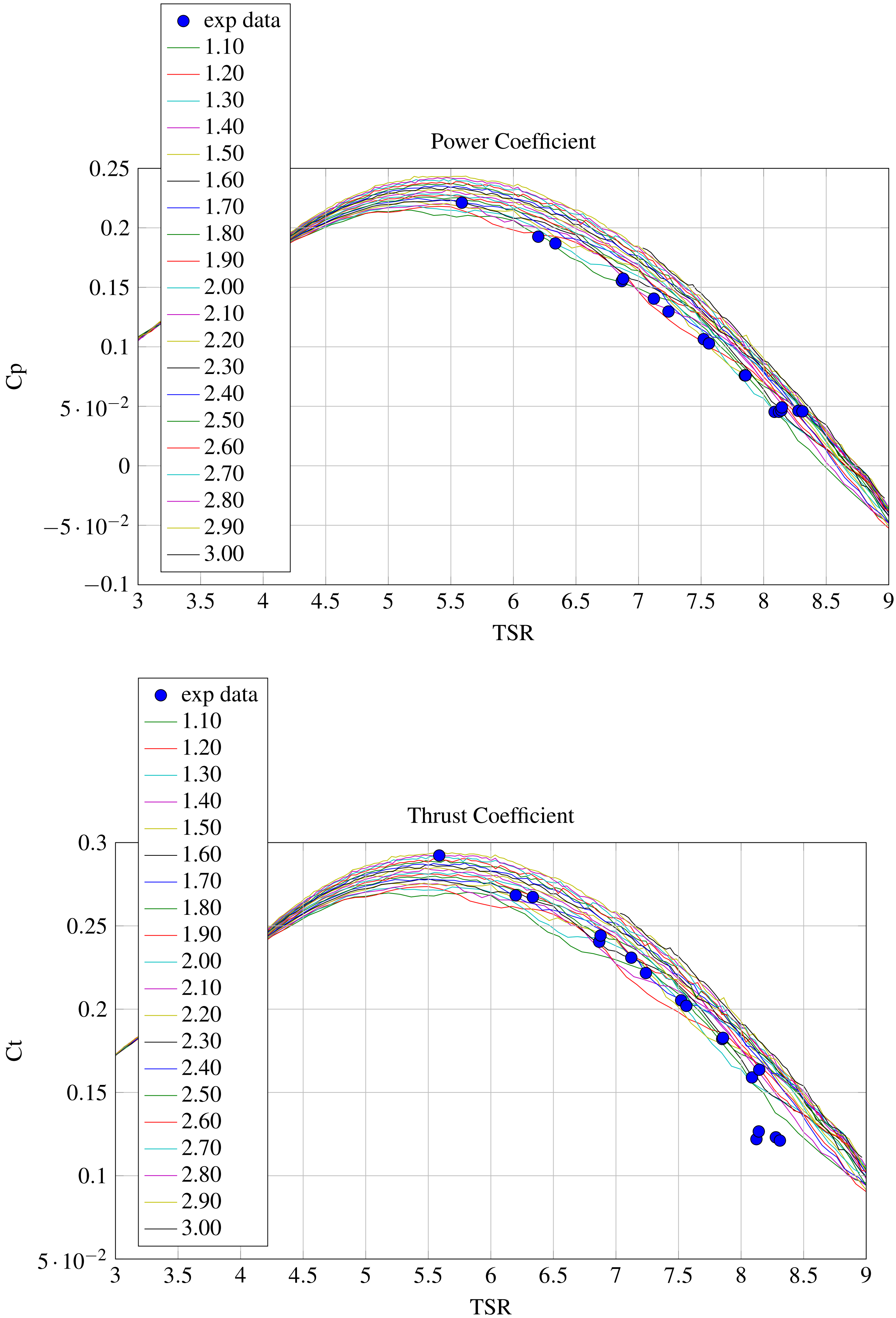

Fig. 9.6 Power and Thrust Characteristics dependency on epsilon force spread parameter.

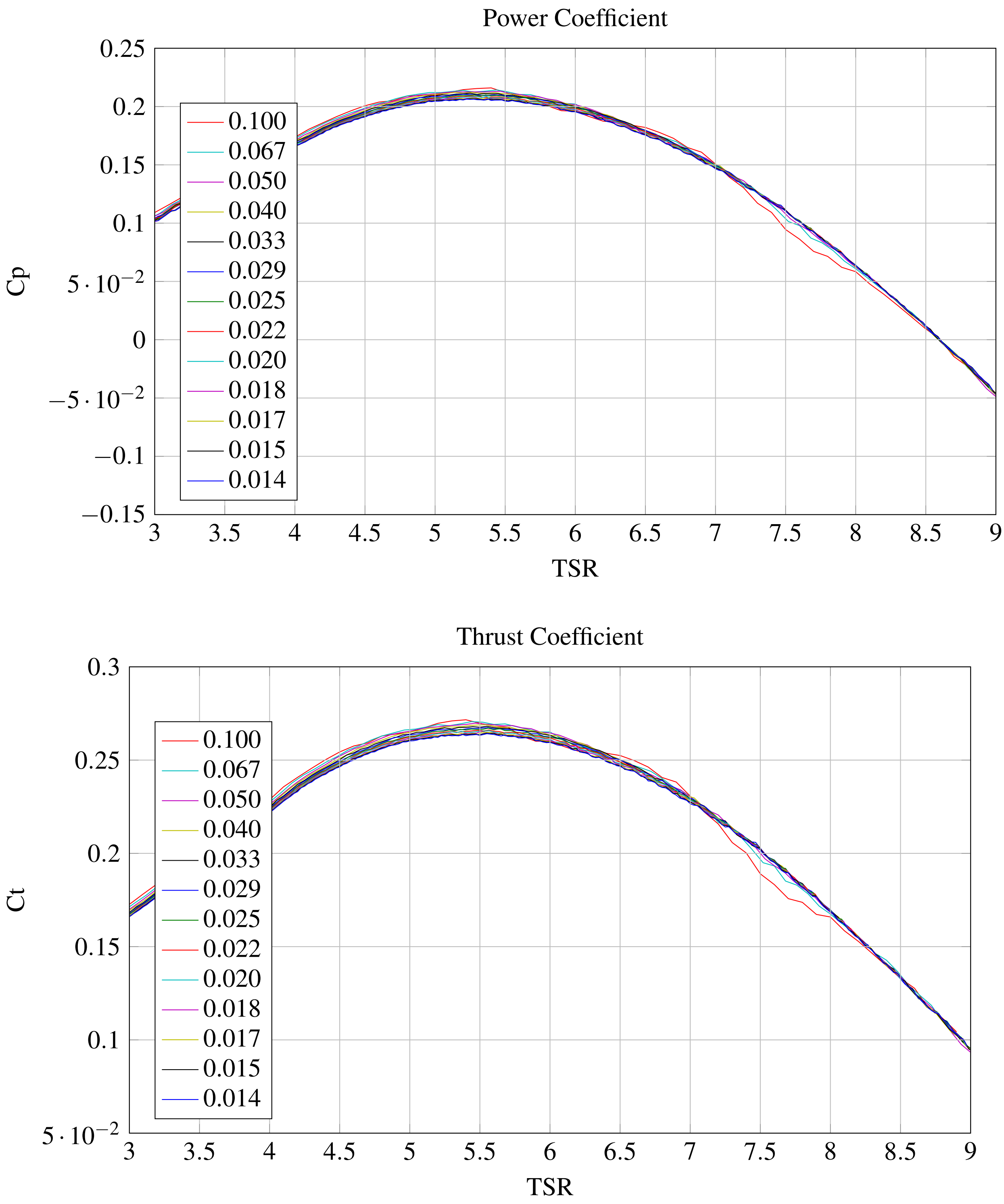

Fig. 9.7 Power and Thrust Characteristics dependency on time step length.

Conclusions In the previous paragraphs the author showed the dependency of performance on a number of model setup parameters. This was required in order to gain sensitivity on the model response to parameter changes and to select the appropriate values that will be used in Section 10.2.
Caution was then applied positioning the inlet a 1 rotor distance upstream the turbine. The mesh refinement level is so that the mesh presents more than 10 cells across a blade span. The blockage is in reality dependent on the actual position of the turbine. The base case 0.0 proved to be sufficient for the turbine tabulated data tuning presented in the next section. Furthermore the author experience that time stepping for turbulent resolved simulations is actually limited by the solution of turbulence itself rather than accuracy of the actuator line model. One last comment should be done on the setting of the ε parameter: in order to represent the actual area of influence of the blade on the field it should be the same size as the local aerofoil section chord. In general though this is not possible due to the coarseness of the mesh, it was than set by the author to be equal to twice the mesh size.

9.2 Turbine Tabulated Data Tuning

NREL S809 aerofoil data is easily available at different Reynolds numbers and turbulent conditions for example in the NREL portal [1]. The author has found difficulties in matching the experimental data from the water tank plugging the available data in literature [66] into the actuator line numerical model. The reason is that the particular tank turbulent conditions and velocity profile alongside with a turbine blade shape not certified by post-production scanning, might cause slight changes that combined together can cause an error as large as 50% (Figure 9.7).
Hence the decision to take power and thrust coefficients curves from the experiments and tune the aerofoil lift and drag coefficients in order to match the experimental performance. This is common practice in CFD and FEA. The aerofoil description has been implemented according to equations resumed in [62]. A norm function has been used in order to evaluated the distance between the experimental results cloud and the simulation output characteristics. Its minimum has been computed by search via the Nelder-Mead method running a number of simulations varying the lift-and-drag-describing aerofoil parameters.
In the following sections more detail is provided:

- in Section 9.2.1 a description of the lift and drag coefficients curves model is reported,

- Section 9.2.2 gives an introduction on the Nelder-Mead minimisation method,
- finally in Section 9.2.3 presents the algorithm used for the coefficients tuning procedure, base case simulation and obtained results

9.2.1 Aerofoil Lift and Drag Curves Description

Aerofoil lift and drag coefficient curves can be described in the pre-stall range as reported below:

$$C_L = S \cdot (\alpha - A_0) - sign(\alpha - A_0) \cdot R_{C_L} \cdot \left(\frac{|\alpha - A_0|}{A_{C_{Lmax}} - A_0} \right)^N \tag{9.1}$$

$$C_D = C_{D0} + (C_{D_{max}} - C_{D0}) \cdot \left(\frac{\alpha - A_0}{A_{C_{Dmax}} - A_0} \right)^M \tag{9.2}$$

where

α is the angle of attack,

S the slope of the linear part of lift,

A_0 the angle of attack for lift equal to zero,

R_{C_L} reduction from linear segment of lift curve,

$A_{C_{Lmax}}$ the angle of attack at max pre-stall lift,

N the exponent of lift curve for its shape definition at $\alpha = A_{C_Lmax}$,

$A_{C_{Dmax}}$ the angle of attack at max pre-stall drag,

$C_{D_{max}}$ max pre-stall drag,

M the exponent of drag curve.

The drag coefficient curve 9.2 is a symmetric exponential function centred in A_0. The lift coefficient curve 9.1 is the sum of a linear component, prevalent around A_0, and a non linear part taking into account the departure from linearity close to stall.
In [62] the equations parameters are tuned to obtain power and lift curves closely matched for the well known NREL Phase VI experiment [29]. Being the tidal turbine model in the current study a scaled version of the Phase VI experiment, the author utilised the available data in [62] as starting point for the model adjustment.

In [62] particular attention is paid to the post-stall regime. Here the analysis is limited to the pre-stall range: the interest is in the turbine regulation away from stall. The unsteady loading consequence of this phenomenon is detrimental for the machine fatigue life, hence control operation is designed to be distant from it.
BEM models in general and the actuator line developed here in particular, require lift and drag data spanning 360°. A widely used method is the so-called Viterna [72] extrapolation consisting in the following equation for the drag coefficient

$$C_{D_{max}} = 1.11 + 0.018AR \qquad \alpha = 90^\circ \tag{9.3}$$

$$C_D = B_1 \sin^2\alpha + B_2 \cos\alpha \qquad 15^\circ < \alpha < 90^\circ \tag{9.4}$$

where:

$$B_1 = C_{D_{max}}$$

$$B_2 = \frac{C_{D_{stall}} \cos\alpha_{stall}}{\cos\alpha_{stall}}$$

and for the lift coefficient

$$C_L = A_1 \sin 2\alpha + A_2 \frac{\cos^2\alpha}{\sin\alpha} \qquad 15^\circ < \alpha < 90^\circ \tag{9.5}$$

where:

$$A_1 = B_1/2$$

$$A_2 = (C_{L_{stall}} - C_{D_{max}} \sin\alpha_{stall} \cos\alpha_{stall}) \frac{\sin\alpha_{stall}}{\cos^2\alpha_{stall}}$$

9.2.2 Minimisation Nelder-Mead Procedure

The Nelder–Mead method [58] is a heuristic technique used to minimise an objective function without knowledge of its derivatives.
This method aims to find the optimum by using a set of points $\mathbf{x} \in \mathbb{R}^n$ representing the input parameters of the function to be minimised $f(\mathbf{x})$ and reflecting the worst one over the others centroid. If the operation produces a point closer to the solution then the worst the operation is repeated. If the point is the best found a further expansion in the direction is tried. In case the point isn't better, conversely a contraction is applied. If all the above don't produce any improvement then the point cloud is positioned across a valley and a shrinkage towards the

best point available is conducted.
The mentioned procedure can be described step by step as follows:

1. a set of initial conditions is provided $\mathbf{x}_1, \ldots, \mathbf{x}_{n+1}$
2. function is evaluated and ordered at the provided points $f(\mathbf{x}_1) \leq f(\mathbf{x}_2) \leq \cdots \leq f(\mathbf{x}_{n+1})$.
3. the centroid of the first n points $\mathbf{x}_o = \dfrac{\mathbf{x}_1 + \mathbf{x}_2 + \cdots + \mathbf{x}_n}{n}$
4. a new point $\mathbf{x}_r = \mathbf{x}_o + \alpha(\mathbf{x}_o - \mathbf{x}_{n+1})$ with $\alpha > 0$ called **reflection** is computed
   - If $f(\mathbf{x}_1) \leq f(\mathbf{x}_r) < f(\mathbf{x}_n)$ then $\mathbf{x}_{n+1}$ is replaced with $\mathbf{x}_r$ and the procedure starts over from 2
   - else if reflected point results the best $f(\mathbf{x}_r) < f(\mathbf{x}_1)$, then an **expansion** point $\mathbf{x}_e = \mathbf{x}_o + \gamma(\mathbf{x}_r - \mathbf{x}_o)$ with $\gamma > 0$ is computed.
     (a) if $f(\mathbf{x}_e) < f(\mathbf{x}_r)$ then $\mathbf{x}_{n+1} = \mathbf{x}_e$ and back to 2
     (b) else $\mathbf{x}_{n+1} = \mathbf{x}_r$ and return to 2
   - else continue
5. either **contraction** or **shrink**. Contracted point $\mathbf{x}_c = \mathbf{x}_o + \rho(\mathbf{x}_{n+1} - \mathbf{x}_o)$ with $0 < \rho \leq 0.5$
   - if $f(\mathbf{x}_c) < f(\mathbf{x}_{n+1})$ then execute contraction $\mathbf{x}_{n+1} = \mathbf{x}_e$ and return to 2
   - else shrink substituting $\mathbf{x}_i = \mathbf{x}_1 + \sigma(\mathbf{x}_i - \mathbf{x}_1)$ for i $\in \{2, \ldots, n+1\}$ and go back to step 2.

The coefficients in Greek letters are named as below

- α reflection,
- γ expansion,
- ρ contraction,
- σ shrink.

In this work the value assigned have been kept as standard

$$\begin{pmatrix} \alpha \\ \gamma \\ \rho \\ \sigma \end{pmatrix} = \begin{pmatrix} 1 \\ 2 \\ 1/2 \\ 1/2 \end{pmatrix}$$

.

Parameter	S	A_0	R_{C_L}	$A_{C_{Lmax}}$	N	$A_{C_{Dmax}}$	$C_{D_{max}}$	M
Initial Guess	0.125	-1.0	1.033	15.7	2.01	21.8	0.226	3.0
Optimised	0.074	-0.28	0.553	15.7	2.93	21.8	0.226	3.0

Table 9.1 Aerofoil performance description coefficients, initial guess and optimised.

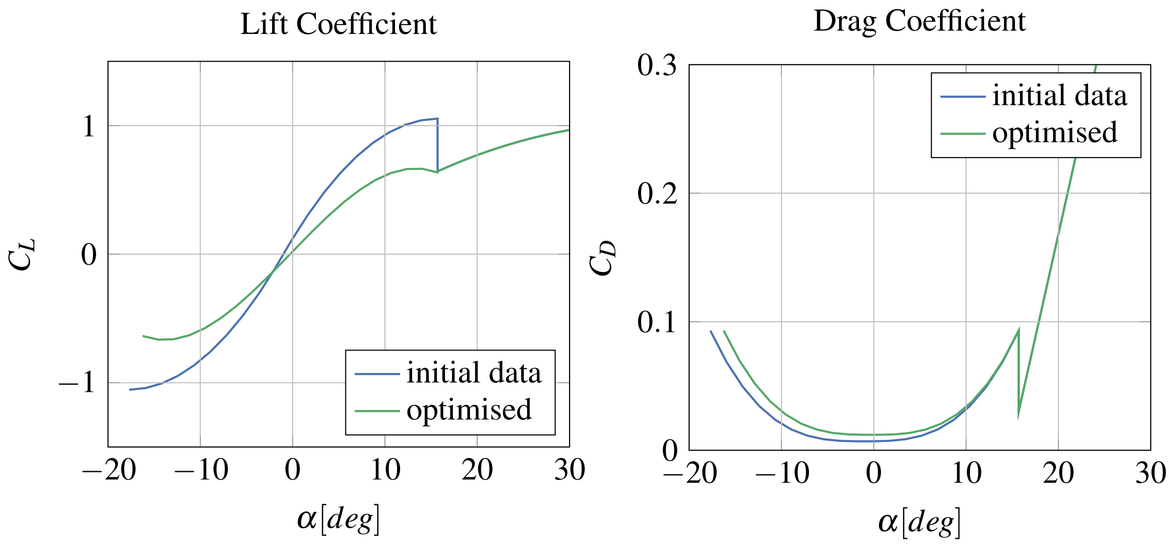

Fig. 9.8 Initial and after Tuning Lift and Drag coefficients

9.2.3 Implementation and Validation Results

The parameters optimisation procedure has been carried out making use of the *scipy.optimize* [4] library in conjunction with *pyfoam* [3] in order to run a large number of OpenFOAM simulations.

The scope function to be minimised is defined as the $L-2$ norm of the vector difference between the simulation output performance curves and the experimental points. Values of power and thrust coefficients from the numerical simulation are derived interpolating the obtained performance curves at the experimental collected values of Tip Speed Ratio.

The initial guess for the aerofoil parameters come from matching the experimental data in [66]. From Picture 9.8 and Table 9.1 one can see that when compared with data validate for performance of a 10m full-scale wind turbine BEM calculation, stall occurs earlier and it is less abrupt. This is an expected behaviour when the Reynolds number results one order of magnitude lower. Also drag coefficient at close-to-zero lift shows higher values in magnitude. The post-stall behaviour was kept constant being irrelevant in this investigation.

Velocities in the [29] are of the order of magnitude of 10m/s. Turbine *Re* is than equal to $\frac{l \cdot v}{\nu} \simeq \frac{10m \cdot 10m/s}{10^{-5}m/s^2} = 10^7$. The $1m$ tidal turbine model object of the present work operates in water in a velocity field of $1m/s$ hence $Re \simeq \frac{1m \cdot 1m/s}{10^{-6}m/s^2} = 10^6$.

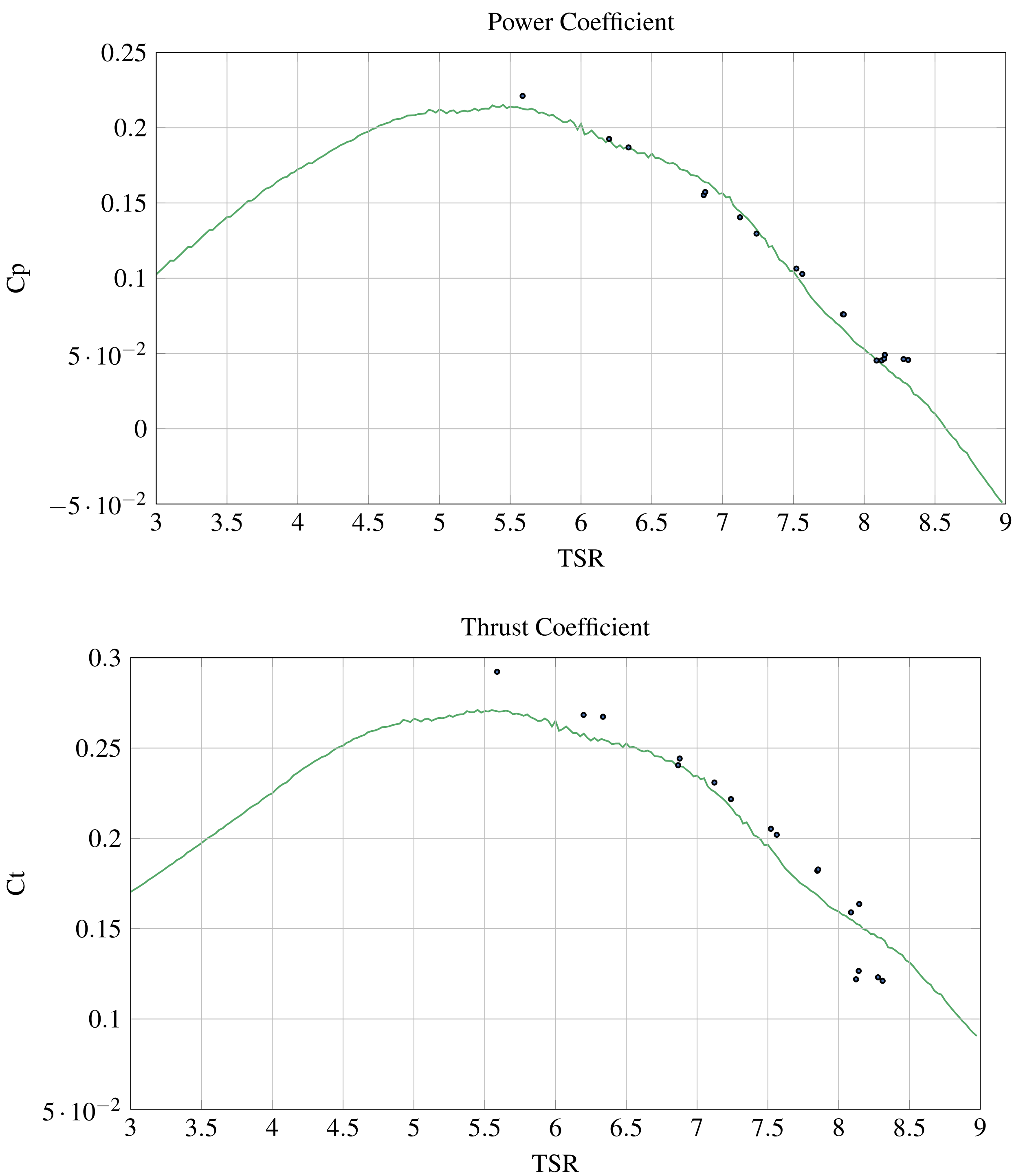

Fig. 9.9 Power and Thrust Characteristics from Tuned aerofoil coefficients vs. experimental points from IFREMER campaign

Chapter 10

Numerical Results

10.1 Flow Simulations Results

In the present section four methodologies implemented by the author in OpenFOAM are compared in the production of realistic turbulence in a channel flow. Both the “vortons ” and the “Smirnov” methods are described in Part I. The FFT-POD approach is described in the numerical methodologies part. Additionally, already in the standard OpenFOAM libraries a random field generator respecting:

- amplitude of fluctuation
- a bland time correlation by introduction of a relaxation factor: each time step is blended to the previous given a relaxation coefficient from 0, uncorrelated to 1, fully correlated.

All the inflow methods were set to reproduce the same integral length and time scales and Reynolds stresses. In picture 10.1 the inlet patch at an arbitrary time step for the Reference simulation alongside the methods trying to match it are reported. In figure 10.2d the downstream-the-inlet-patch evolution is visible from right to left. The random inflow is as expected the worse performing. The space non correlation causes high velocity streaks to be convected downstream. A channel like behaviour is never recovered downstream the domain considered.
The Smirnov method performs well on the inlet patch in terms of reproducing coherent structures even though the effect of the stretching of the homogeneous starting field makes the field close to the wall boundary unrealistically stretched in the direction of the wall itself. Unfortunately downstream evolution is not currently available.
The vortons method result limited by the number of vertices present on the inlet patch but

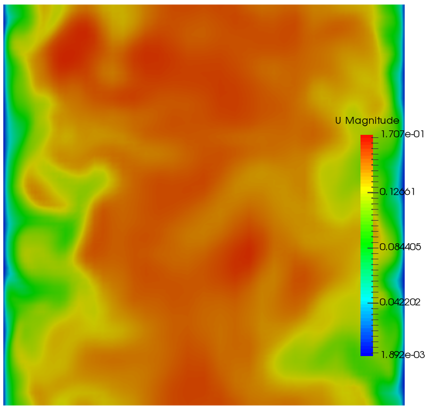

(a) Reference simulation

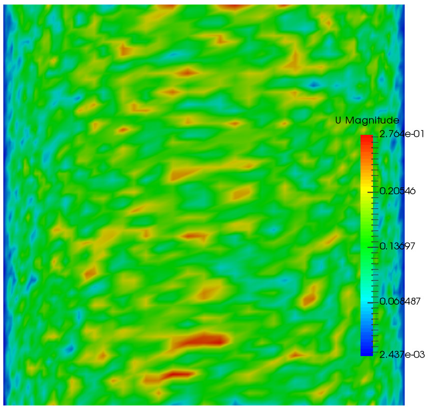

(b) Random Inflow

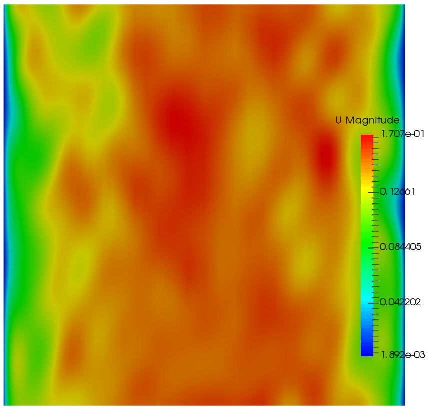

(c) Smirnov Inflow

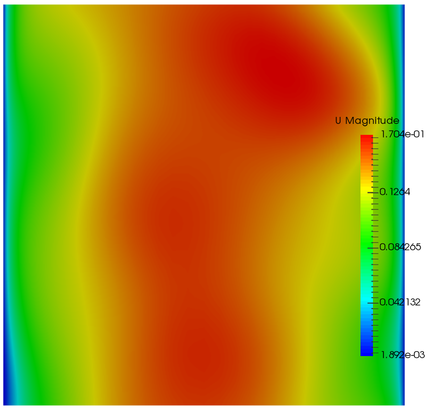

(d) Vortons Inflo

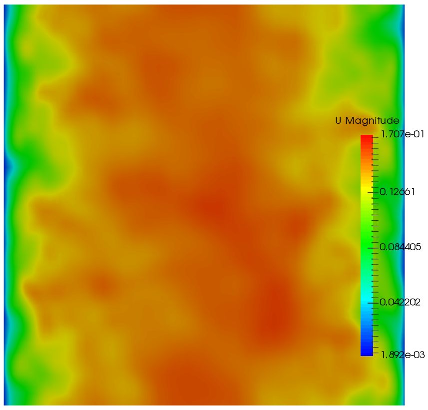

(e) FFT-POD Inflow

Fig. 10.1 Comparison between implemented inflow methods in reproducing a channel flow. Cross-span-wise section

those seem to decay towards the end of the domain to more developed turbulence.
The author's new method well represent all the features of the original flow. Also downstream evolution is much similar to that of the reference channel simulation. The lack of the full power is a consequence of the truncation of the expansion series to the 100th coefficient. The illustrated partial result shows anyway the potential of the developed methodology when compared with the current state of art.

Additional statistical analyses would be required in order to compare the presented implemented methodologies in OpenFOAM such as:

- mean flow profiles and their evolution downstream the inlet section
- mean Reynolds stresses (as in Figure5.6b, 5.4b, 5.3b and 5.1a)
- the turbulence spectrum (Figures 5.1b and 5.2b)
- the second invariant of the velocity gradient tensor (Q) contour plotsof in order to qualitatively describe the wall-genrated turbulent structures

Due to practical lack of time the author has not been able to prepare the mentioned material. Furthermore the performance of the single point method described in Section 7.1.1 has not been assessed.

10.2 Turbine Simulations Results

In the present section the three state of the art methods described have been used to generate turbulent statistics for the turbine model implemented by the author. The turbine was positioned half the channel height downstream the inlet patch ingesting a flow very similar to that present in the inlet patch.
The flow results are in accordance with those of the previous session. The random generator produces a white noise signature in both torque and power being unsuitable for dynamic calculations.
Both the Vortons and Smirnov methods present peculiar spectral shapes that cannot be modified. This could be in some cases acceptable but not in general. The three spectral responses unequivocally show the *fundamental importance of the inflow generator in the assessment of unsteady loads on open rotor turbines*.
Also for this section additional work would be required to run also simulations having as inflow conditions:

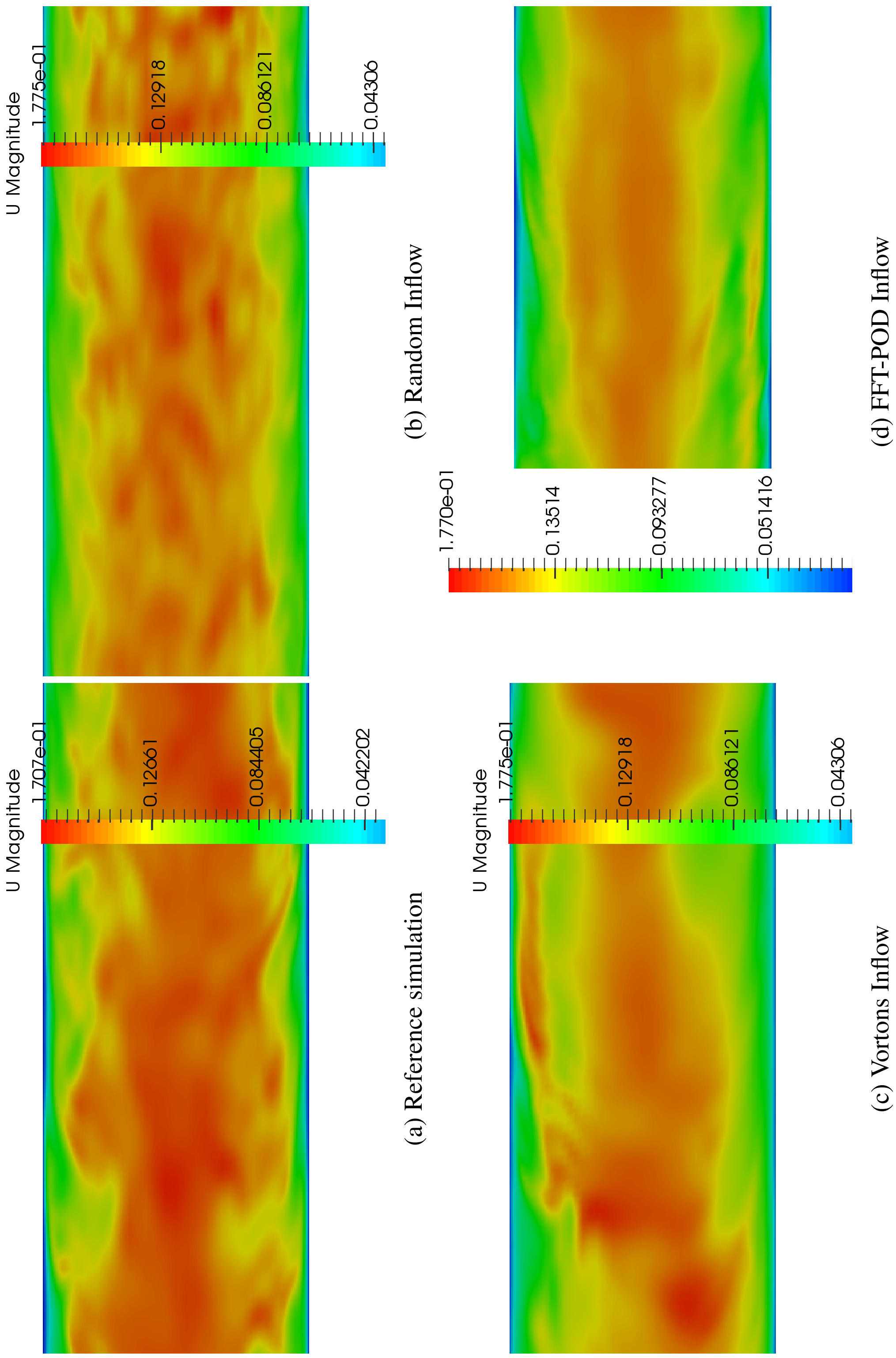

(a) Reference simulation

(b) Random Inflow

(c) Vortons Inflow

(d) FFT-POD Inflow

Fig. 10.2 Comparison between implemented inflow methods in reproducing a channel flow. Stream-wise section

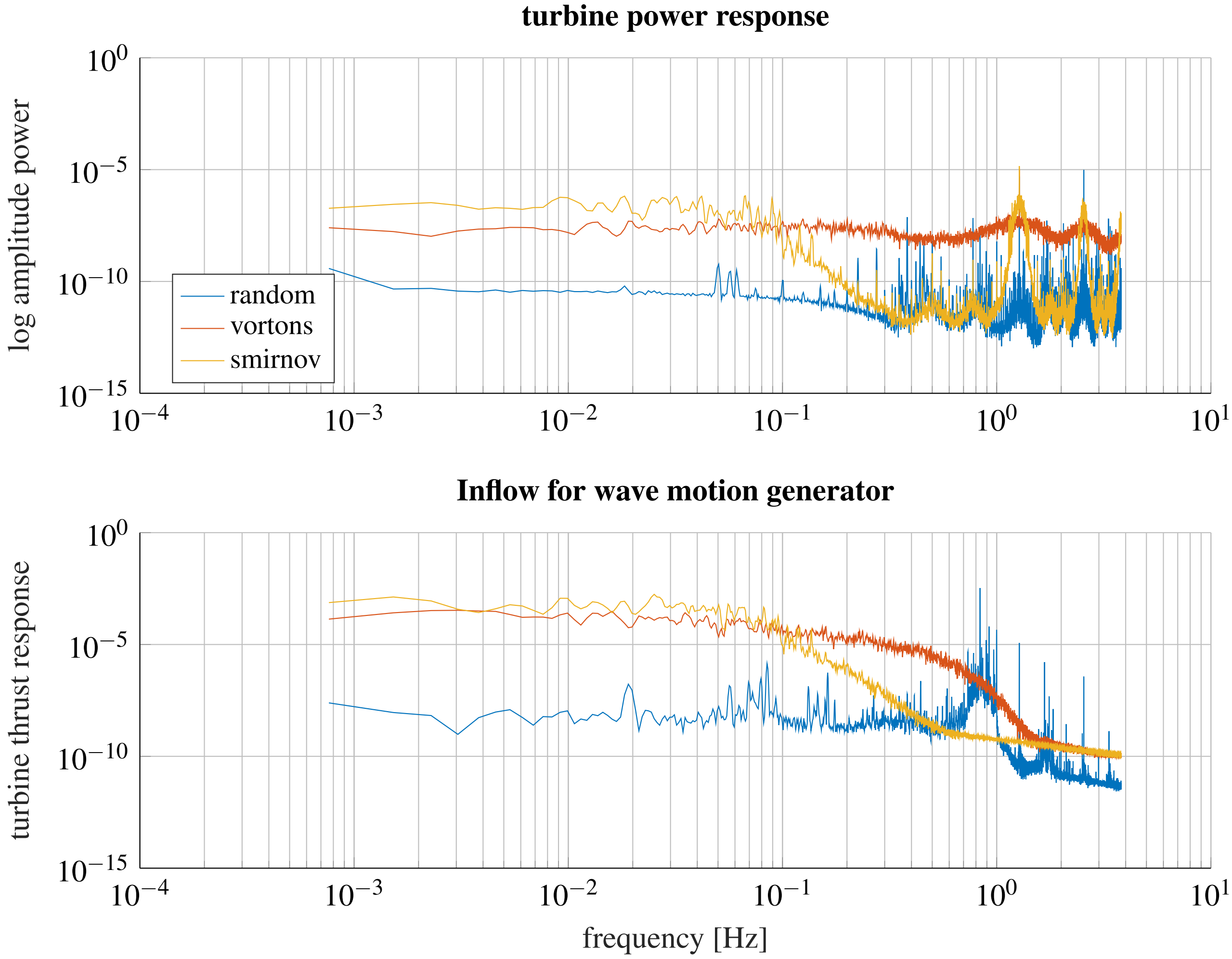

Fig. 10.3 Turbine dynamic Power and Thrust Response for channel case making use of some of the implemented methods

- the reference flow
- the author's developed single point method (Section 7.1.1) and Y direction POD Method (Section 7.1.2)

Also these additional studies have been left out by the author due to time shortage.

Chapter 11

Conclusions and Future Work

11.1 Conclusions

Main key achievements:

- analysed ADCP data from Ramsey Sound showing:
  - turbulence POD modes recover homogeneity in an efficient fashion after just 7 descriptors. Thus it is possible to use few POD modes in combination with standard harmonic functions in order to describe the turbulent structures and spacial correlation in a very large Reynolds number environmental flow.
  - POD coefficients power spectral density show similar-to-regular-velocity PSD features such as peaks and decay rate. They only contain time information being the spacial one intrinsic of the modes shape.
- conducted experimental campaign and demonstrated:
  - correlation between inflow turbulence and torque and thrust signature by activation of wave generator as a mean of producing controlled flow frequencies
  - a constant torque controller would mitigate the fatigue effects on a tidal turbine by lowering fluctuations an spectral content of torque and thrust at the shaft. This was simulated by the use of a direct-drive power system able of keeping the turbine brake torque constant.
- presented a novel inflow turbulence generation method making use of Fast Fourier Transform in the directions of homogeneity and POD analysis covering the remaining. The latter was applied to the case of a turbulent channel and

  - showed the capability of reproducing typical flow structures with a minimal computational effort.
  - turbulence statistics have not been presented in this work due to time shortage

- developed from scratch an Actuator Line Method making use of the appropriate available classes in the OpenFOAM toolbox.

- finally the inflow methods implemented alongside the newly developed one where used to produce inflow data for the ALM turbine.

  - The importance of the accuracy of the former in the assessment of dynamic loads on the latter has been clearly stated.
  - The novel method presented resulted the most promising. Its accuracy has to be further assessed.

11.2 Future Work

Quantitative studies on the turbulence generated by the developed “Y direction POD“ method and a dynamic validation of the implemented ALM method in OpenFOAM vs the IFREMER experiment making use of the ”Single Point“ method for the inflow, are still open points of this work.
Furthermore this work leaves open a number possibilities for additional studies.
One possible point is the application of the POD methodology developed for the inflow generation making use of the data from a sea site such as Ramsey Sound. This would require to find a way to extend line data coming from ADCPs to surface data to be used to characterise a boundary inflow in a 3-d simulation.
A relatively straightforward extension study could be the evaluation of the turbulence generated by closely spaced devices in a farm or for the DeltaStream three-rotors concept case. Extension to closed rotor turbines studies such as aeronautic compressors where the turbulent, possibly consequence of an upstream stall, flow from an experiment could be used to study the downstream stage aerodynamic effects on the blades cascade.
The described FFT methodology can be re-adapted to anular geometries when replacing the Fourier system being othonormal complete in a rectangular geometry with the Bessel one for circular domains. In general the inflow boundary conditions generation problem requires further investigation. Appropriate production of correlated turbulent structures would be an

enabling tool for turbulence resolved simulation to replace RANS for all those studies where the dynamic effects are of crucial importance.

References

[1] Airfoil Data. https://wind.nrel.gov/airfoils/AirfoilData.html.

[LEM] LEMOS. https://github.com/LEMOS-Rostock.

[3] PyFOAM. https://pypi.python.org/pypi/PyFoam.

[4] Scipy optimize. https://docs.scipy.org/doc/scipy/reference/tutorial/optimize.html.

[5] (2014). OpenFOAM v2.3.1. https://openfoam.org/.

[6] Adrian, R., Meneveau, C., Moser, R., and Riley, J. (2000). Final report on turbulence measurements for les workshop. Technical report, DTIC Document.

[7] Afgan, I., McNaughton, J., Rolfo, S., Apsley, D., Stallard, T., and Stansby, P. (2013). Turbulent flow and loading on a tidal stream turbine by les and rans. *International Journal of Heat and Fluid Flow*, 43:96 – 108. 7th International Symposium on Turbulence Heat Mass Transfer (THMT-7), Palermo Conference on Modelling Fluid Flow (CMFF'12).

[8] Andreucci, D. (2016). *Appunti del corso di Fisica Matematica*. La Sapienza, Facoltá di Ingegneria.

[9] Barltrop, N., Varyani, K., Grant, A., Clelland, D., and Pham, X. (2007). Investigation into wave—current interactions in marine current turbines. *Proceedings of the Institution of Mechanical Engineers, Part A: Journal of Power and Energy*, 221(2):233–242.

[10] Ben Elghali, S., Benbouzid, M., and Charpentier, J. (2007). Marine tidal current electric power generation technology: State of the art and current status. In *Electric Machines Drives Conference, 2007. IEMDC '07. IEEE International*, volume 2, pages 1407 –1412.

[11] Benowitz, B. A. and Deodatis, G. (2015). Simulation of wind velocities on long span structures: A novel stochastic wave based model. *Journal of Wind Engineering and Industrial Aerodynamics*, 147:154–163.

[12] Berkooz, G., Holmes, P., and ey, J. L. (1993a). The proper orthogonal decomposition in the analysis of turbulent flows. *Annual review of fluid mechanics*, 25(1):539–575.

[13] Berkooz, G., Holmes, P., and Lumley, J. (1993b). On the relation between low-dimensional models and the dynamics of coherent structures in the turbulent wall layer. *Theoretical and Computational Fluid Dynamics*, 4(6):255–269.

[14] Bijleveld, H. and Veldman, A. (2010). Rotorflow: A quasi-simultaneous interaction method for the prediction of three-dimensional aerodynamic flow over wind turbine blades. *The Science of Making Torque from Wind, Heraklion, Crete, Greece, 28-30 juni 2010.*

[15] C., S. W. and Masson, C. (2010). Modeling of lifting-device aerodynamics using the actuator surface concept. *Int. J. Numer. Meth. Fluids*, (62):1264–1298.

[16] Canuto, C., Hussaini, M., Quarteroni, A., and Zang, T. (2007). *Spectral Methods: Evolution to Complex Geometries and Applications to Fluid Dynamics*. Scientific Computation. Springer Berlin Heidelberg.

[17] Castro, H. G. and Paz, R. R. (2013). A time and space correlated turbulence synthesis method for large eddy simulations. *Journal of Computational Physics*, 235:742 – 763.

[18] Churchfield, M. and Lee, S. (2012.). Nwtc design codes sowfa.

[19] Churchfield, M. J., Lee, S., Michalakes, J., and Moriarty, P. J. (2012a). A numerical study of the effects of atmospheric and wake turbulence on wind turbine dynamics. *Journal of Turbulence*, page N14.

[20] Churchfield, M. J., Li, Y., and Moriarty, P. J. (2012b). A large-eddy simulation study of wake propagation and power production in an array of tidal- current turbines - preprint. *To be published in Philosophical Transactions of the Royal Society*.

[Comte-Bellot] Comte-Bellot, G. High reynolds number channel flow experiment.

[22] Corsar, M. (2012). Turbulent loads upon tidal turbines: Comparison between experiment and modeling predictions. *Asian Wave and Tidal Conference Series*.

[23] Dobrev, I., Massouh, F., and Rapin, M. (2007). Actuator surface hybrid model. *Journal of Physics*, Conference Series(75).

[24] Druault, P., Lardeau, S., Bonnet, J.-P., Coiffet, F., Delville, J., Lamballais, E., Largeau, J.-F., and Perret, L. (2004). Generation of three-dimensional turbulent inlet conditions for large-eddy simulation. *AIAA journal*, 42(3):447–456.

[25] Ferziger, J. H. and Peric, M. (2012). *Computational methods for fluid dynamics*. Springer Science & Business Media.

[26] Frederich, O. and Luchtenburg, D. M. (2011). Modal analysis of complex turbulent flow. In *TSFP DIGITAL LIBRARY ONLINE*. Begel House Inc.

[27] Galloway, P., Myers, L., and Bahaj, A. (2010). Studies of a scale tidal turbine in close proximity to waves.

[28] Hand, M., Simms, D., Fingersh, L., Jager, D., Cotrell, J., Schreck, S., and Larwood, S. (2001a). Unsteady aerodynamics experiment phase vi: wind tunnel test configurations and available data campaigns. *National Renewable Energy Laboratory, Golden, CO, Report No. NREL/TP-500-29955*.

[29] Hand, M., Simms, D., Fingersh, L., Jager, D., Cotrell, J., Schreck, S., and Larwood, S. (2001b). Unsteady aerodynamics experiment phase vi: wind tunnel test configurations and available data campaigns. *National Renewable Energy Laboratory, Golden, CO, Report No. NREL/TP-500-29955*.

[30] Hansen, M. O. L. (2008). *Aerodynamics of Wind Turbines*. earthscan, second edition.

[31] Holmes, P., Lumley, J. L., and Berkooz, G. (1998). *Turbulence, coherent structures, dynamical systems and symmetry*. Cambridge university press.

[32] Huang, S., Li, Q., and Wu, J. (2010). A general inflow turbulence generator for large eddy simulation. *Journal of Wind Engineering and Industrial Aerodynamics*, 98(10–11):600–617.

[33] Hœpffner, J., Naka, Y., and Fukagata, K. (2011). Realizing turbulent statistics. *Journal of Fluid Mechanics*, 676:54–80.

[34] JN, S. (1995). A model for unsteady rotor aerodynamics. *J. Wind Eng. Ind. Aerodyn.*, 58:259.

[35] JOHN KIM, P. M. and MOSER, R. (1987). Turbulence statistics in fully developed channel flow at low reynolds number. *J . Fluid Mech.*

[36] Kaltenbach, H.-J., Fatica, M., Mittal, R., Lund, T. S., and Moin, P. (1999). Study of flow in a planar asymmetric diffuser using large-eddy simulation. *Journal of Fluid Mechanics*, 390:151–185.

[37] Keating, A., Piomelli, U., Balaras, E., and Kaltenbach, H.-J. (2004). A priori and a posteriori tests of inflow conditions for large-eddy simulation. *Physics of Fluids*, 16(12):4696–4712.

[38] Kolmogorov, A. N. (1941). The local structure of turbulence in incompressible viscous fluid for very large reynolds numbers. In *Dokl. Akad. Nauk SSSR*, volume 30, pages 301–305. JSTOR.

[39] Kornev, N. and Hassel, E. (2007). Synthesis of homogeneous anisotropic divergence-free turbulent fields with prescribed second-order statistics by vortex dipoles. *Physics of Fluids*, 19(6):–.

[40] Kraichnan, R. H. (1970). Diffusion by a random velocity field. *Physics of Fluids*, 13(1):22–31.

[41] LeGresley, P. A. (2005). *Application of proper orthogonal decomposition (POD) to design decomposition methods*. PhD thesis, Stanford University.

[42] Li, N., Balaras, E., and Piomelli, U. (2000). Inflow conditions for large-eddy simulations of mixing layers. *Physics of Fluids*, 12(4):935–938.

[43] Li, S. and Montgomery, D. (1996). Decaying two-dimensional turbulence with rigid walls. *Physics Letters A*, 218(3):281 – 291.

[44] Liu, P. (2010). A computational hydrodynamics method for horizontal axis turbine – panel method modeling migration from propulsion to turbine energy. *Energy*, 35(7):2843–2851.

[45] Lozano-Durán, A. and Jiménez, J. (2014). Time-resolved evolution of coherent structures in turbulent channels: characterization of eddies and cascades. *Journal of Fluid Mechanics*, 759:432–471.

[46] Lumley, J. L. (1970). Stochastic tools in turbulence. volume 12. applied mathematics and mechanics. Technical report, DTIC Document.

[47] Lund, T. S., Wu, X., and Squires, K. D. (1998). Generation of turbulent inflow data for spatially-developing boundary layer simulations. *Journal of Computational Physics*, 140(2):233–258.

[48] Luznik, L., Flack, K. A., Lust, E. E., and Taylor, K. (2013). The effect of surface waves on the performance characteristics of a model tidal turbine. *Renewable energy*, 58:108–114.

[MathWorks] MathWorks. Matlab armax method.

[50] McCann, G. (2007). Tidal current turbine fatigue loading sensitivity to waves and turbulence–a parametric study. In *Proceedings of the 7th European Wave and Tidal Energy Conference*.

[51] Mikkelsen, R. (2003). *Actuator disc methods applied to wind turbines*. PhD thesis, PhD thesis, Technical University of Denmark.

[52] Moriarty, P. and Hassen, A. (2005). *AeroDyn Theory Manual*. NREL.

[53] Pope, S. B. (2000). *Turbulent Flows*. Cambridge University Press.

[54] Said, S. E. and Dickey, D. A. (1984). Testing for unit roots in autoregressive-moving average models of unknown order. *Biometrika*, 71(3):599–607.

[55] Sanderse, B. (2009). Aerodynamics of wind turbine wakes.

[56] Shinozuka, M. and Deodatis, G. (1991). Simulation of stochastic processes by spectral representation. *Applied Mechanics Reviews*, 44(4):131.

[57] Shinozuka, M. and Deodatis, G. (1996). Simulation of multi-dimensional gaussian stochastic fields by spectral representation. *Applied Mechanics Reviews*, 49:29–53.

[58] Singer, S. and Nelder, J. (2009). Nelder-mead algorithm. *Scholarpedia*, 4(7):2928.

[59] Sirovich, L. (1987). Turbulence and the dynamics of coherent structures. *Quarterly of applied mathematics*, 45(3):561–571.

[60] Smirnov, A., Shi, S., and Celik, I. (2001). Random flow generation technique for large eddy simulations and particle-dynamics modeling. *Journal of Fluids Engineering*, 132(2):359–371.

[61] Sørensen, J. N. (2011). Aerodynamic aspects of wind energy conversion. *Annual Review of Fluid Mechanics*, 43(1):427–448.

[62] Spera, D. A. (2008). Models of lift and drag coefficients of stalled and unstalled airfoils in wind turbines and wind tunnels.

[63] Speziale, C. (1998). Turbulence modeling for time-dependent rans and vles: a review. *AIAA journal*, 36(2):173–184.

[64] Squire, D., Hutchins, N., Morrill-Winter, C., Schultz, M., Klewicki, J., and Marusic, I. (2017). Applicability of taylor's hypothesis in rough-and smooth-wall boundary layers. *Journal of Fluid Mechanics*, 812:398–417.

[65] Tabor, G. and Baba-Ahmadi, M. (2010). Inlet conditions for large eddy simulation: A review. *Computers and Fluids*, 39(4):553–567.

[66] Tangler, J. and Kocurek, J. D. (2005). Wind turbine post-stall airfoil performance characteristics guidelines for blade-element momentum methods. In *43rd AIAA Aerospace Sciences Meeting and Exhibit*, pages 10–13. Reno, Nevada.

[67] Tangler, J. L. (2002). The nebulous art of using wind tunnel aerofoil data for predicting rotor performance. *Wind Energy*, 5(2-3):245–257.

[68] Timoshenko, S. P. and Woinowsky-Krieger, S. (1959). *Theory of plates and shells*. McGraw-hill.

[69] Troldborg, N. (2010). Numerical simulations of wake characteristics of a wind turbine in uniform flow. *Wind Energy*, 13:86.

[70] Vermeer, L., Sørensen, J., and Crespo, A. (2003). Wind turbine wake aerodynamics. *Progress in Aerospace Sciences*, 39(6–7):467–510.

[71] Viterna, L. A. and Corrigan, R. D. (1982). Fixed pitch rotor performance of large horizontal axis wind turbines. Technical report, NASA Lewis Research Center, Cleveland, Ohio.

[72] Viterna, L. A. and Janetzke, D. C. (1982). Theoretical and experimental power from large horizontal-axis wind turbines.

[73] Wyngaard, J. and Clifford, S. (1977). Taylor's hypothesis and high–frequency turbulence spectra. *Journal of the Atmospheric Sciences*, 34(6):922–929.

[74] WZ, S. (2009). The actuator surface model: a new navier-stokes based model for rotor computations. *J. Sol. Energy Eng.*, 131:011002.

[75] Yu, R. and Bai, X.-S. (2014). A fully divergence-free method for generation of inhomogeneous and anisotropic turbulence with large spatial variation. *Journal of Computational Physics*, 256:234 – 253.

Appendix A

Numerical Schemes

A.1 PISO algorithm in OpenFOAM

The continuity equation for an incompressible flow, when density and viscosity are constant, is satisfied when pressure and velocity solve the equations A.1.

$$\nabla^2 p = -\nabla \cdot \nabla \cdot (\rho u \otimes u) \tag{A.1}$$

This equation is coupled with the momentum equation, so a method to solve both equations must be adopted. For this work a PISO algorithm has been chosen, which is an implicit pressure-correction method. The discretized equation for velocities may be written:

$$A_P^{u_i} u_{i,P}^{n+1} + \sum_l A_l^{u_i} u_{i,l}^{n+1} = Q_{u_i}^{n+1} - \left(\frac{\delta p^{n+1}}{\delta x_i} \right)_P \tag{A.2}$$

Where P refers to an arbitrary velocity node, index l denotes the neighbor points, A are the coefficients which depend on the discretization method, Q_{u_i} contains any source term such as a body force. The only way to solve this equation is an iterative algorithm. So we first find an approximate solution for u^m, where m is the counter for outer iterations:

$$u_{i,P}^{m*} = \frac{Q_{u_i}^{m-1} - \sum_l A_l^{u_i} u_{i,l}^m}{A_P^{u_i}} - \frac{1}{A_P^{u_i}} \left(\frac{\delta p^{m-1}}{\delta x_i} \right)_P \tag{A.3}$$

The first term on the right hand side will be called $\tilde{u}^{m*}_{i,P}$, so we can write:

$$u^{m*}_{i,P} = \tilde{u}^{m*}_{i,P} - \frac{1}{A^{u_i}_P}\left(\frac{\delta p^{m-1}}{\delta x_i}\right)_P \tag{A.4}$$

the corrected velocities and pressure are linked by:

$$u^{m}_{i,P} = \tilde{u}^{m*}_{i,P} - \frac{1}{A^{u_i}_P}\left(\frac{\delta p^{m}}{\delta x_i}\right)_P \tag{A.5}$$

this one should satisfy continuity equation:

$$\frac{\delta(\rho u^m_i)}{\delta x_i} = 0 \tag{A.6}$$

so, using A.5 in A.6 one obtains a discrete Poisson equation for the pressure:

$$\frac{\delta}{\delta x_i}\left[\frac{\rho}{A^{u_i}_P}\left(\frac{\delta p^m}{\delta x_i}\right)\right]_P = \left[\frac{\delta(\rho u^m_i)}{\delta x_i}\right]_P \tag{A.7}$$

After solving the Poisson equation the final velocity field at the new iteration, u^m_i, is calculated from Eq.A.7. Now the velocity field satisfies the continuity condition, but the velocity and pressure fields do not satisfy the momentum equations, so we begin another inner iteration and the process is continued until a velocity field which satisfies both momentum and continuity equation is obtained.

The way OpenFOAM solves the pressure equation with its own implementation of PISO algorithm will be shown using the code itself. Such blocks of code are found in every solver which use the PISO algorithm with minor differences (*icoFoam*, *pisoFoam*, *channelFoam*, *dnsFoam*, they all use PISO).

The algorithm explained below is repeated for each time step.

1. First the momentum equation it is solved using the old values for u and p to have an initial estimate of U which will only need a small correction to satisfy the continuity:

```
fvVectorMatrix UEqn
        (
            fvm::ddt(U)
          + fvm::div(phi, U)
- fvm::laplacian(nu, U)
        );
```

```
solve(UEqn ==  -fvc::grad(p) +g);
```

2. PISO loop starts, it is assumed that the velocities and pressure can be written as a provisional value which requires small corrections to satisfy both momentum and continuity equations.

$$u_i^m = u_i^{m*} + \sum_r^N u^r \; ; \; p^m = p^{m-1} + \sum_r^N p^r \tag{A.8}$$

The standard approach adopted in [25], is to solve the equations for each corrections. That obviously would require an extra storage in memory, so OpenFOAM solves the same equations but using the latest estimation for the velocities, that is to say:

$$u_i^{k+1} = u_i^{m*} + \sum_r^k u^r \; ; \; p^{k+1} = p^{m-1} + \sum_r^k p^r \tag{A.9}$$

By doing so no extra storage is needed and when all the corrections have been performed one will have the final velocities and pressure. The k^{th} estimation for velocities is calculated as:

```
volScalarField rUA = 1.0/UEqn.A();
U = rUA*UEqn.H();
```

For the step zero, this means that we are giving an initial guessing of the velocities without accounting for the pressure:

$$\tilde{u}_{i,P}^{m*} \approx -\frac{\sum_l A_l^u u_{i,l}^{m*}}{A_P^{u_i}} \tag{A.10}$$

For the correction steps this calculate the k^{th} estimation .

$$\tilde{u}_{i,P}^{k} \approx -\frac{\sum_l A_l^u u_{i,l}^{k}}{A_P^{u_i}} \tag{A.11}$$

The symbol   is there to remember that this velocity lacks the pressure gradient.

3. The balance of fluxes is adjusted to globally obey continuity.

```
phi = (fvc::interpolate(U) & mesh.Sf())
```

```
+ fvc::ddtPhiCorr(rUA, U, phi);

adjustPhi(phi, U, p);
```

The flux on the surfaces (ρu) is calculated by interpolating then it is adjusted to be conservative on the domain. Such flux will be used to solve the Poisson equation and find a new correction for the pressure.

4. The Poisson equation for pressure is defined and it is solved once, then it is solved again for the prescribed number of non-orthogonal corrections (that is the step of correction to adapt the method for non orthogonal meshes):

   ```
   fvScalarMatrix pEqn
   (
   fvm::laplacian(rUA, p) == fvc::div(phi)
   );
   ```

   Which is the same as:

   $$\frac{\delta}{\delta x_i}\left[\frac{\rho}{A_P^{u_i}}\left(\frac{\delta p^{k+1}}{\delta x_i}\right)\right]_P = \left[\frac{\delta\left(\rho \tilde{u}_i^k\right)}{\delta x_i}\right]_P \tag{A.12}$$

   We are calculating the updated pressure using the latest estimation for the velocities.

5. Correct the velocities with the new pressure gradient.

   ```
   U -= rUA*fvc::grad(p);

      U.correctBoundaryConditions();
   ```

   This assignment implicitly calculate the new velocity as

   $$u_{i,P}^{k+1} = \tilde{u}_{i,P}^k - \frac{1}{A_P^{u_i}}\left(\frac{\delta p^{k+1}}{\delta x_i}\right)_P \tag{A.13}$$

   so that U in the code contains the velocity updated to the last computed correction. The summation for p is never explicitly computed because the hypothesis of a p which the results of the sum of small corrections it is used every time the Poisson equation it is performed.

6. Loop until the prescribed number of correction-steps is reached.

Appendix B

Wake Visualization Experiments

The author of the present work was responsible for some measurements on the scaled model representative of the DeltaStream device taken in INFREMER, Boulogne Sur Mer. The test rig was designed by the Cranfield Offshore Department and the data acquisition and processing as well.

The author could dispose of an ADCP testing instrument gently provided by “Nortek AS” for the velocity profiles data acquisition.

The aim of the deployment of the instrument was

- understanding velocity profiles in the wake
- providing a validation for the numerical method

At the moment of writing this report wake contour plots for a single turbine in isolation have been produced but no cross-validation with numerical simulations have been performed. This task is postponed to the future.

The instrument has the capability of measuring velocity orthogonal to an acoustic beams that propagate from its the head by means of measuring the correlation of the signal. The velocity is evaluated for different distances in the propagation direction. Combining reading from beams disposed in different directions it is possible to extrapolate a 3D field.

The instrument used had only a single beam available and that was oriented in a way to face the flow with angle of 65 degree on the horizontal plane. From simple trigonometry it was so possible to evaluate the axial velocity in the wake moving the instrument in four different locations in the steam-wise direction as reported in Fig.B.1a.

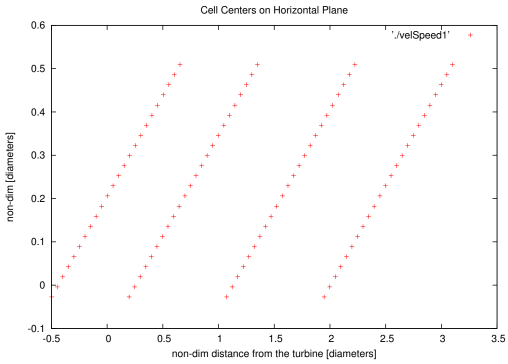

(a) Acquisition cells centers disposition in space

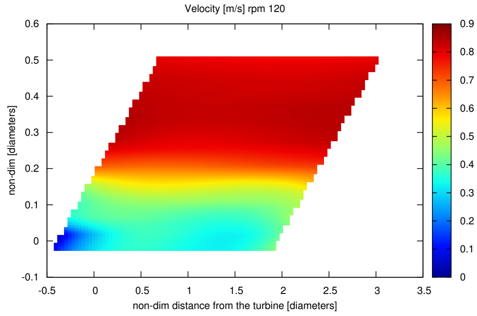

(b) Velocity contour 120 rmp

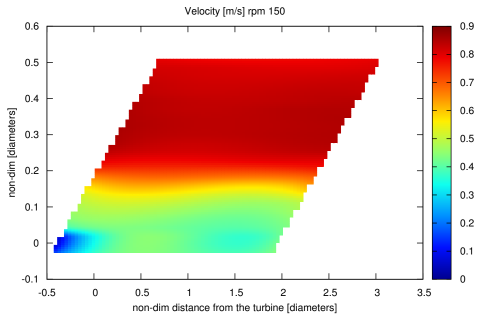

(c) Velocity contour 150 rmp

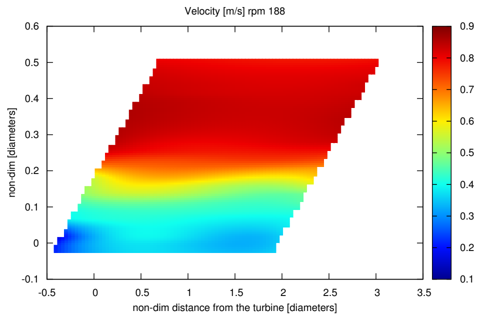

(d) Velocity contour 188 rmp

Fig. B.1 ADCP contours of the wake

In Fig. B.1 contours for different shaft speeds of the model are reported for half of the wake after interpolation. The inflow velocity is kept constant.

The contours show how there is an apparent initial stretching of the wake that then diffuses increasing its axial dimension. The dept of the wake in the range of velocities considered should increase with the rpm.

Appendix C

Channel Flow Resolved Turbulence Simulation

Turbulence in tidal channels is crucial for the unsteady loads assessment. The decision of using an LES model is a direct consequence of that.
Nominally in a tidal channel the order of magnitude of the Reynolds Number can be as high as 10^7. This number indicates the ratio between convective and viscous actions in the field. The first are responsible for the cascade of turbulence from the production scale, the latter for its dissipation at high frequencies. In environmental flows the separation between the largest and the smallest scale is then relevant. The flow is though known to recover homogeneity at the small scales thus LES use is possible for the solution of the only large scales in the domain [53]. It is also true that the grid size for an LES simulation is independent of the separation for Reynolds Numbers that are sufficiently high. In fact only the scales where the non homogeneous effects are relevant need to be modelled. These scales are also the scales relevant for the loads. The structure inertia acts as a filter on the frequencies of the order of some *cm* .
A Reynolds Number around 10^5 is considered sufficient to develop the fluid field numerical model. Also in freely available literature only data for channel simulations up to those values are available. Further validation will come from the scheduled test taking place in INSEAN during the winter. The size and water speed in the flume tank that will be in use are sufficient to go up to $Re \approx 10^6$.
The current experimental data used are available at [Comte-Bellot] for a channel flow. Hence a channel flow simulation is set for validation. The configuration parameters are then used for the boundary layer simulation in the interest of this work.

Table C.1 Flow Field Grids Synthetic Table

Simulation	Channel Flow	Boundary Layer 1	Boundary Layer 2
Computational domain	$2\pi\delta \times 2\delta \times \pi\delta$	$2\pi\delta \times 2\delta \times \pi\delta$	$2\pi\delta \times 2\delta \times \pi\delta$
δ	$1[m]$	$1[m]$	$1[m]$
Δx^+	250	250	250
Δz^+	125	125	125
$y_w^+ lowerblock$	0.5	0.5	0.5
r lower block	1.1	1.1	1.1
r upper block	0.91	1	1
N_x	206	206	206
N_z	206	206	206
N_y	140	81	177
N_tot	$5.9 \cdot 10^3$	$3.4 \cdot 10^3$	$7.5 \cdot 10^3$

A grid and turbulent model dependency study was carried out by a visiting student Thilo Engelking who worked under the direction of the author.

C.0.1 Channel Simulations

The turbulence model considered the most suitable for the present study is the DDES for its computational reduced cost and capability in coping with complex boundary layer flows. This feature is not taken advantage of at this stage of the work but it will be when considering the local bathymetry in place of the flat wall.

Grid Size The grid size chosen is $2\pi\delta \times 2\delta \times \pi\delta$ respectively in the x stream-wise, y wall normal and z cross-wise directions. The spacing is uniform in the two homogeneity directions x and z. In y a constant expansion ratio $r = 1.0585$ (figure C.1) is selected in a way to meet the condition for the first cell centre to be at $y_w^+ \leq 1$. One can find information about the

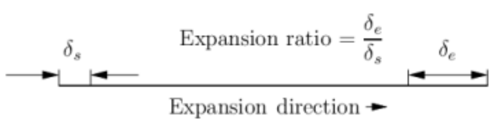

Fig. C.1 Graded grid spacing along an edge of a block in OpenFoam

grid spacing alongside the other grids considered in table C.1.

The $^+$ variables are non-dimensional in “wall” length units, [53].

Table C.2 Boundary Conditions for Flow Field Simulations

Simulation	Channel Flow	Boundary Layer 1
min X	coupled with max X	coupled with max X
min X	coupled with min X	coupled with min X
min Y	zero value zero gradient for pressure	zero value zero gradient for pressure
max Y	zero value zero gradient for pressure	zero normal value and tangent gradient zero normal value and tangent gradient
min Z	coupled with max Z	coupled with max Z
min Z	coupled with min Z	coupled with min Z

Boundary Conditions The boundary conditions applied are reported in table C.2.

Cyclic conditions are applied both on the X and Z faces. The Y faces are considered non slip walls where all the variables go to zero but the pressure that is considered constant across the closest to the wall cell.

Bulk Condition Under these conditions the system will remain invariant if initialized to zero fields. The flow field is driven by an average pressure gradient that keeps the mass averaged velocity equal to 1. Also at the initial time step, velocity and pressure are set to be random variables in the domain. This is done to help the evolution of a turbulent field.

Velocity Correlation The chosen domain size assures that for an average unitary velocity, turbulence statistics of velocity fluctuations are uncorrelated in stream and cross wise directions [35]. This is confirmed by the plot of B_{11} and B_{33} in figure C.3b. These plots are obtained from the use of "spectrumFoam". One can observe how the correlation value drops from one at zero distance to less than 10% in the centre of the channel showing the size is sufficient to assure independence of the turbulent structures generated. The normal to the wall direction shows a week dependency in both x and y, the other two show a higher autocorrelation in their direction. This is due to the fact that x direction velocity structure tend to propagate in x and the same is true for y.

Experimental Validation The channel flow for a Reynolds Number of 230000 has been compared to the experimental values in [Comte-Bellot]. Synthetic results for the average

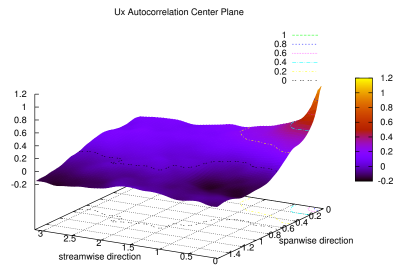

(a) Stream-wise velocity correlation on a plane $y = \delta$

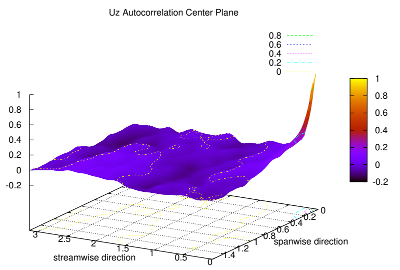

(b) Cross-wise velocity correlation on a plane $y = \delta$

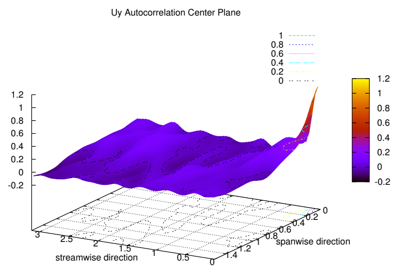

(c) Normal-to-the-wall velocity correlation on a plane $y = \delta$

velocity and the Reynolds Stresses i.e. turbulence statistics at zero separation are reported respectively in figure C.3a and C.3b. These have been computed with the use of the standard OpenFoam "postChannel" utility. One can notice how the both the cross-wise and normal-to-the-wall statistics match very closely the experimental values. On the average velocity and stresses in the stream-wise direction there are relative errors locally always smaller that 10%. The max error is anyway reached in the areas closest to the wall that have the smallest velocity hence contribution to the power production of the turbines.

C.0.2 Boundary Layer Simulations

Once the methodology has been validated it is possible to extend the results to a similar case. The boundary layer case differs from the channel for the removal of the non slip condition applied to the top wall. Instead a free slip wall is used. From the numerical aspect the only condition changing is that the tangent to the boundary velocity is not fixed to zero but free to variate (table C.2). There is no longer need for the resolution of a boundary layer turbulence in proximity of the upper wall. It is then reasonable to extend the mesh keeping constant the

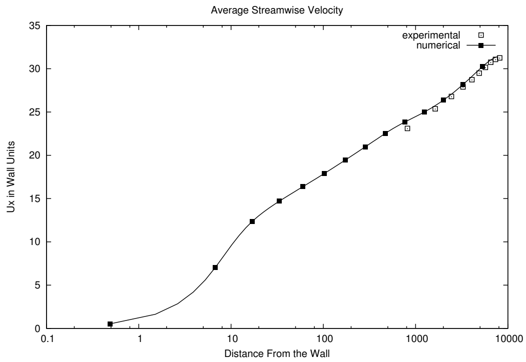

(a) Stream-wise average velocity (Distance from the wall in wall units)

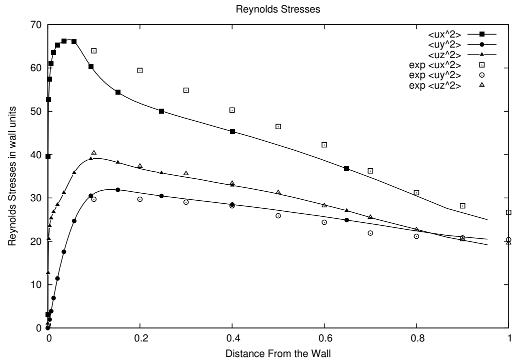

(b) Channel Flow Statistics at zero separation

mesh size at the center of the channel (table C.1 Boundary Layer 1).

On this mesh a more refined statistical analysis is carried on. The study of the power spectrum is useful in order to correlate turbulence with thrust and torque frequency signature for the turbine and discern the various causes of the unsteadiness [22]. In the future work the calculated spectral densities will then be correlated with water tank experiments.
In figure C.4 the PSD for three different vertical locations is shown. The spacial results is obtained using the "spectrumFoam" own developed code. The time spectrum is obtained by collection of velocity data in determined locations in the numerical domain over the time of the simulation. The MATLAB function "periodgram" provides the PSD algorithm. Time and space can be plotted on the same axis according to the mentioned *Taylor Hypotesis*.
The reference spectrum plotted in continuous line is the "Von Karman" spectrum for the stream-wise velocity

$$hi_{u_g}(\omega) = \sigma_u^2 \frac{2L_u}{\pi} \frac{1}{(1+(1.339L_u\omega)^2)^{\frac{5}{6}}} \tag{C.1}$$

where the integral length scale L_u and the variance σ_u^2 are computed in MATLAB too from the time signal. ω is the frequency. The "Von Karman" spectrum differs form the calculated ones for the nature of a DDES simulation. In fact the LES filter cuts off the high frequencies for the time spectrum. The space trace ends in the nearby of this condition being the filter size tailored on the mesh. Also the energy level roughly matches only for the centre plane case. Water tank experiments are expected to clarify all the aspects in order to extrapolate a realistic spectrum model for the cases considered in this work.
For the levels and typology of turbulence generated by a flat wall at $Re = 230000$ the time

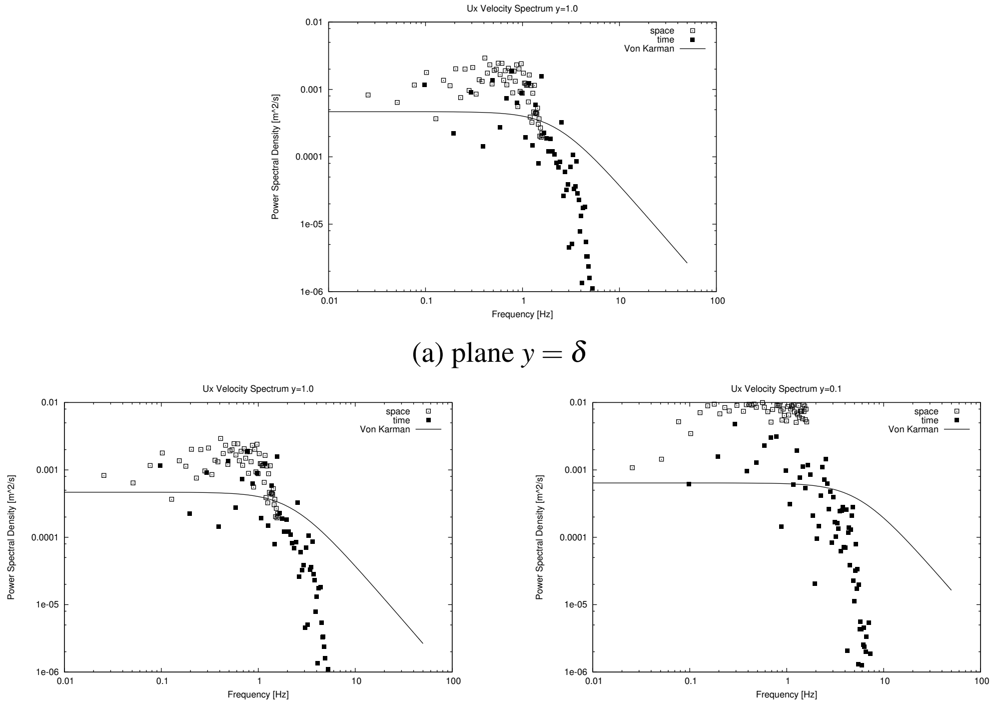

(a) plane $y = \delta$

(b) plane $y = 0.5\delta$ (c) plane $y = 0.1\delta$

Fig. C.4 Stream-wise velocity PSD at parallel-to-the-wall planes in Channel Flow

and space formulations coincide as from the calculated spectra. This is not known to be true in general in environmental flow being the largest structures in the field being convected at higher speeds [19] than the smaller when compared to artificial turbulence. This could mislead in the loads assessment hence further research is necessary.